

Rapport Final de Travail de Fin d'études

Particles Deposition on an Array of Spheres using a Hybrid Euler/Lagrange CFD Method

Simon MARTIN

Tuteurs :

Option : Aéronautique

ECL :

Dr. Francis Leboeuf

Filière : Propulsion

Entreprise :

Dr. Abdel Dehbi

Métier : Recherche et Développement



Abstract

English:

A numerical method designed for calculation of particles deposition on spheres has been benchmarked. Air flows past single spheres and linear arrays of eight spheres with various spacing have been solved using an Eulerian CFD-RANS method with RSM turbulence model. Simulations have been performed at Reynolds numbers between 6×10^3 and 1.2×10^4 . Then particles tracking computations have been conducted using a Lagrangian method. Interactions between particles and turbulent velocity fluctuations have been computed using a stochastic model based on the Langevin equation. The particles Stokes number ranges from 0.03 to 4.5. Numerical results are compared to experimental data. For particles with very low inertia (Stk around 0.03) coherence between the two is not good. However because of the scattering of the data for this range of Stk values the computational method performance can hardly be judged by this comparison. For particles with higher inertia (Stk above 0.3) the coherence between results and data is quite good for close sphere: errors around 10 % only for a spacing of 1.5 diameters between two successive centers. Then the coherence deteriorates when the spacing increases: errors above 30 % for spacing above 2 diameters. This limitation of the numerical approach is probably due to the RANS resolution of the flow and then the lack of accuracy on turbulence intensity resolution. That is why applying the method with DES solved flows is proposed for future research but not tried because of time constraints.

Keywords: CFD, model benchmarking, RANS, Lagrangian particles tracking, stochastic model, particles deposition on spheres

Français:

L'évaluation des performances d'une méthode numérique conçue pour calculer le taux de déposition de particules sur des sphères a été réalisée. Dans un premier temps un flow d'air autour de sphères isolées ou de rangées de huit sphères calculé numériquement à l'aide d'une méthode Eulérienne basée sur des équations RANS-RSM. Le calcul a été réalisé pour plusieurs régimes et le nombre de Reynolds associé aux sphères varie entre 6×10^3 and $1,2 \times 10^4$. Ensuite des calculs de suivi Lagrangien de particules ont été conduits. Lors de ces calculs l'effet des fluctuations turbulentes de vitesse sur les particules a été modélisé à l'aide d'un model stochastique basée sur l'équation de Langevin. Le nombre de Stokes associé aux particules injectées varie entre 0.03 et 4.5. Enfin les résultats numériques ont été confrontés à des résultats d'expériences réalisées dans les mêmes conditions. Pour les particules à faible inertie (Stk autour de 0.03) la cohérence entre résultats de simulation et données d'expériences n'est pas bonne ; cependant pour d'aussi petites particules la dispersion des données expérimentale semble être très importante, l'efficacité du model peut donc difficilement être jugée sur ces résultats-ci. Pour les particules d'inertie supérieures (Stk entre 0.3 et 2.3) les résultats semblent plus prometteurs. Quand les sphères sont proches les unes des autres la cohérence entre résultats de simulation et données d'expériences est plutôt bonne : à peu près 10 % d'erreur seulement pour un espacement de 1.5 diamètre entre deux centres successifs. Cette cohérence se dégrade avec l'augmentation de l'espacement : l'erreur dépasse les 30 % pour un espacement au delà de 2 diamètres. Cette limitation du model numérique est probablement causée par le calcul RANS qui tend à sous estimer l'intensité de la turbulence. C'est pourquoi appliquer la même méthode mais avec un calcul DES a été envisagé mais non mis en œuvre par manque de temps.

Acknowledgements

Many thanks to my supervisor, Dr Abdel Dehbi, for guiding me throughout my internship.

Thanks to Dr Detlef Sockow and Hauke Schuett, for helping me with my computer.

Thanks to Beatrice Gschwend for helping me with papers.

Thanks to everyone in the Sacree group.

Table of Content

ABSTRACT	3
ACKNOWLEDGEMENTS	4
TABLE OF CONTENT	5
LIST OF FIGURES & TABLES	7
NOMENCLATURE	9
INTRODUCTION	11
1 THEORY AND BACKGROUND	13
1.1 PARTICLES TRACKING	13
1.2 PREVIOUS INVESTIGATIONS	20
1.3 OBJECTIVE AND RESOURCES	24
2 FLOW SIMULATION	25
2.1 GEOMETRY AND MESH	25
2.2 SIMULATION OVERVIEW	32
2.3 RESULTS AND DISCUSSIONS	46
3 PARTICLES TRACKING	51
3.1 PARTICLE INJECTION AND DEPOSITION CALCULATION METHODS	51
3.2 PARTICLES DEPOSITION ON SINGLE SPHERES	57
3.3 PARTICLES DEPOSITION ON ARRAYS OF SPHERES	60
CONCLUSION	77
REFERENCES	78
ANNEXES	79
ANNEX 1: GAMBIT JOURNAL FILE	79
ANNEX 2: MESH PARAMETERS	87
ANNEX 3: FLOW FIELDS RESULTS FOR 8 SPHERES	89
ANNEX 4: FORTRAN PROGRAMS FOR INJECTORS	94
ANNEX 5: PARTICLES DEPOSITION RESULTS	95



List of Figures & Tables

Figures

Figure 1 : Interaction particles/turbulent velocity fluctuation	15
Figure 2 : Drag coefficient for uniform flow past a sphere	21
Figure 3: Sphere wall's coefficients at $Re = 165,000$	22
Figure 4 : Flow past a sphere at $Re = 11,000$; mean flow field velocity and stream lines	22
Figure 5 : Experimental set ups for particles deposition measurement on spheres	23
Figure 6 : Examples of global geometries	26
Figure 7 : Base geometry	26
Figure 8 : Reduced base geometry	27
Figure 9: Base geometry subdivision	27
Figure 10 : Core volume	28
Figure 11 : Core volume subdivision	28
Figure 12 : Sphere boundary layer definition	28
Figure 13 : Core meshing	29
Figure 14 : Tube and inlet meshing	30
Figure 15 : Middle front of the sphere's mesh	30
Figure 16 : Global geometry construction method	31
Figure 17 : Sphere spacing determination technique	31
Figure 18 : Boundary condition calculation method	33
Figure 19 : Single Sphere & $Re = 5,000$; wall coefficients for grid independence	35
Figure 20 : Single sphere & $Re = 5,000$; wake values for grid independence	35
Figure 21 : Single sphere & $Re = 5,000$; boundary layer	36
Figure 22 : Single sphere & $Re = 5,000$; wall coefficients for spatial discretization influence	37
Figure 23 : Single sphere & $Re = 5,000$; wakes values for spatial discretization influence	37
Figure 24 : Single sphere & $Re = 12,000$; boundary layer	38
Figure 25: Normal velocity in the XY plane in percent of the inlet velocity magnitude	38
Figure 26 : Single sphere & $Re = 12,000$; results with finest grid	39
Figure 27 : Single sphere & $Re = 12,000$; normal velocity in the wake	40
Figure 28 : Whole geometry to reduced geometry	40
Figure 29 : Single sphere & $Re = 5,000$; results values with quarter mesh	41
Figure 30 : $Re = 12,000$; Normal velocity in percent of the inlet velocity magnitude	42
Figure 31 : 8 spheres & $L/D = 2$ & $Re = 12,000$; results values for grid independence	44
Figure 32 : 8 spheres & $L/D = 6$ & $Re = 12,000$; results values for grid independence	45
Figure 33 : Single sphere & $Re = 12,000$; comparison simulation/data	47
Figure 34 : Single sphere & $Re = 12,000$; boundary layer detachment point	47
Figure 35 : Single sphere; recirculation area, comparison simulation/data	47
Figure 36 : Single sphere; wall friction coefficient, Re influence	48
Figure 37 : Single sphere; recirculation area, Re influence	48
Figure 38 : Single sphere; turbulent intensity, Re influence	49
Figure 39 : Inlet area subdivision	53
Figure 40 : Particle density repartition for various numbers of particles	55
Figure 41 : Collection efficiency of single sphere; comparison whole vs. reduced geometry	56
Figure 42 : Collection efficiency of single sphere; experimental data	57
Figure 43 : Collection efficiency of single sphere; particles tracking results	58
Figure 44 : Collection efficiency of single sphere; comparison data vs. simulation results	59
Figure 45 : Collection efficiency on linear arrays; data from Hähner	61
Figure 46 : collection efficiency on linear arrays; data from Waldenmair 1	61
Figure 47 : collection efficiency on linear arrays; data from Waldenmair 2	62
Figure 48 : Comparison collection efficiency leading spheres vs. single spheres	62
Figure 49 : Comparison collection efficiency leading spheres vs. single spheres	64
Figure 50 : Collection efficiency of arrays; simulation results, spacing influence	64

Figure 51: Collection efficiency of arrays; simulation results, Re influence	66
Figure 52: Collection efficiency of arrays; simulation results, tracking model influence	67
Figure 53 : Particles deposition repartition; simulation results.....	68
Figure 54 : Collection efficiency of leading spheres, comparison simulation results vs. data	69
Figure 55 : Collection efficiencies with $L/D = 1.5$, comparison simulation results vs. data.....	70
Figure 56 : Results with $L/D = 1.5$, model benchmarking	71
Figure 57: Collection efficiencies with $L/D = 2$, comparison simulation results vs. data.....	72
Figure 58 : Results with $L/D = 2$, model benchmarking	73
Figure 59: Collection efficiencies with $L/D = 6$, comparison simulation results vs. data.....	74
Figure 60 : Results with $L/D = 6$, model benchmarking	74
Figure 61: Relative collection efficiencies ($L/D = 6$), comparison simulation results vs. data.	75
Figure 62 : Results extraction line	89
Figure 63 : 8 spheres & $L/D = 6$ & $Re = 12,000$; global wall results	90
Figure 64 : 8 spheres & $L/D = 2$ & $Re = 12,000$; global wake results	91
Figure 65 : 8 spheres & $L/D = 6$ & $Re = 12,000$; global wall results	92
Figure 66 : 8 spheres & $L/D = 6$ & $Re = 12,000$; global wake results	93

Tables

Table 1: Boundary conditions values	33
Table 2 : Meshes for single sphere.....	34
Table 3 : Single sphere & $Re = 5,000$; simulations' main results.....	34
Table 4 : Single sphere & $Re = 5,000$; spatial discretization influence	36
Table 5 : Single sphere & $Re = 12,000$; simulation's main results.....	37
Table 6 : Finest mesh parameters for single sphere	39
Table 7: Single sphere & $Re = 12,000$; simulation results for finest grid	39
Table 8 : Quarter mesh parameters	41
Table 9 : Single sphere & $Re = 5,000$; simulation's main results with quarter mesh.....	41
Table 10 : Single sphere & $Re = 12,000$; simulation's main results with quarter mesh.....	42
Table 11 : Single sphere main results summary	42
Table 12 : Meshes for 8 spheres & $L/D = 2$	43
Table 13 : 8 spheres & $L/D = 2$ & $Re = 12,000$; simulations' main results	43
Table 14 : Meshes for 8 spheres & $L/D = 6$	44
Table 15 : 8 spheres & $L/D = 6$ & $Re = 12,000$; simulations' main results	45
Table 16 : Mesh for 8 spheres & $L/D = 1.5$	46
Table 17 : 8 spheres; simulations' main results summary	46
Table 18 : Injector size determination for single sphere cases	54
Table 19: Injector size determination for 8 spheres cases	54
Table 20 : Relative error in particles distribution for various injectors.....	55
Table 21 : Experimental data available	60
Table 22 : Particles tracking computations summary ($X =$ data available)	63
Table 23 : Collection efficiency of leading spheres, gaps and errors.....	69
Table 24 : Particles deposition on arrays, Gaps and Errors summary.....	75
Table 25 : Mesh parameters detail	87
Table 26 : Collection efficiency results for singles spheres	95
Table 27 : Particles tracking results for linear arrays of 8 spheres	100

Nomenclature

Latin symbols

C_d	: Sphere drag coefficient (-)
C_p	: Sphere pressure coefficient (-)
C_f	: Sphere friction coefficient (-)
D	: Sphere diameter (m)
D_t	: Pipe diameter (m)
D_i	: Injector diameter (m)
d_p	: Particle diameter (m)
δ	: Boundary layer first row thickness (m)
g	: Earth gravitational acceleration (m.s^{-2})
I	: Turbulence intensity (-)
k	: Turbulent kinetic energy ($\text{m}^2.\text{s}^{-2}$)
l	: Turbulence length scale (m)
L	: Distance between two successive sphere centers in an array (m)
L/D	: Sphere spacing (-)
N_0	: Number of particles carried into the projected area of a collector (-)
N_d	: Number of particles deposit on a collector (-)
N_p	: Number of particles injected into the projected area of the first sphere (-)
N_i	: Number of particles deposited on the sphere i (-)
m_p	: Particle masse (kg)
p_i	: Particles deposition repartition on sphere i (-)
r	: Injector ratio (-)
R	: Boundary layer growth factor (-)
Re	: Sphere Reynolds Number (-)
Re_t	: Pipe Reynolds Number (-)
Stk	: Particle Stokes number (-)
u	: Fluid velocity (m.s^{-1})
u_∞	: Fluid main stream velocity (m.s^{-1})
u_0	: Inlet fluid velocity (m.s^{-1})
u'	: Fluctuating velocity (m.s^{-1})
u^*	: Wall shear velocity (m.s^{-1})
u_p	: Particle velocity (m.s^{-1})
y^+	: dimensionless wall distance (-)

Greek symbols

ϵ	: Dissipation rate of kinetic energy ($\text{m}^2.\text{s}^{-3}$)
η	: Sphere collection efficiency (-)
η_r	: Sphere relative collection efficiency (-)
μ	: Fluid dynamic viscosity (Air = $1.79 \cdot 10^{-5} \text{ kg.m}^{-1}.\text{s}^{-1}$)
ν	: Fluid kinematic viscosity (Air = $1.46 \cdot 10^{-5} \text{ m}^2.\text{s}^{-1}$)
ρ_p	: Particle density (DES = 913 kg.m^{-3})
ρ_f	: Fluid density (Air = 1.22 kg.m^{-3})
τ_p	: Particle relaxation time (s)

Mesh parameters:

Fr : Boundary layer first row size (mm)
R : Boundary layer growth factor
Nr : Boundary layer number of rows
Nn : Circular resolution
Nns : Core radial resolution in front of the sphere
GF : Core radial growth factor in front of the sphere
Ndc : Core axial resolution in front of the sphere
GD : Core axial growth factor in front of the sphere
Nps : Axial resolution above the sphere
Ndp : Tube radial resolution
FI : Tube radial inner first row size (mm)
Fn : Tube radial outer first row size (mm)
Npi : Inlet axial resolution
LI : Inlet axial last row size in mm

Introduction

Developed by a team led by South Africa, a new concept of nuclear reactor named Pebble Bed Modular Reactor should be able to offer high efficiency production of electricity and better safety performances than the actual fusion reactors. As part of this project, the department of Nuclear Energy and Safety (NES) of the Paul Scherrer Institut contributes to the development of computational methods to predict the progression of severe accidents and the release of radioactive materials into the atmosphere.

The Pebble Bed Modular Reactor (PBMR) is an advanced high-temperature gas-cooled, and graphite moderated reactor. The fuel elements are spherical graphite “pebbles” about 6 cm in diameter. These spheres contain microsphere of uranium dioxide. Helium gas flows over and through the gaps between the pebbles and act as a coolant. The graphite fuel has high thermal conductivity and high heat capacity. Because of that, the plan can withstand a broad spectrum without the need for operation of active safety systems and with very limited release of radionuclides to the environment. Nevertheless, in the PBMR design, the graphite pebbles are continually rubbing against each other. Because of that a very large quantity of graphite dust is released in the reactor coolant system. Then dust particles are transported and deposited on surfaces by aerosol processes. Thus, in the event of a pipe leak, rapid depressurization of the system may cause the release of radioactive material airborne into the surrounding atmosphere. That's why it is very important to develop computational models which quantify accurately the potential threat of these radioactive aerosols, and the Laboratory of Thermal-Hydraulic (LTH) of the NES contributes to such project. A part of the development of such models consists on modeling the aerosol deposition rate on pebble bed during normal and critical operating conditions. However, the numerical method used to calculate the particle deposition has to be benchmarked before.

On the one hand Dr A. Dehbi, member of the LTH, has already carried out several benchmarking of turbulent particles dispersion models on wall-bounded geometries. The method then used is based on a CFD-Langevin-equation approach and it was applied for simple wall bounded geometries like straight pipe and 90° bend pipe. The results then obtained show good coherence with experimental data. However the geometry used is quite different from those of pebble beds. Therefore the method has to be benchmarked using geometries closer to a pebble bed.

On the other hand experiment of particles deposition on single and linear arrays of spheres experiments have been conducted. A pebble bed being a pile of spheres, benchmarking the model using these results will be a step further to obtain a numerical method that can be used on actual pebble bed geometry.

The investigation presented here consists on benchmarking this numerical method using particles deposition measurements on spheres. In a first part the theoretical aspects of the numerical method along with the experimental investigations are summarized. Then the two following parts present the application of the method; the second part presenting its CFD side and the third part presenting its particles tracking side. The benchmarking of the method is carried out in the third part.



1 Theory and background

This first part of the report gives some theoretical basis on particles diffusion modeling. It also concisely presents several other investigations linked to the study of particles deposition on spheres.

1.1 Particles tracking

In order to carry out numerical computations of particles deposition on collectors particles diffusion on a fluid has to be modeled. To do this it exist many different methods and models. This chapter gives basic information about those used for our study.

1.1.1 Particles Transport and Deposition mechanisms

Depending on the size of a particle and the nature of the flow, different mechanisms can be responsible for its transport and deposition.

Continuous phase influences motion of discrete particles through fluid forces such as:

- Drag: due to viscous and inertial effects of the fluid on particles, this force is always along direction of particle relative velocity and tends to make equal the particle velocity and the flow velocity. The drag force per unit mass may be expressed as :

$$F_D = K_D(u - u_p) = C_D \cdot \frac{Re_p}{24} \cdot \frac{18\mu}{\rho_p d_p^2} \cdot (u - u_p)$$

with:

$$Re_p \equiv \frac{\rho_f d_p |u - u_p|}{\mu} = \text{particles relative Reynolds number}$$

C_D : Drag coefficient (its expression depends on the value of Re_p)

μ, ρ_f et u : fluid viscosity, density and velocity

ρ_p, d_p et u_p : particle density, characteristic length and velocity

This force is always important.

- Gravity and Buoyancy: these two forces are along the gravitational acceleration and are in competition. The sum of the two can be expressed as (per unit mass):

$$F_G = g \left(1 - \frac{\rho_f}{\rho_p} \right)$$

Depend on the value of $\frac{\rho_f}{\rho_p}$ Gravity or Buoyancy will prevail.

- Lift: due to local velocity gradient or particle rotation, this force is always normal to particle relative velocity. This force is important for light particles ($\rho_p < \rho_f$) and secondary for heavy particles ($\rho_p > \rho_f$).
- Brownian diffusion: due to the Brownian motion of particles in a fluid. Important only for small particles ($d_p < 0.1 \mu\text{m}$).
- Thermophoresis: due to temperature gradient in the fluid, this force tends to move aerosols toward the decreasing temperature. The thermophoresis force per unit mass may be expressed as :

$$F_{th} = -D_{T,p} \cdot \frac{1}{m_p T} \nabla T$$

with:

$D_{T,p}$: thermophoresis coefficient (depends on both fluid and particle)

m_p : particle masse

When an important temperature gradient exists between the inlet air flow and the wall this mechanism can have a important influence on particle deposition rate.

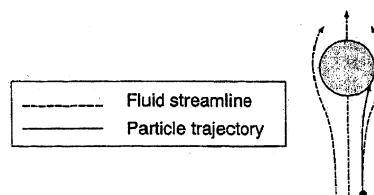
- Electrophoresis: due to presence of an electric field
- Photophoresis: due to intense light radiation
- Etc ...

All transport mechanisms except for the drag force can bring a particle to contact a boundary of the fluid domain. Then, adhesives forces (e.g. Van der Waals force) tend to cause particles to adhere to the surface.

However, because of particle's inertia, it takes a certain amount of time for a particle to react to an acceleration of the fluid. In order to quantify this "reaction time", a temporal parameter depending on both particle and fluid has been defined. It is called the relaxation time and is defined as such:

$$\tau_p \equiv \frac{\rho_p d_p^2}{18\mu}$$

Thus, due to particle's inertia, an aerosol's trajectory may deviate from the fluid main streamline since it can be unable to follow the motion of an accelerating gaz. By following its own trajectory rather than the trajectory of a fluid passing around a solid object the aerosol can impact on the solid surface. This deposition mechanism is called **Inertial Impaction**.



In order to quantify this mechanism one uses the Stokes Number:

$$Stk \equiv \frac{\tau_p \cdot u_\infty}{D_o} = \frac{\text{Particle response distance}}{\text{characteristique length}}$$

with:

D_o : *characteristique dimension of the obstacle*
 u_∞ : *fluid main stream velocity*

Depending on the value of the Stokes Number, particle adjusts to flow and not impact on wall ($Stk \ll 1$), or mainly follows its own trajectory and impacts on wall ($Stk \gg 1$).

There exists another mechanism also due to particle inertia that can lead particle to deviate from a fluid main streamline. Turbulent eddies create fluctuating velocity component which are sometime normal to the main streamline. Depending on turbulence intensity and particles inertia, particles that only partially follow eddies motion are carried away from the main streamline. This phenomenon then affects particles concentration and doing so particles deposition. Moreover if a particle pass near a wall it can also be projected on it by turbulent fluctuations (see Figure 1).

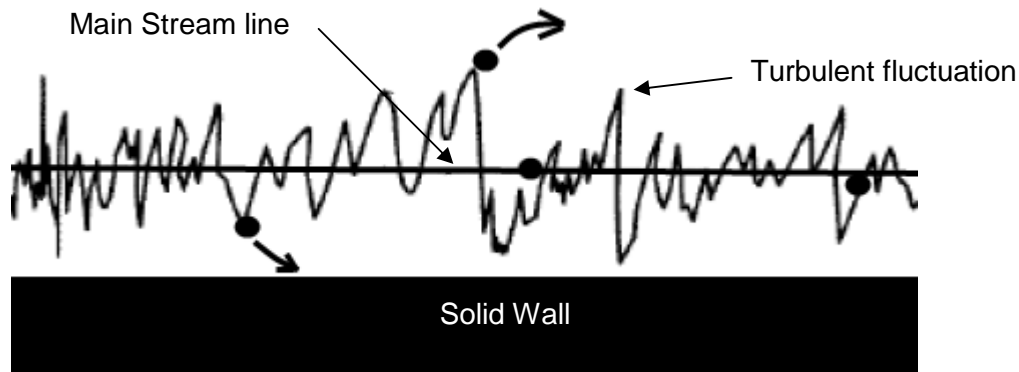


Figure 1 : Interaction particles/turbulent velocity fluctuation

Then two kind of inertial deposition mechanisms can be differentiated:

- Inertial Impaction due to main velocity field and characterized by the Stokes number.
- Turbulent-enhanced deposition due to fluctuating velocity.

That is why it is very important to accurately model turbulence and velocity fluctuations or particles deposition will sometime be highly underestimated.

Finally because of Particle Bounce or Re-entrainment particles impacting a wall have only a probability h to deposit. For solid collector and solid particles h can fall to only a few percent.

1.1.2 Particles tracking methods and equations

There are two main families of methods to treat particle transport in fluid flows: Eulerian and Lagrangian.

— In the Eulerian or “two-fluid” approach, the particles are regarded as a continuous phase for which the averaged conservation equations (continuity, momentum and energy) are solved in similar fashion to the carrier gas flow. The Eulerian approach is particularly suitable for denser suspensions when particle–particle interactions are important and the particle feedback on the flow is too large to ignore.

— In the second approach, called Lagrangian, the particles are treated as a discrete phase made of particles which are dispersed in the continuous phase. The particle volume loading is usually assumed negligible, so that particles have no feedback effect on the carrier gas and particle–particle interactions are neglected. In the Lagrangian framework, the controlling phenomena for particle dispersion in the field are assessed using a rigorous treatment of the forces acting on the particle. In general, the detailed flow field is computed first, then a representatively large number of particles are injected in the field, and their trajectories determined by following individual particles until they are removed from the gas stream or leave the computational domain. Particle motion is extracted from the time integration of Newton’s second law, in which all the relevant forces can be incorporated (drag, gravity, lift, thermophoretic force, etc.). The Lagrangian approach is computationally intensive, because it entails tracking a large number of particles until stationary statistics are achieved. On the other hand, the results of Lagrangian particle tracking are physically easier to interpret. Therefore, in the following investigation, the Lagrangian methodology is used, along with the assumption that the dispersed phase is dilute enough not to affect the continuous flow field.

The methods used here are Lagrangian ones. Then the equations used for these methods are detailed below.

When applying the Newtown's second law to a particle we obtain the following equation (the fluid velocity u has been solved previously independently of any particles tracking):

$$\frac{du_p}{dt} = K_D \cdot (u - u_p) + F_G + F_{th} + \text{Lift} + \dots$$

The trajectory $x(x_1, x_2, x_3, t)$ of the particle is obtained by integration of the following velocity vector equation with respect to time:

$$\frac{dx}{dt} = u_p$$

In laminar flows only the averaged velocity field is influencing particles motion and the previous expressions are sufficient to compute the trajectory of individual particles whatever the method used to solve the flow (RANS, LES or DNS). As particles trajectory is deterministic few trajectory computation are needed to obtain the mean dispersion statistics.

In turbulent flows, random velocity fluctuations are also influencing particles motion. And when turbulent fluctuations exist in the fluid flow, the computation of particle trajectory is no longer deterministic and the particle tracking problem becomes more complicated to handle. To determine the mean dispersion statistics of particles it is necessary to perform many trajectory computations to obtain correct averaged results.

If the flow has been solved with DNS or LES velocity fluctuations are already included into the velocity field. So particles trajectory can be directly computed with no need of further modeling. However, DNS and LES are still very time-consuming process and not fitted for complex 3D geometry.

While using RANS method only the time averaged velocity field is available and turbulence is represented through variables like turbulent kinetic energy, turbulence dissipation rate or Reynolds Stresses components. Then one needs to model the effects of velocity fluctuations on particles.

That is why stochastic models of the fluid velocity fluctuations have been created in order to model the effect of turbulence on Lagrangian particles. For that one uses a Random Walk model consisting of a large number of independent steps with statistic components in each step. Random Walk models are treatments in which particles are made to interact with the instantaneous velocity field u such as:

$$u(t) = \bar{u} + u'(t)$$

with:

\bar{u} : mean velocity

$u'(t)$: fluctuating velocity

Two different kind of Random Walk model are presented here: the Discrete Random Walk Model (CRW) which is implemented in Fluent, and the Continuous Random Walk Model (CRW). These two models have been benchmarked many times by several people and they are described here as in [2] & [3] (A. Dehbi).

In these two models the mean flow is previously solved either by using a steady CFD-RANS method or by averaging an unsteady solution obtain by URANS, DES or LES. Then the Random Walk model is applied in order to model the action of the velocity field on particles.

- DRW model

Here the turbulent dispersion of particles is modeled as a succession of interactions between a particle and eddies which have finite lengths and lifetimes. It is assumed that at time t_0 , a particle with velocity u_p is captured by an eddy which moves with a velocity composed of the mean fluid velocity, augmented by a random “instantaneous” component which is piecewise constant in time. When the lifetime of the eddy is over or the particle crosses the eddy, another interaction is generated with a different eddy, and so forth. The eddy has the following length and lifetime:

$$L_e = C_\mu^{\frac{3}{4}} \frac{k^{\frac{3}{2}}}{\varepsilon}$$

$$\tau_e = C_L \frac{k}{\varepsilon}$$

with:

C_μ and C_L : constants dependent on the model of turbulence used

k : turbulent kinetic energy (obtained in the RANS modeling)

ε : dissipation rate of kinetic energy (obtained in the RANS modeling)

Then the value of the turbulent gas velocity which prevails during the eddy lifetime is randomly drawn from a Gaussian distribution. Hence, in component notation, one has:

$$u_i' = \lambda_i \cdot \sqrt{u_i'^2} \quad \text{avec } i = 1, 2 \text{ ou } 3$$

with:

λ_i : random numbers with zero mean and unit standard deviation.

In the bulk of the flow, where the turbulence is assumed isotropic, the rms values of the three components of instantaneous velocity are obtain from the relationship:

$$\sqrt{u_1'^2} = \sqrt{u_2'^2} = \sqrt{u_3'^2} = \sqrt{\frac{2k}{3}}$$

However, when used in the boundary layer the previous expression introduce a large over-prediction for the wall normal component u_2' . That is why when the particle is inside the boundary layer ($y^+ < 100$) the rms values of instantaneous velocity and turbulence dissipation rate are modified to account for the strong anisotropic nature of turbulence. For that one uses correlations extracted from DNS results:

$$u_1'^+ = \frac{\sqrt{u_1'^2}}{u^*} = \frac{0.40y^+}{1 + 0.0239(y^+)^{1.496}}$$

$$u_2'^+ = \frac{\sqrt{u_2'^2}}{u^*} = \frac{0.0116(y^+)^2}{1 + 0.203y^+ + 0.00140(y^+)^{2.421}}$$

$$u_3'^+ = \frac{\sqrt{u_3'^2}}{u^*} = \frac{0.19y^+}{1 + 0.0361(y^+)^{1.322}}$$

$$\varepsilon^+ = \frac{\varepsilon}{u^{*4}/\nu} = \frac{1}{4.529 + 0.0116(y^+)^{1.75} + 0.768(y^+)^{0.5}}$$

with:

$$u^* = \sqrt{\frac{\tau_w}{\rho_f}} : \text{friction velocity}$$

$$\nu : \text{fluid kinematic viscosity}$$

Despite being quite cheap in CPU time and giving some good results the DRW method suffer from fundamental shortcoming:

- Particle velocity jumps at end of eddy lifetime (infinite acceleration)
- Non-physical accumulation of small particles close to walls, so called "spurious drift", which leads to non-physical deposition of small inertia particles on walls.

- CRW model:

The CRW model have been created to offer a more physical way of modeling the fluctuating velocity, and thus go past the shortcoming of the DRW model.

One of the most common ways to describe fluid velocity fluctuations in a continuous way is through the Langevin equation. In this equation the change in the fluid velocity field with time is assumed to be comprised of a damping term which is proportional to velocity, and a random forcing term that has zero mean. Thus the Langevin equation is a stochastic differential equation which uses Markov chains to specify a possible increment du_i in the fluid velocity fluctuation during a time dt :

$$du_i' = -u_i'(t) \frac{dt}{\tau_i} + \sigma_i \sqrt{\frac{2}{\tau_i}} \cdot d\xi_i$$

with:

τ_i : timescale characteristic of the turbulence

$\sigma_i = \sqrt{u_i'^2}$: rms of fluctuating velocity

$d\xi_i$: random numbers with zero mean and variance dt

The Langevin equation was extensively used to model homogeneous turbulence where the rms values and timescales are position independent. In wall-bounded flow, however, turbulence is strongly inhomogeneous and anisotropic in the boundary layer, which implies some modification of the Langevin equation is in order.

First, one must take the impact of turbulence inhomogeneities into account. Without this correction tracer-like particles will diffuse in a non-physical way and induce errors as high as 550 % in simple flows. The inclusion of the drift acceleration into the Lagrangian equation dramatically decreases these errors. With $a_i = u_j \frac{\partial u_i}{\partial x_j}$ the instantaneous acceleration of a fluid particle, the drift acceleration is defined as followed:

$$\bar{a}_i = a_{i,mean} + a_{i,drift} = \bar{u}_j \frac{\partial \bar{u}_i}{\partial x_j} + \overline{u_j' \frac{\partial u_i'}{\partial x_j}}$$

The drift acceleration gives rise then to a drift velocity that one needs to add in the Langevin equation to take into account turbulence inhomogeneities:

$$\delta u_i = \overline{u_j' \frac{\partial u_i'}{\partial x_j}} dt = \frac{\partial \overline{u_j' u_i'}}{\partial x_j} dt$$

To arrive at the second equality, it is necessary to assume a divergence-free fluctuating velocity field, which is reasonable for the incompressible flows addressed in this investigation.

However, the previous expression of the drift velocity is valid for a fluid particles and thus for tracer-like particles only. For inertial particles a correction is in order. One can show that the drift correction for an inertial particle can be obtained from the drift correction of a fluid particle through a multiplicative factor as follow:

$$\delta u_i = \frac{\overline{\partial u_j' u_i'}}{\partial x_j} \cdot \left(\frac{1}{1 + Stk} \right) \cdot dt$$

with:

$$Stk = \frac{\tau_p}{\tau_L} : \text{particles Stokes number}$$

τ_L : Lagrangian time scale (to be specified)

τ_p : Particle relaxation time

Thus the Langevin equation can be written as follows:

$$du_i' = -u_i' \cdot \frac{dt}{\tau_i} + \sigma_i \sqrt{\frac{2}{\tau_i}} \cdot d\xi_i + \frac{\overline{\partial u_j' u_i'}}{\partial x_j} \cdot \left(\frac{1}{1 + Stk} \right) \cdot dt$$

Secondly, the Langevin equation is normalized in order to better account of both the inhomogeneous and anisotropic nature of the turbulence in the boundary layer:

$$d\left(\frac{u_i'}{\sigma_i}\right) = -\left(\frac{u_i'}{\sigma_i}\right) \cdot \frac{dt}{\tau_i} + \sqrt{\frac{2}{\tau_i}} \cdot d\xi_i + \frac{\partial \left(\frac{\overline{u_j' u_i'}}{\sigma_i} \right)}{\partial x_j} \cdot \left(\frac{1}{1 + Stk} \right) \cdot dt$$

Finally a distinction is made between turbulence in the bulk flow and in the boundary layer:

→ In the bulk flow the turbulence is considered isotropic so :

$$\sigma_1 = \sigma_2 = \sigma_3 = \sigma = \sqrt{\frac{2k}{3}}$$

After simplifications the Langevin equation became:

$$d\left(\frac{u_i'}{\sigma}\right) = -\left(\frac{u_i'}{\sigma}\right) \cdot \frac{dt}{\tau_L} + \sqrt{\frac{2}{\tau_L}} \cdot d\xi_i + \frac{1}{3\sigma} \frac{\partial k}{\partial x_j} \cdot \left(\frac{1}{1 + Stk} \right) \cdot dt$$

with:

$$\tau_L = \frac{2}{C_0} \frac{k}{\varepsilon}$$

→ In the boundary layer flow the turbulence is anisotropic and a distinction must be made between the directions. After simplifications and some hypothesis the Langevin equation becomes :

$$\begin{aligned} d\left(\frac{u'_1}{\sigma_1}\right) &= -\left(\frac{u'_1}{\sigma_1}\right) \cdot \frac{dt}{\tau_L} + \sqrt{\frac{2}{\tau_L}} \cdot d\xi_1 + \frac{\partial\left(\frac{u'_1 u'_2}{\sigma_1}\right)}{\partial x_2} \cdot \left(\frac{1}{1+Stk}\right) \cdot dt \\ d\left(\frac{u'_2}{\sigma_2}\right) &= -\left(\frac{u'_2}{\sigma_2}\right) \cdot \frac{dt}{\tau_L} + \sqrt{\frac{2}{\tau_L}} \cdot d\xi_2 + \frac{\partial\sigma_2}{\partial x_2} \cdot \left(\frac{1}{1+Stk}\right) \cdot dt \\ d\left(\frac{u'_3}{\sigma_3}\right) &= -\left(\frac{u'_3}{\sigma_3}\right) \cdot \frac{dt}{\tau_L} + \sqrt{\frac{2}{\tau_L}} \cdot d\xi_3 \end{aligned}$$

where the subscripts 1, 2 and 3 stand for streamwise, wall-normal and spanwise directions, respectively.

As for the DRW model, $\sigma_1, \sigma_2, \sigma_3$ and τ_L are calculated as functions of y^+ and u^* with correlations extracted from DNS results:

$$\begin{aligned} \sigma_1^+ &= \frac{\sigma_1}{u^*} = \frac{0.40y^+}{1 + 0.0239(y^+)^{1.496}} \\ \sigma_2^+ &= \frac{\sigma_2}{u^*} = \frac{0.0116(y^+)^2}{1 + 0.203y^+ + 0.00140(y^+)^{2.421}} \\ \sigma_3^+ &= \frac{\sigma_3}{u^*} = \frac{0.19y^+}{1 + 0.0361(y^+)^{1.322}} \\ \tau_L^+ &= \tau_L \cdot \frac{u^{*2}}{\nu} = 7.122 + 0.5731y^+ + 0.00129(y^+)^2 \text{ for } 5 < y^+ \leq 100 \\ &= 10 \text{ for } y^+ \leq 5 \end{aligned}$$

Thus, the CRW model gives a more physical representation of particles dispersion by turbulence than the DRW model. The shortcomings of the latter are solved this way.

1.2 Previous investigations

Even if computational modelings of particles deposition on arrays of spheres have never been investigated in detail several studies linked to such subject have already conducted. This chapter briefly summarize them beginning by the ones concerning flows past spheres (both experimental and numerical), then speaking about experimental measurements of particles deposition on arrays of spheres.

1.2.1 Flow past a single sphere

Many investigations on uniform flows past a sphere have been conducted both experimental and numerical.

In order to characterize this kind of flows many dimensionless number are used. The more common ones are:

→ The pressure and friction coefficients (defined locally and only on a wall):

$$C_p = \frac{P - P_\infty}{\frac{1}{2} \rho_f u_\infty^2} \quad \& \quad C_f = \frac{\tau}{\frac{1}{2} \rho_f u_\infty^2}$$

With:

P : wall pressure

τ : wall shear stress

u_∞ & P_∞ : main stream flow velocity and pressure

ρ_f : fluid density

→ The drag coefficient (defined for all the sphere):

$$C_d = \frac{F_D}{\frac{1}{2} \rho_f u_\infty^2 S}$$

With:

F_D : total drag force

S : projected sphere surface

There also exists another expression of the friction coefficient:

$$\tilde{C}_p = \frac{\tau}{\rho_f u_\infty^2} * \sqrt{Re}$$

With:

Re : sphere Reynolds Number

In the on hand, because of the many experimental investigations value of the drag coefficient C_D for a sphere in a uniform flow is known for a wide range of Reynolds number values (Figure 2).

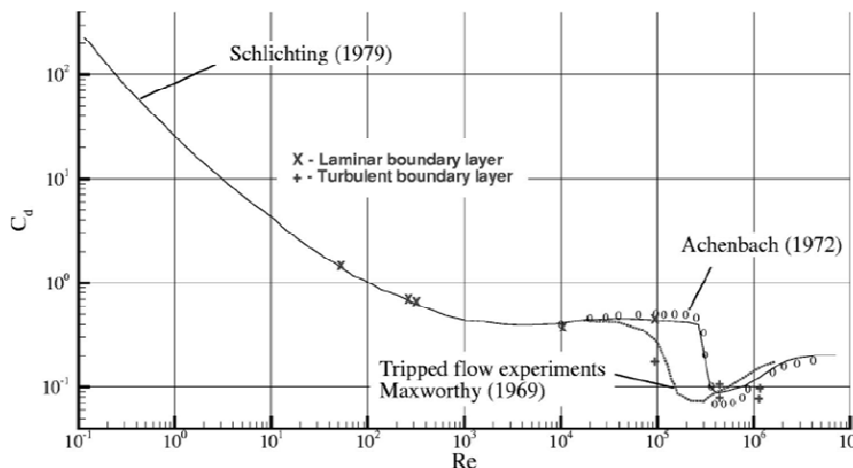


Figure 2 : Drag coefficient for uniform flow past a sphere

C_D passes through five phases as the Reynolds number increases:

- For $Re < 1$ the flow is laminar and symmetric (Stokes flow). The drag coefficient can be calculated analytically and is equal to:

$$C_D = \frac{24}{Re}$$

- For $1 < Re < 1000$ the drag coefficient continues decreasing but the influence of the Reynolds number also decrease.
- For $3 \cdot 10^3 < Re < 2.5 \cdot 10^5$ the drag reach a plateau and stays constant all over this range. Its empirical value is around 0.4. This range is also interesting because the flow field around the sphere concerning the form and the extension of the wake can be considered uniform to a great extend. This range is called the sub-critical regime.

- For $Re \approx 2.5 \cdot 10^5$ the drag coefficient abruptly decreases from 0.4 to less than 0.1. This is due to the boundary layer transition from laminar to turbulent.
- For $Re > 2.5 \cdot 10^5$ the flow is fully turbulent and the drag coefficient start increasing.

Experimental investigations made by E. Achenbach [4] give the values of pressure coefficients and friction coefficients on the surface of the sphere for a sub-critical value of Re (Figure 3).

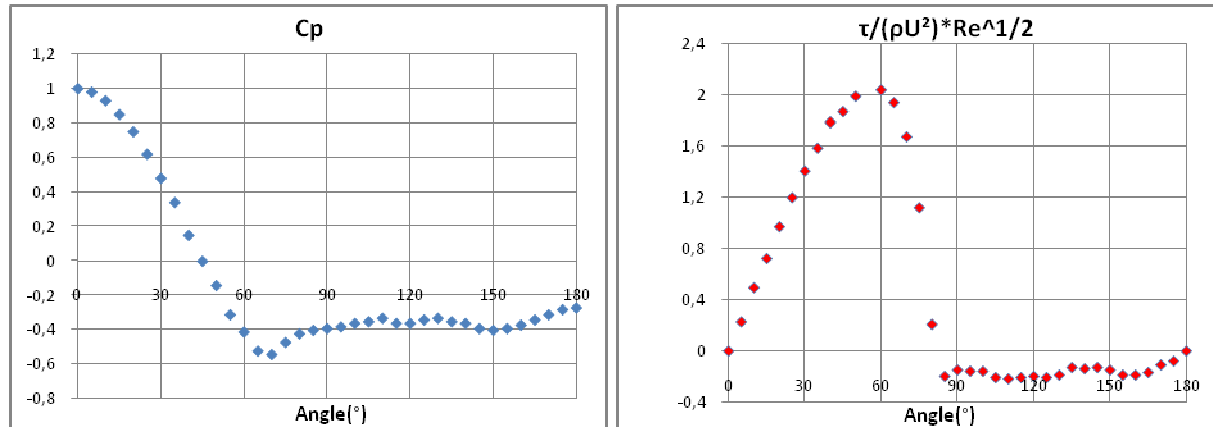


Figure 3: Sphere wall's coefficients at $Re = 165,000$

These two curves have been proven to be constant all over the sub-critical regime.

A more recent study made by Y. Jang [5] gives visualization of the flow structure around a sphere for $Re = 11,000$ (Figure 4).

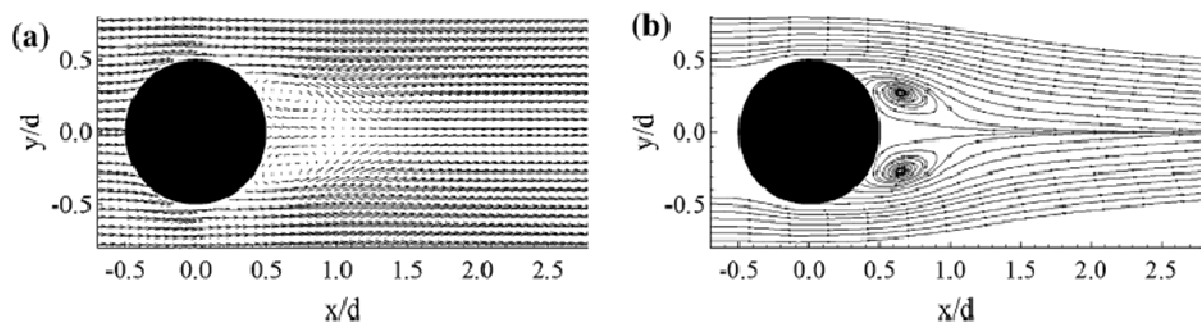


Figure 4 : Flow past a sphere at $Re = 11,000$; mean flow field velocity and stream lines

In the other hand many numerical investigations have been conducted on flow past sphere in order to benchmark turbulence models used with RANS equations or to validate results obtain with LES and DES computations. This is indeed a very good and simple example of flow past a bluff body with massively detached flow and moving boundary layer separation.

For example G. Constantinescu and K. Squire [6] & [7] made 3D computations using unsteady RANS equations with several turbulence models like $k-\epsilon$ and $k-\omega$. They made also computations using LES and DES. They results shows that URANS predictions of the pressure coefficient, skin friction and streamwise drag were in reasonable agreement with measurements, and predictions of turbulence kinetic energy and the shear stress were

similar to LES and DES results. However URANS solutions did not adequately resolve shedding mechanisms while LES and DES manage to resolve a large part to the vortex shedding process.

1.2.2 Particles deposition on spheres

Few experiments have been conducted on particles deposition on spheres. That is why, in order to benchmark our particles tracking simulations, the works of F. Hähner [9] and M. Waldenmaier [10] & [11] have been used exclusively.

In these two investigations the same experimental set ups were used. The gas used was air, the particles were made of DES (Di-II-ethyl-hexyl-sebacate) and the spheres were in steel. A first experimental set up (Figure 5a) was used for low Stokes number (between 0.03 and 0.5), then a second one (Figure 5b) was used for high Stokes number (between 0.4 and 5).

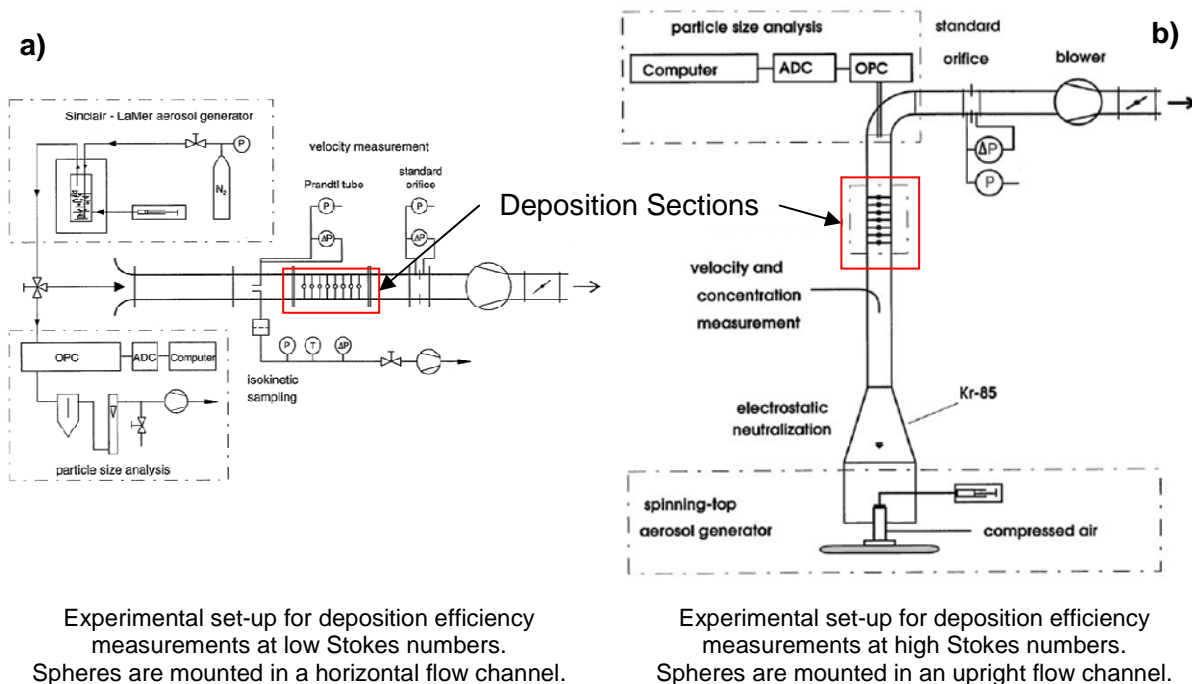


Figure 5 : Experimental set ups for particles deposition measurement on spheres

Both Hähner [9] and Waldenmaier [10] conducted particles deposition measurements on single sphere for a wide range of particles Stokes number. Hähner [9] carried out particles deposition measurements on linear array of spheres with two different spacing while Waldenmaier [10] conducted particles deposition measurements on linear arrays of spheres with a third spacing.

As no bounce occurs for DES impaction on steel every particle touching the spheres stays on it. That is why the measurement of particles deposition a sphere has been performed by weighting it before and after the experiment. Thus the mass of DES deposited on the sphere is calculated. This technique probably gives precise enough results if the collection efficiency of the sphere is high enough by for very low deposition this method seems to lead to a important scattering of the data (see Figure 42).

It is the results from these two investigations which have been used for benchmarking the present numerical method. The experimental data are presented in detail later in this report.

At last, the PHD works completed by Margaret Msongi Mkhosi [12] in 2007 present a first attempt to predict particles deposition on pebble bed using computational simulations. During her investigations she conducted particle deposition calculations on linear arrays of spheres using a flow solved with a 2d CFD-RANS method and the FLUENT's DRW tracking model. However calculations have been conducted using only one value for Re and for Stk .

1.3 Objective and resources

As said in the introduction, the main aim of this study is to benchmark a computational method which has been put together to calculate particles deposition on spheres. This method uses a CFD-solved flow coupled with a Lagrangian particle tracking model. The experimental data used to benchmark the method came from particle deposition measurements on spheres. Both the theoretical aspects of the method and the experiments have been presented in the first part of this report.

In order to apply the numerical method to particles deposition calculation on spheres one has to proceed in two steps:

1. Flow simulation: flows past spheres in geometries equivalent to the experimental set ups have to be solved (geometries modeling and meshing, flows computing, and results verification).
2. Particles tracking: using the flows solved in the first step particles tracking and deposition calculations have to be conducted.

Benchmarking of the numerical method is then carried out by comparing the computed results and the experimental data.

The resources used to carry out this investigation are:

- Gambit 6.3 for the meshing
- Fluent 12 for the CFD calculations and particles tracking (an UDF has been added to Fluent in order to do particle tracking using a CRW model)
- Paraview 3.2 and Excel for results post treatments and particles deposition calculations

The flows were solved using four processors running in parallel and sometime eight when they were available. It took around 3 days of calculation to solve a flow with 8 spheres.

The two next parts of this report describe the steps carried out while applying and benchmarking the numerical method and give the main results obtained.

2 Flow Simulation

In this study the discrete phase is modeled using a Lagrangian method (tracking a large number of individual particles). Moreover we assume that the particles concentration is low enough to use a one way coupling model. Thus one has to solve the continuous phase before doing any particle tracking calculation. This part of the report presents the method we used to obtain the different flows.

2.1 Geometry and mesh

The main aim of this study is to reproduce with numerical simulations the experiments made by Hähner [9] and Waldenmairer [10] as regard particle deposition measurement on single spheres or arrays of spheres. Then the experimental set ups geometries have to be modeled. This chapter explains how the geometries have been selected and the method used to mesh them.

2.1.1 Geometry

Here what we know about the collectors geometry:

- ✓ Deposition experiments were carried out in a pipe of 0.1 m diameter
- ✓ The collectors were composed of single sphere or linear arrays of eight spheres in strait line parallel to the direction of the flow.
- ✓ The spheres diameter ranged from 3mm to 9mm
- ✓ Linear arrays were characterized by the dimensionless spheres distance L/D (L=distance between two successive sphere centers, D=sphere diameter); this parameter was set equal to 1.5, 2 or 6.

Moreover, we know about the flow that:

- ✓ The Reynolds number based on the sphere diameter ranged from 3 000 to 12 000
- ✓ The inlet fluid velocities ranged from 5 ms^{-1} to 28 ms^{-1}

As regard the flow, the important parameter for particles deposition is the Reynolds number based on the sphere diameter. Moreover changing the spheres diameter from one geometry to another is not a good idea because one will need much more meshing in the end. Thus the spheres diameter has been set common to all the geometries and the inlet velocity has been changed according to the Reynolds Number. In order to respect the inlet velocity range given by Waldenmairer [10] we choose $D=6.5\text{mm}$ (moreover 6.5 mm is a value used in many of the experimental set ups). Then:

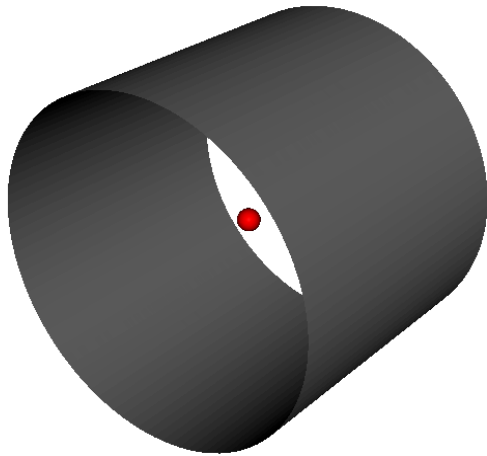
$$\begin{aligned} Re = 3\,000 &\Rightarrow u_0 = 6.75 \text{ ms}^{-1} \\ Re = 12\,000 &\Rightarrow u_0 = 27 \text{ ms}^{-1} \end{aligned}$$

In conclusion, 4 geometries have to be built and meshed:

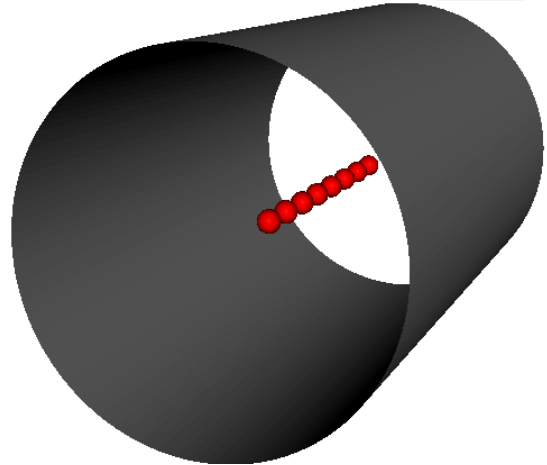
- ✓ One single sphere of $D=6.5 \text{ mm}$ diameter in a pipe of 0.1 m diameter
- ✓ 8 spheres with $L/D=1.5$ and $D=6.5 \text{ mm}$ in a pipe of 0.1 m diameter
- ✓ 8 spheres with $L/D=2$ and $D=6.5 \text{ mm}$ in a pipe of 0.1 m diameter
- ✓ 8 spheres with $L/D=6$ and $D=6.5 \text{ mm}$ in a pipe of 0.1 m diameter

In order to let the particles reach a steady state in the inlet we set a distance of $7D$ in front of the first sphere.

The Figure 6 shows a 3d view of two geometries that have to be meshed.



Single sphere

8 spheres with $L/D=2$ **Figure 6 : Examples of global geometries**

2.1.2 Meshing

4 geometries have been selected so at least 4 grids have to be created. Moreover, for every geometry simulations with various Reynolds Number have been performed. Then more than one grid per geometry is needed. The best solution to reduce the mesh creation time is to write a parametric Gambit Journal File which allows one to quickly build any mesh needed.

All the geometries chosen are made of one or eight spheres in a cylinder. So only the inlet and the first half of the first sphere have to be meshed. Then the final geometry will be obtained by copying this mesh as many times as needed.

Thus the only part that needs to be meshed is represented Figure 7.

**Figure 7 : Base geometry**

Moreover this geometry is X-axisymmetric so one can cut it in four quarters and mesh those four parts exactly in the same way. So finally the only part that truly needs to be meshed is represented Figure 8.

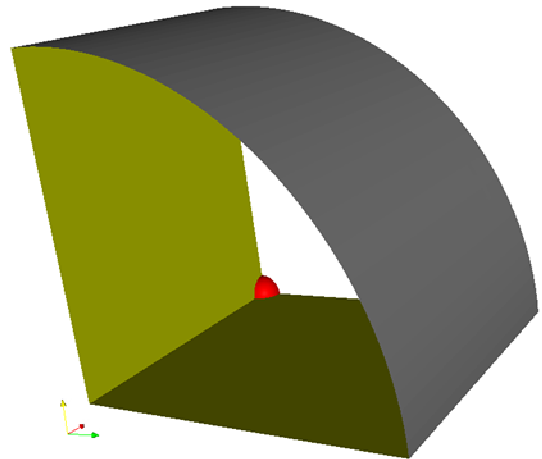
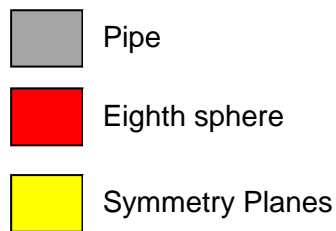


Figure 8 : Reduced base geometry

From this point the easiest solution is to define boundary layers for sphere and wall and fill the interior with unstructured tetrahedral meshing.

However, in order to have a better control on the grid and to reduce the calculation time I decided to divide the domain in sub volumes and mesh them with structured hexahedral meshing as much as possible:

The volume is first divided in four parts as on Figure 9.

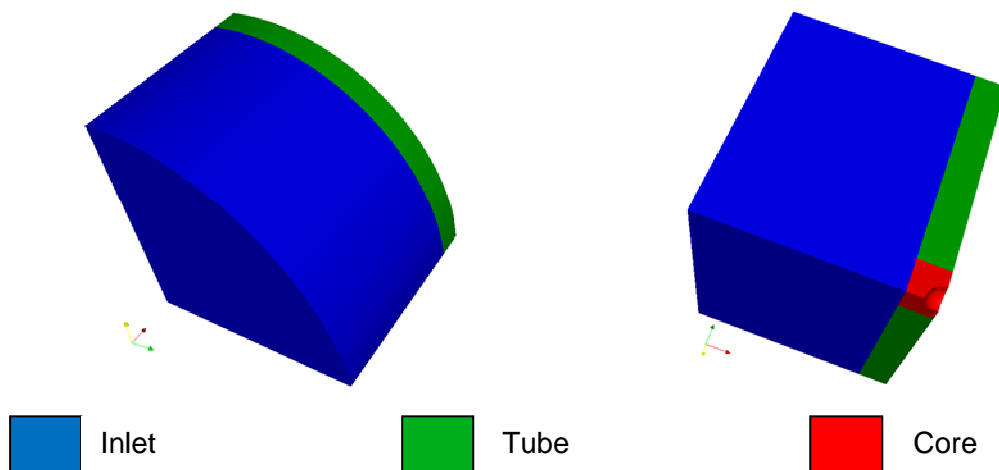


Figure 9: Base geometry subdivision

Comment: The Core volume is an X-axis cylinder such as Radius = Height.

Now that all the volumes are defined the mesh can be created.

- Meshing of Core :

This part is the most difficult to mesh for the mesh has to go from the surface of a sphere to the surface of a cylinder.

Because of that the volume cannot be meshed entirely with structured mesh. However, this volume can be again divided into two sub volumes (Figure 10).

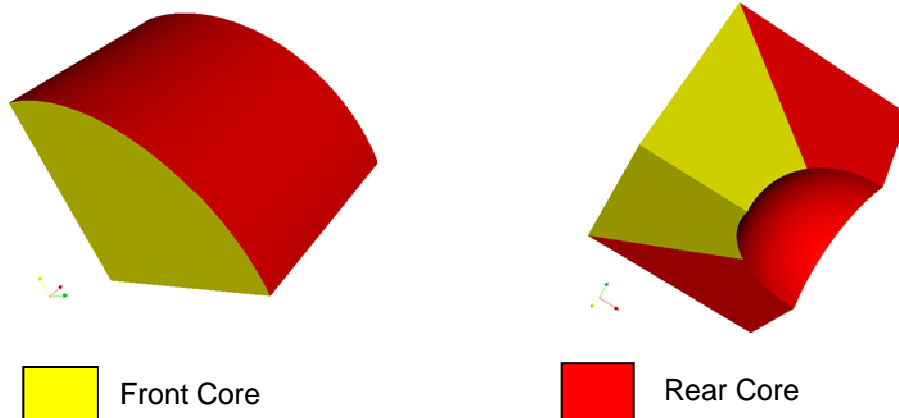


Figure 10 : Core volume

While the front part cannot be meshed with a structured mesh the rear part can. The two volumes are defined such as the interface between them is normal to the sphere surface and cut it in the middle (Figure 11).

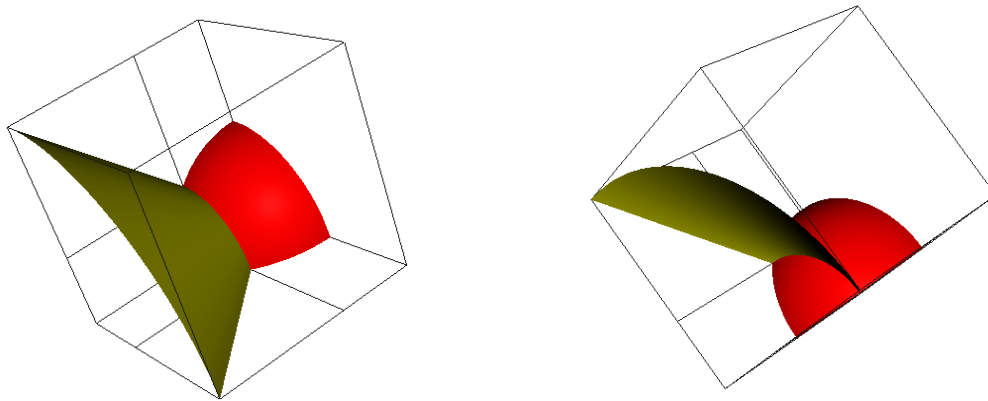


Figure 11 : Core volume subdivision

First, one has to define the sphere's boundary layer. Here, the boundary layer is characterized by 3 parameters (Figure 12).

- Fr : First row thickness
- R : Growth factor
- Nr : Number of rows

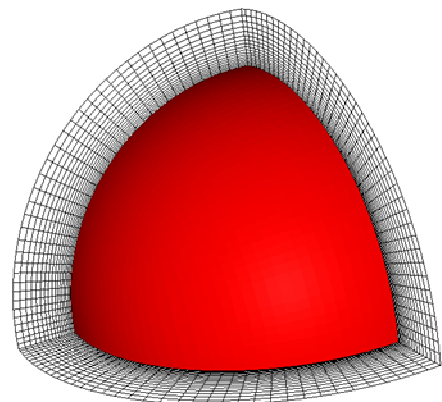


Figure 12 : Sphere boundary layer definition

Comment: Different parameters can be defined for the pipe's boundary layer. However we choose to use the same ones.

Then the Core volume can be meshed, first the front part then the rear part (Figure 13).

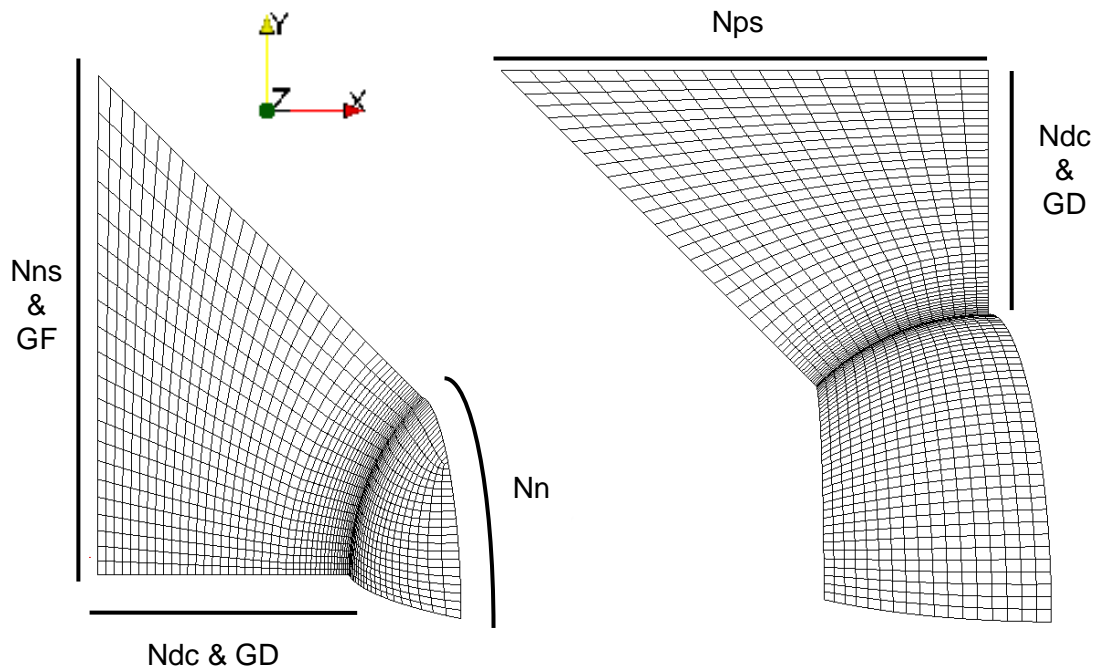


Figure 13 : Core meshing

Comment: The volume meshing is created by rotation of the surface meshing around the X axis.

Core mesh parameters are:

- N_n : Number of cells in the circular direction
- N_{ns} & GF : Number of cells and growth factor in front of the sphere in the radial direction (in order to have a more regular mesh one needs to set $N_{ns} = N_n/2+1$).
- N_{dc} & GD : Number of cells and growth factor in front of the sphere in the axial direction ($N_{dc} > N_r$ because the boundary layer cells are counted in N_{dc} and GD is the growth factor outside the boundary layer).
- N_{ps} : Number of cells above the sphere in the axial direction

Comment: The axial, radial and circular directions refer to the pipe (cylinder) and not to the sphere.

Now that Core is meshed one has to mesh Tube and Inlet (Figure 14 and Figure 13). But many of the parameters have already been fixed while meshing Core.

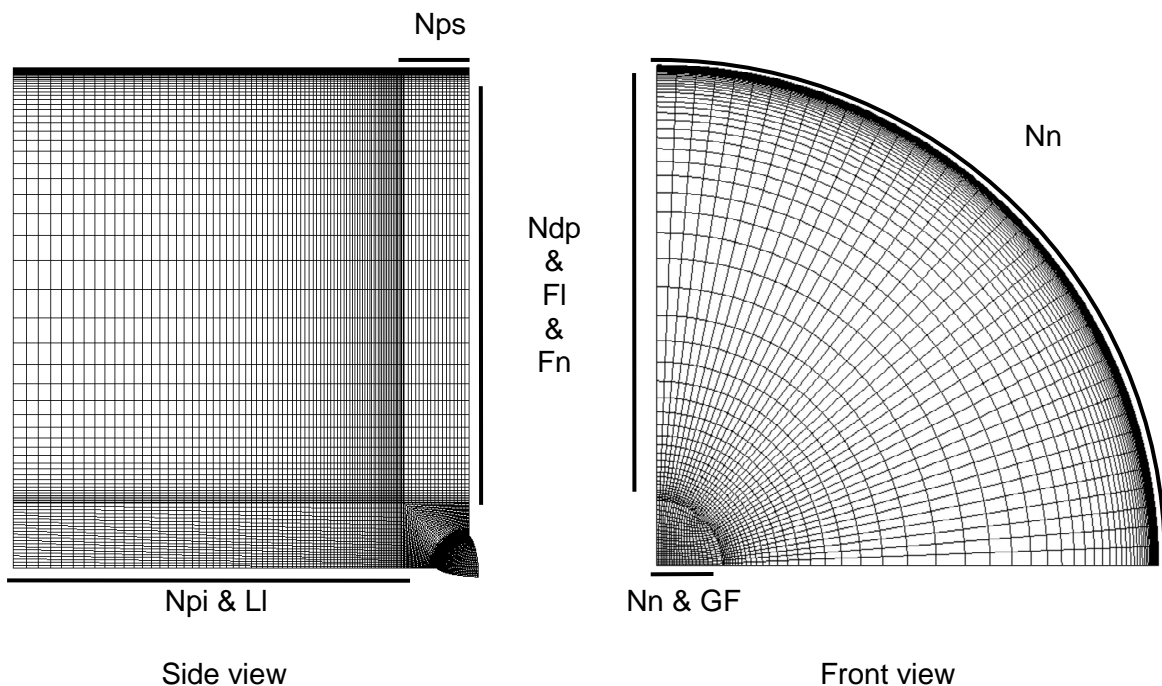


Figure 14 : Tube and inlet meshing

The only new parameters needed are:

- Ndp, Fi and Fn: Number of cells (Ndp>Nr because the pipe's boundary layer cells are counted in Ndp), first row size outside Core and first row size outside the pipe's boundary layer in the radial direction.
- Npi & Li: Number of cells and first row size outside Core in Inlet in the axial direction.

Comment: The only surface not meshed with structured mesh is the middle front of the sphere (Figure 15). However the mesh here is not far from structured.

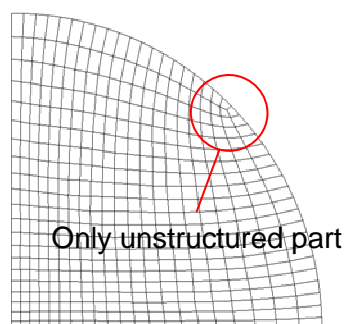


Figure 15 : Middle front of the sphere's mesh

Now that the base geometry is meshed one can copy it as much as needed to create the final geometries. For example in order to create a geometry with two spheres one can proceed as illustrated Figure 16.

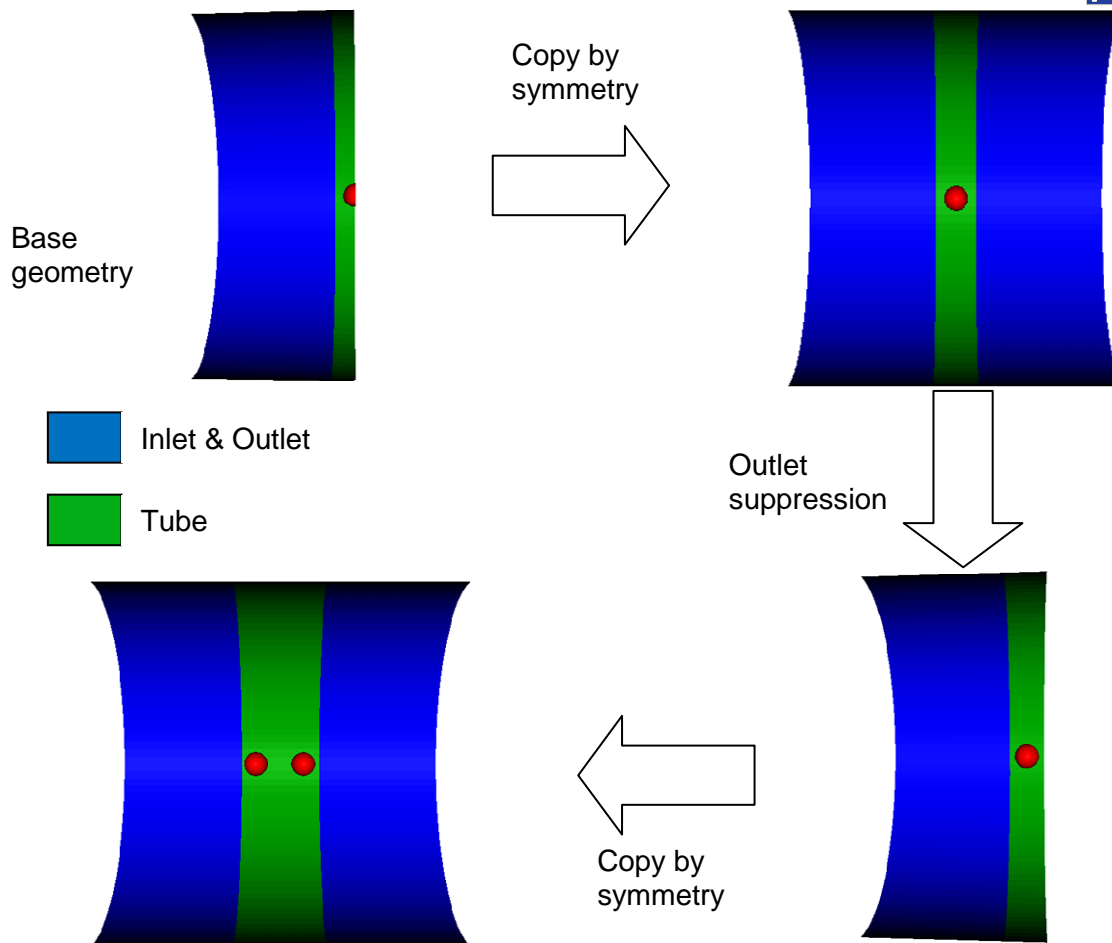


Figure 16 : Global geometry construction method

Comment: With this method only a peer number of spheres can be created.

As seen previously the geometries have various sphere spacing. In order to change this spacing the dimensions of the Core volume have to be set accordingly. For example for $L/D = 2$ the values of the Core Height must be D (Figure 17).

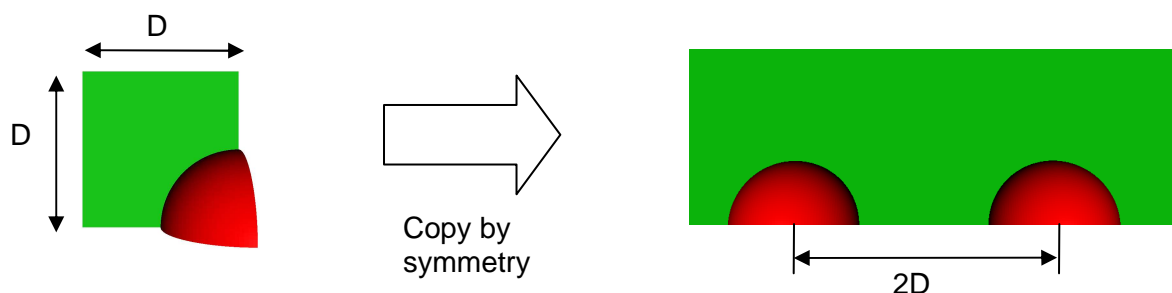


Figure 17 : Sphere spacing determination technique

In conclusion with 4 geometric parameters (spheres diameter, pipe diameter, inlet length and sphere spacing), 3 boundary layer's parameters and 10 grid parameters one can quickly create any geometry needed with any mesh refinement. The gambit journal files can be found in Annex 1.

2.2 Simulation overview

The different geometries have been selected and a meshing technique has been investigated. Then the flows have to be solved. In order to do that several steps have to be completed: choosing of the resolution method (LES, DES, RANS, ...) and the discretization schemes, making sure that the results are grid independents, checking if the solutions found don't presents some clearly absurd features. This chapter details all these steps.

2.2.1 Simulation generalities

All the CFD calculations were made using steady RANS equations. The choice of steady solutions can be contested while many experimental studies like Jang [5] have showed that unsteady phenomenon like vortex shedding take place in the wake of a sphere for this range of Reynolds Number. However, computing particles trajectories using an unsteady solution is much more time consuming that doing it in a steady one: the velocity field has to be modified at each increment of the particle tracking computation and the time step has to be adapted to both the particles and the velocity field. As regard the number of cases to be treated, using unsteady solutions would be too much time consuming. Moreover the stochastic nature of the particles tracking model obliges us to perform a large number of trajectory computation for each particle. If enough computations are made, using the mean flow extracted from the unsteady solution is equivalent to use directly the unsteady solution; yet steady computation gives us a mean solution of the real unsteady flow.

While using RANS equations one has to choose between several models of turbulence. This choice is important because not every model give good results on bluff body flows and computation time can be very different depending on the model used. Constantiescu [6] showed that some two-equations based model like the $k-\omega$ one give good results for flows around sphere without being too much time consuming. However, while modeling flow around a linear array of spheres many interactions between spheres and wakes take place. Therefore the flows can be much more complex than for a single sphere. Thus we decided to use the more powerful (and more time consuming) turbulence model we had in Fluent: a Reynolds Stress Model (RSM). All the computations have been done using this model.

No wall functions have been used: boundary layers are accurately resolved by the mesh.

The SIMPLE algorithm and the implicit formulation have been used. For the momentum and turbulence equations two spatial discretization schemes have been used: 2nd order UPWIND and 3rd order MUSCL. For the first computation the two have been tried in order to pick best one (accurate enough without being too much time consuming). The scheme then picked is the one used in all the others computations.

2.2.2 Boundary conditions

The geometries previously created have an inlet length of 7D. This is enough for the particles to reach a steady state but if one sets uniform boundary conditions in the inlet the flow doesn't have the time to be fully developed before meeting the first sphere.

Creating geometries with longer inlet would be a waste of computing time so one has to set an already developed flow as boundary condition in the inlet. In order to obtain the data for the boundary conditions computations have been made in a simple pipe of 0.1m radius and 20D length.

For this computation the inlet boundary conditions are constant on the profile. Three parameters have to be fixed:

→ Inlet Velocity:

Only the axial velocity has to be set, the other ones are considered null. Moreover the axial velocity is defined by Reynolds Number based on the sphere (which diameter is 6.5mm in all the geometries).

→ Turbulence parameters (Turbulence Intensity (I) and Turbulence Length Scale (l)):

These two parameters have been calculated using formulas extracted from the Fluent 6.3 User's Guide. For fully developed flows in pipes the guide gives the following expression:

$$I = 0.016 * (Re_t)^{-1/8}$$

$$l = 0.07 * D_t$$

With:

Re_t = Reynolds Number based on the tube diameter

D_t = tube diameter

One has just to create a tube of 0.1m radius and 20D length with Gambit, meshe it and solve the flow with the uniform inlet boundary conditions previously calculated. The outlet data can then be extracted and used in the main calculations (Figure 18).

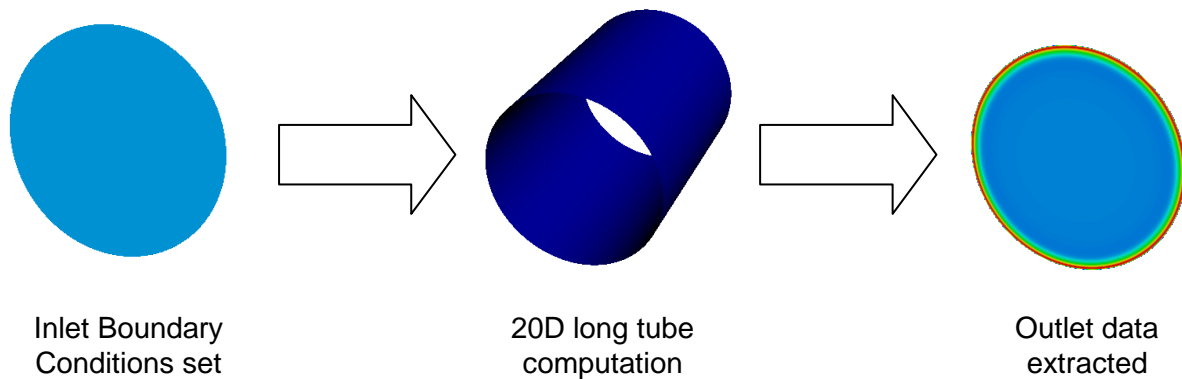


Figure 18 : Boundary condition calculation method

Comment: The tube is meshed in the same way than the inlet for the main geometries. The flow is resolved using a RSM turbulent model and a 3rd order MUSCL spatial discretization.

The table 1 summarizes all the inlet boundary conditions used in this study.

Re Sphere	u_0 (m/s)	Re tube	Turbulence Intensity (%)	Turbulence Length Scale (m)
3 000	6.75	46 000	4.2	0.007
5 000	11	75 000	3.9	0.007
6 000	14	96 000	3.8	0.007
8 300	18.7	128 000	3.7	0.007
12 000	27	184 000	3.5	0.007

Table 1: Boundary conditions values

Comment: In all the simulations diameter sphere (D) equal 6.5 mm and diameter tube (Dp) equal 0.1 m.

2.2.3 Flow fields past single spheres

Solving flow around single sphere has two aims:

1. Comparing the results obtained with the ones found in literature in order to verify if the method used here (grid, turbulence model, and simulation parameters) yield good enough results.
2. Obtaining the flows which will be used for the particles deposition calculations on single spheres.

The geometry is the same for all the single sphere cases:

- ✓ One single sphere of $D=6.5$ mm diameter in a pipe of $D_p=0.1$ m diameter.

Computations with three Reynolds Numbers have been made. Two of them have been deeply investigated ($Re = 5,000$ and $Re = 12,000$).

A. $Re = 5,000$:

Three meshes were created (table 2).

Grid	Cells Count	Boundary Layer	
		First Row Size (mm)	Growth Factor
coarse	678 720	0.020	1.1
medium	1 038 440	0.020	1.1
fine	1 622 400	0.020	1.1

Table 2 : Meshes for single sphere

The meshes parameters are detailed in Annex 2.

In a first time, the flow has been solved for these three meshes with the 3rd order MUSCL spatial discretization scheme (table 3).

Re	Grid	Convergence level	Mean y^+ wall	Drag Coefficient	Viscous Drag (%)
5 000	coarse	1.50E-08	0.69	0.549	12.6
5 000	medium	1.00E-09	0.68	0.548	12.6
5 000	fine	3.20E-09	0.68	0.548	12.6

Table 3 : Single sphere & $Re = 5,000$; simulations' main results

Comment: The colon *Viscous Drag* gives the proportion of the drag value which is due to viscous effects (in opposition to pressure effects).

We can deduce from this first table that the boundary layer first row is fine enough ($y^+ < 1$ on the wall) and the results seen to be grid independent (the streamwise drag differs in C_d by less than 1%). In order to verify this assumption wall values C_f & C_p are plotted Figure 19.

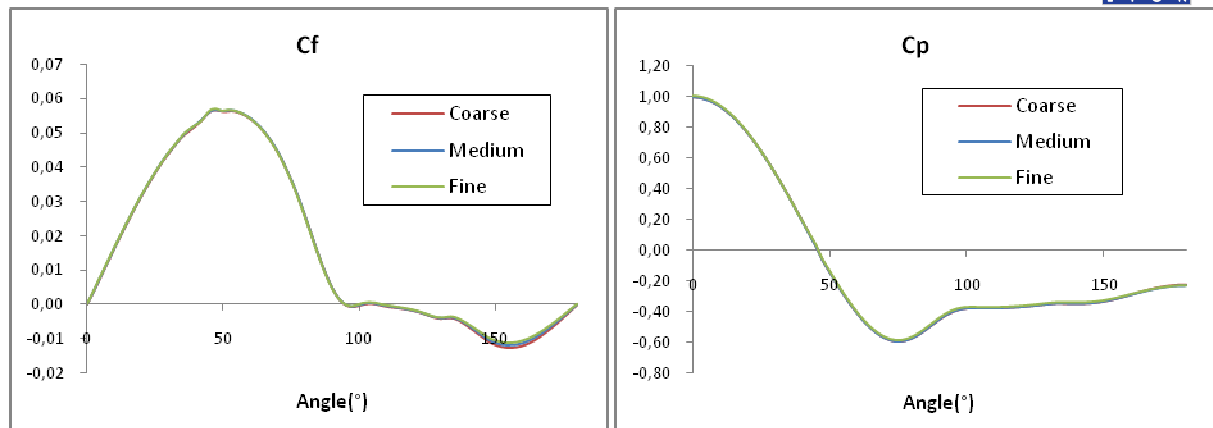


Figure 19 : Single Sphere & Re = 5,000; wall coefficients for grid independence

The results here are clearly grid independent.

However an accurate resolution of the wake is also important because in linear arrays wakes and spheres interact with each other. Then the grid independence of the results has to be checked in the wake to. Velocity Magnitude and Turbulent Kinetic Energy in the near wake ($x/D = 1.08$) are plotted Figure 20.

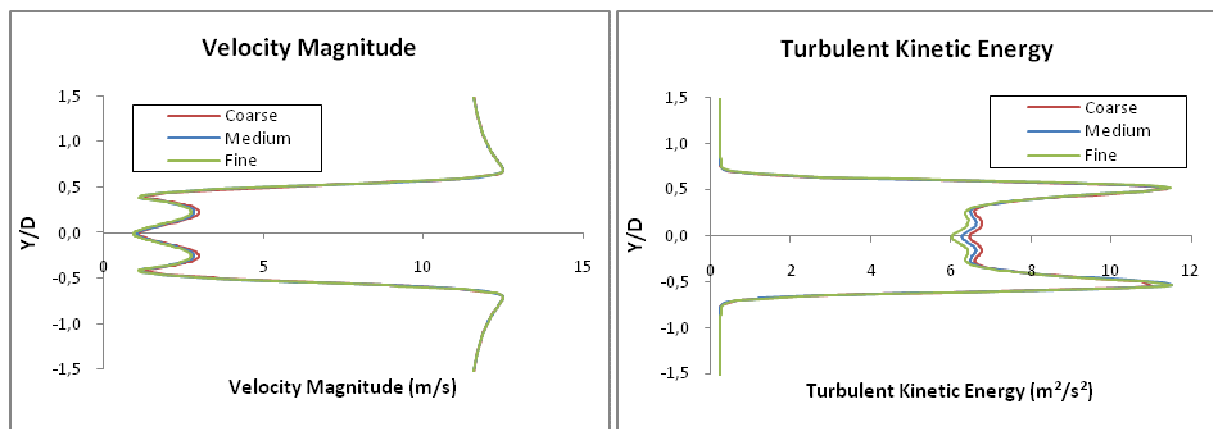


Figure 20 : Single sphere & Re = 5,000; wake values for grid independence

Wake values are not as grid independent as wall ones but they are still very close most of the time. The fine grid can be considered as fine enough for this regime.

One can also note that the worst results are obtained in the wake along the x-axis. Therefore the following grid comparisons are made using the values along this axe for they give us the upper limit of the difference.

Another thing that one has to check is the boundary layer resolution. The size of the first row has already been verified ($y^+ \approx 1$). Now the resolution of the viscous sub layer (y^+ below 20) has to be checked.

y^+ is defined such as :

$$y^+ = \frac{y * u^*}{\nu}$$

With:

u^* = wall shear velocity
 ν = cinematic viscosity
 y = wall normal distance

In Fluent, y^+ wall is defined as:

$$y^+_{wall} = \frac{Fr}{2} * \frac{u^*}{\nu}$$

With:

Fr = boundary layer first row size

Then:

$$y^+ = y^+_{wall} * \frac{2y}{Fr}$$

By using the mean value of y^+ wall given by Fluent one can represent the evolution of y^+ in the wall normal direction (Figure 21).

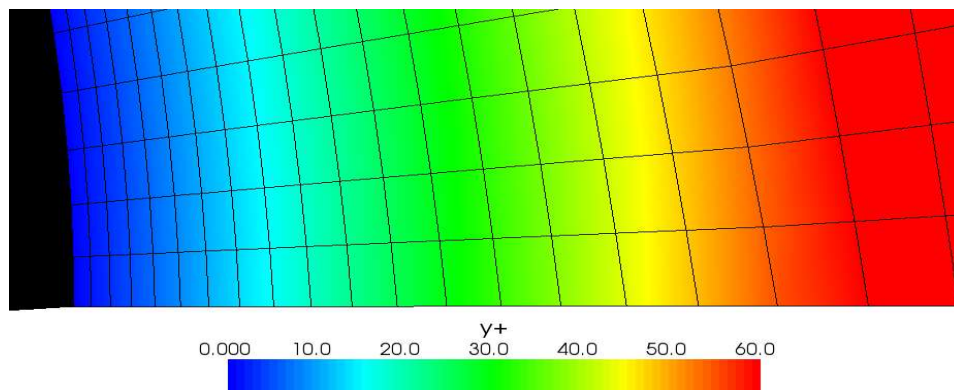


Figure 21 : Single sphere & Re = 5,000; boundary layer

Ten rows are inside the viscous sub-layer: the boundary layer resolution is fine enough.

The previous solutions have been obtained with a 3rd order MUSCL spatial discretization scheme. However, this scheme is more time consuming than a 2nd order UPWIND one. So one can check if a 3rd order discretization is needed or overrated.

The flow has been solved using the 2nd order UPWIND spatial discretization scheme with the fine mesh (table 4).

Re	Scheme Order	Grid	Convergence level	Mean y^+ wall	Drag Coefficient	Viscous Drag (%)
5 000	2	fine	2.00E-08	0.68	0.547	12.7
5 000	3	fine	3.20E-09	0.68	0.548	12.6

Table 4 : Single sphere & Re = 5,000; spatial discretization influence

The streamwise drag differs in C_d by less than 1%. Results extracted from the solutions are plotted Figure 22 and Figure 23.

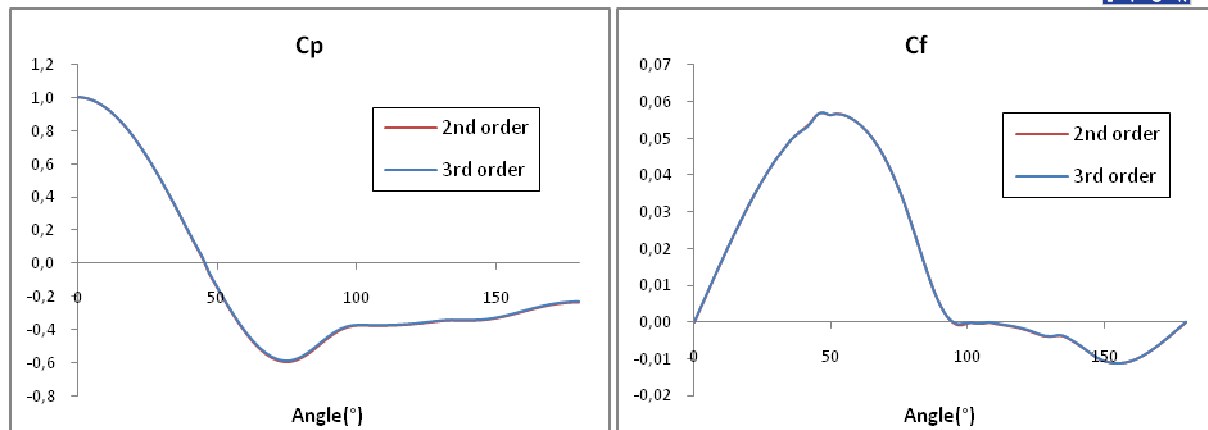


Figure 22 : Single sphere & Re = 5,000; wall coefficients for spatial discretization influence

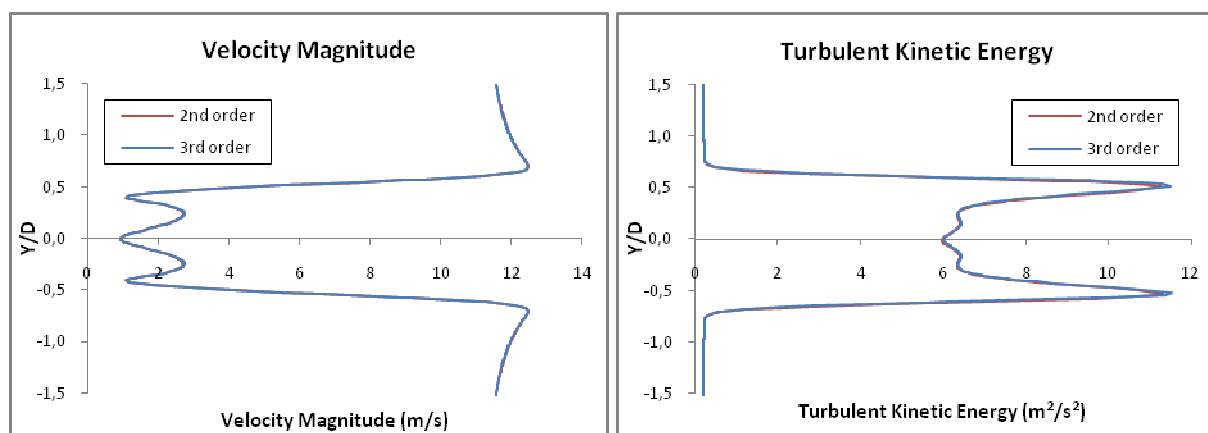


Figure 23 : Single sphere & Re = 5,000; wakes values for spatial discretization influence

The results obtained with 2nd and 3rd order are really close (difference always less than 1%); therefore it is useless to use the 3rd order spatial discretization scheme. The 2nd order one has been used in all the other simulation.

B. Re = 12,000:

Re = 5,000 and Re = 12,000 are both set in the Reynolds number range where the flow can be considered as uniform to a great extent. Then the grid independence investigation made previously for Re = 5,000 is still valid here. Then the flow has been solved using the fine mesh:

Re	Grid	Convergence level	Mean y^+ wall	Drag Coefficient	Viscous Drag (%)
12 000	fine	2.00E-07	1.41	0.47	8.8

Table 5 : Single sphere & Re = 12,000; simulation's main results

However the boundary layer resolution has to be checked again (Figure 24).

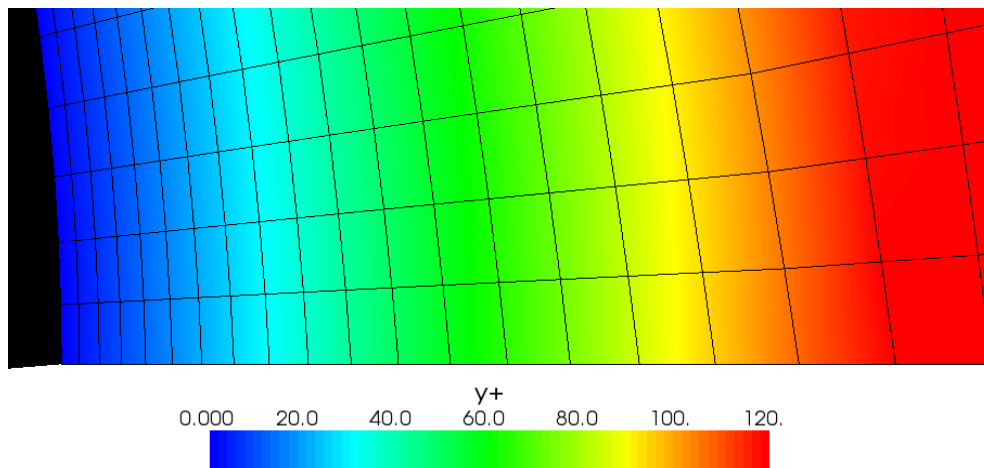


Figure 24 : Single sphere & $Re = 12,000$; boundary layer

Around six rows are inside the viscous sub-layer: the boundary layer resolution is still fine enough.

Unfortunately, a closer look at the normal velocity on a symmetry plane shows a very problematic limitation of the computation (Figure 25).

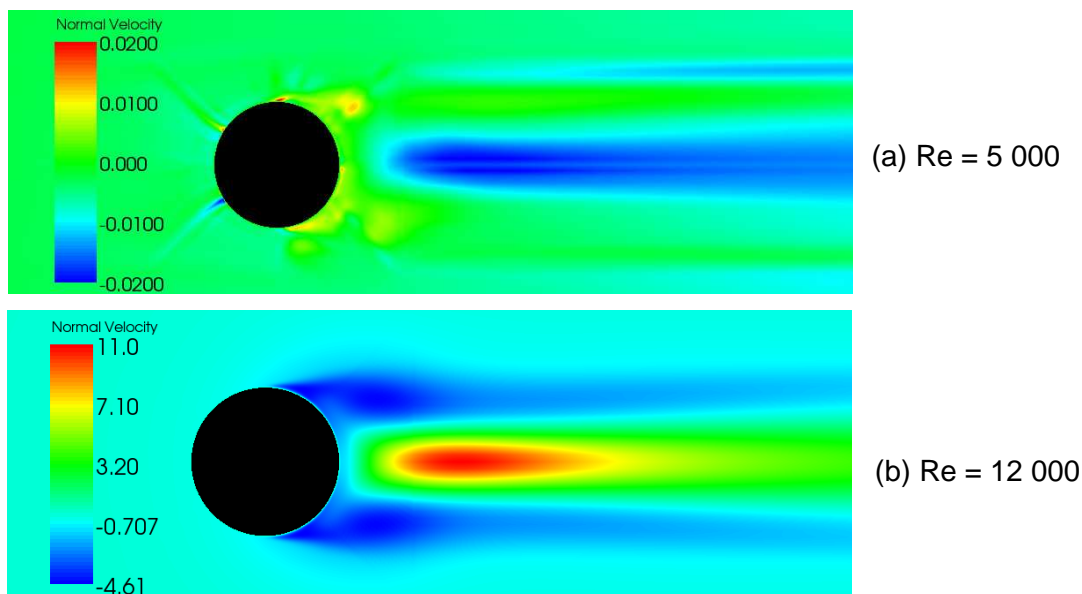


Figure 25: Normal velocity in the XY plane in percent of the inlet velocity magnitude

While for $Re = 5,000$ the velocity field is nearly symmetric (normal velocity magnitude below 0.01 % of the inlet velocity), for $Re = 12,000$ the normal velocity magnitude goes up to 11% of the inlet velocity while it should be null.

This asymmetric feature of the flow probably doesn't influence the particles deposition on the leading sphere. However deposition on the following spheres depends on the shape of the leading sphere's wake, which one is clearly wrong in our calculation. If particles tracking computations are made using this flow particles will be pushed away from the array by this unphysical phenomenon.

First we tried to solve this issue by increasing the grid resolution in the wake zone. One more mesh was then created (table 6).

Grid	Cells Count	Boundary Layer	
		First Row Size (mm)	Growth Factor
fine	1 622 400	0.020	1.1
finest	2 400 000	0.020	1.1

Table 6 : Finest mesh parameters for single sphere

The fine and finest mesh are identical except for the mesh streamwise resolution in the outlet zone ($x > 1.5D$). This resolution is twice as big in the finest mesh.

Then the flow has been solved using the finest mesh (table 6).

Re	Grid	Convergence level	Mean y^+ wall	Drag Coefficient	Viscous Drag (%)
12 000	fine	2.00E-07	1.41	0.47	8.8
12 000	finest	7.00E-09	1.33	0.47	8.9

Table 7: Single sphere & Re = 12,000; simulation results for finest grid

Results have been extracted from the surface of the sphere and from its wake along the x-axis and plotted Figure 26.

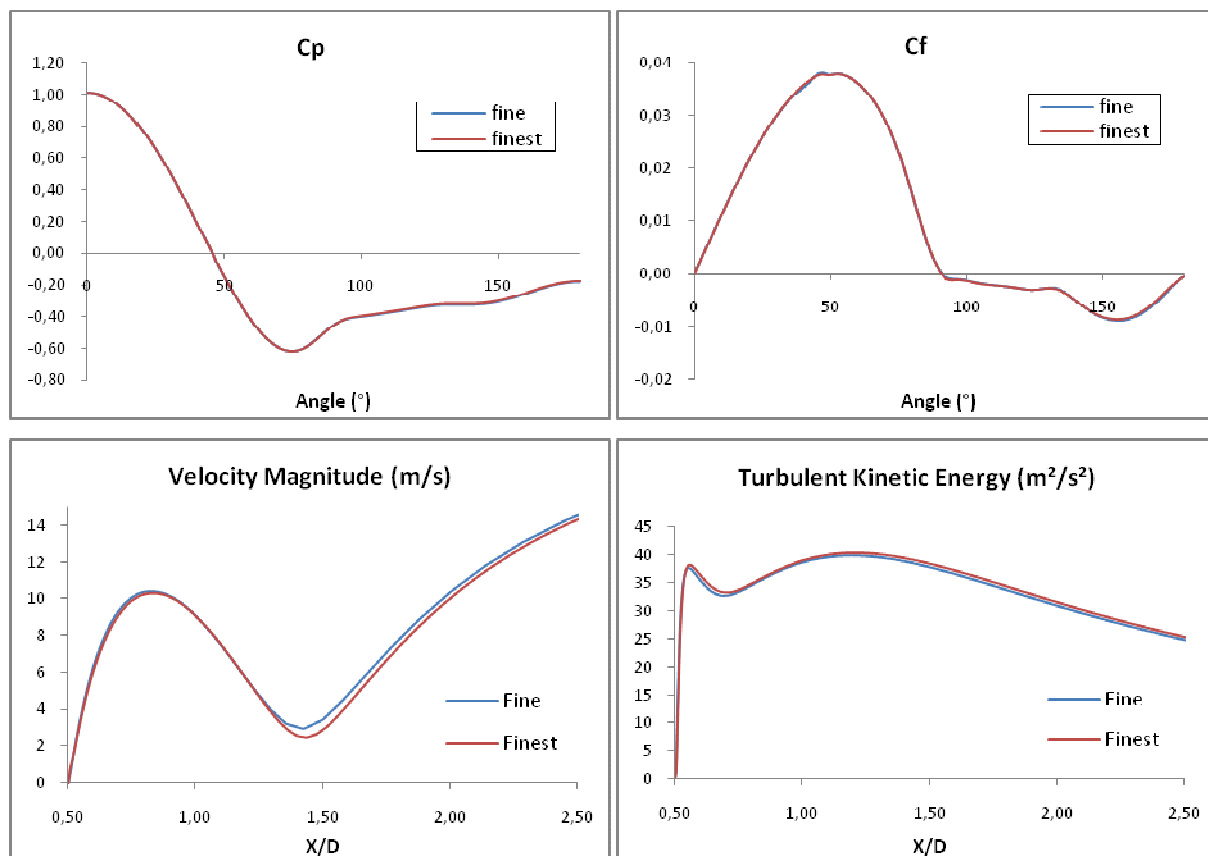


Figure 26 : Single sphere & Re = 12,000; results with finest grid

As expected the results are identical except for the Velocity magnitude in the wake. A closer look at the normal velocity shows that even if the new results are better they are still far from a symmetric flow (Figure 27).

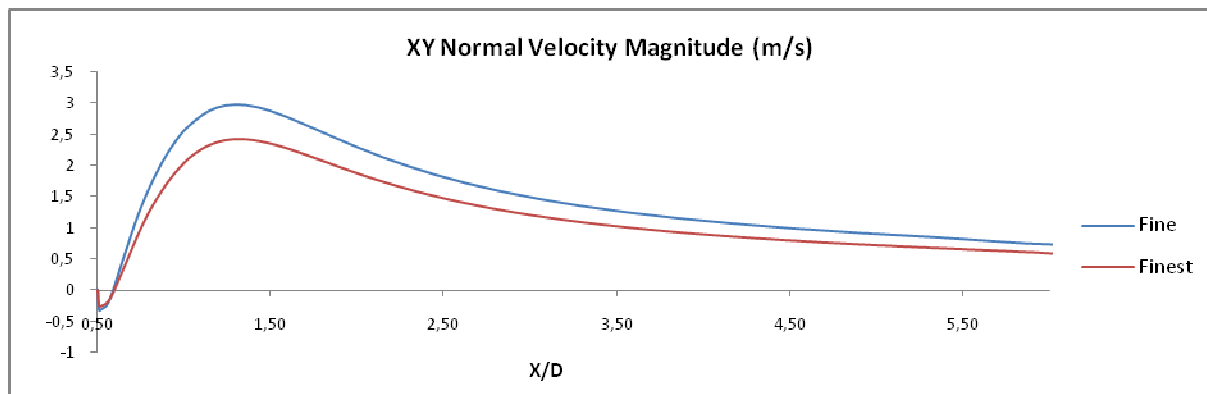


Figure 27 : Single sphere & $Re = 12,000$; normal velocity in the wake

The normal velocity still goes up to 9% of the inlet velocity which is still too much. Moreover refining the mesh fine until this parasite velocity is negligible leads to divergent calculations. Therefore a solution has to be found without further mesh refinement.

Another solution consists on doing 2D axi-symmetric simulations instead of full 3D ones. It will solve any kind of symmetry problems but unfortunately the CRW tracking model can only be implanted into a 3D flow.

Finally we decide to use the axi-symmetric proprieties of the flow while keeping a 3D solution: one quarter of the geometry is extracted and the flow is solved while imposing symmetric boundary conditions over the two symmetry planes (Figure 38).

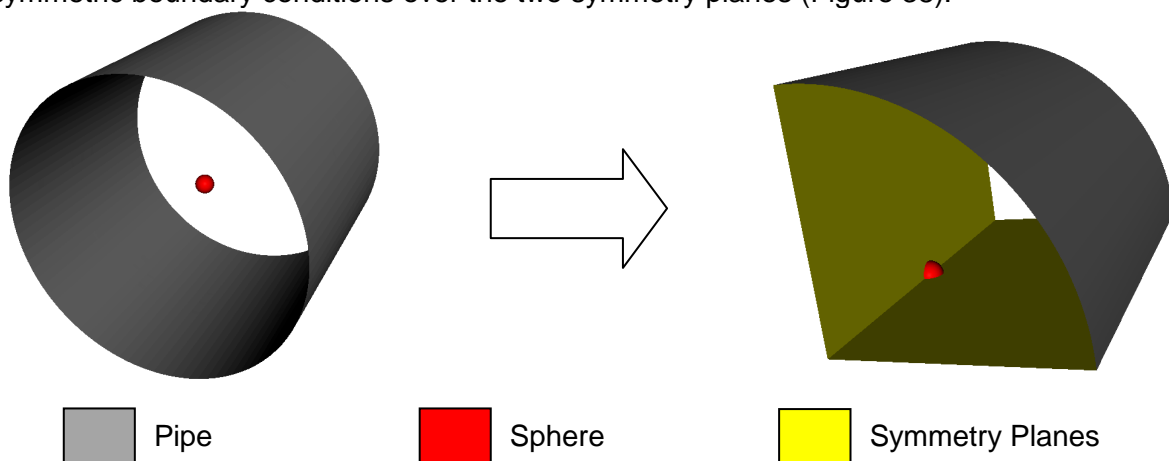


Figure 28 : Whole geometry to reduced geometry

Comment: all the geometries constituted of only one quarter of the real geometry are called **reduced** geometries.

This solution also saves us a lot of computing time as the mesh will be 4 times smaller. However the solutions equivalence between these two geometries has to be verified.

The reduced geometry has been meshed using mostly one quarter of the finest mesh (table 7).

Grid	Cells Count	Boundary Layer	
		First Row Size (mm)	Growth Factor
finest	2 400 000	0.020	1.1
quarter	664 400	0.020	1.1

Table 8 : Quarter mesh parameters

For $Re = 5,000$ the flow is solved for the whole geometry with the finest mesh and for the reduced geometry with the quarter mesh (table 8)

Re	Grid	Convergence level	Mean y^+ wall	Drag Coefficient	Viscous Drag (%)
5 000	finest	4.00E-08	0.65	0.544	12.8
5 000	quarter	4.00E-08	0.65	0.543	12.8

Table 9 : Single sphere & $Re = 5,000$; simulation's main results with quarter mesh

The streamwise drag differs in C_d by less that 1%.

Results were extracted from the surface of the sphere and from its wake along the x-axis and plotted Figure 29.

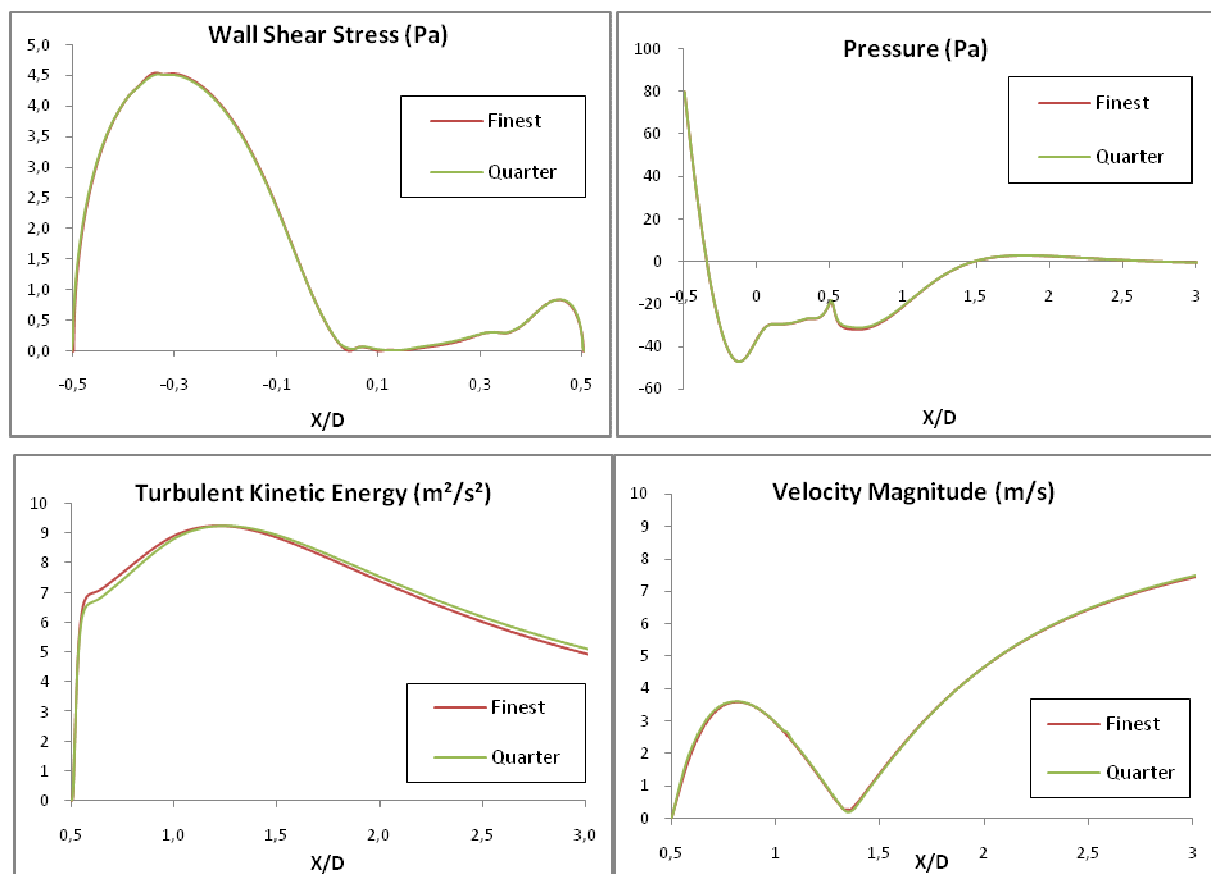


Figure 29 : Single sphere & $Re = 5,000$; results values with quarter mesh

The difference between the finest mesh and the quarter one is always inferior to 1% except for the turbulent kinetic energy in the wake of the sphere. Here the difference stays between 2 and 3 % with a maximum of 4% in the near wake. Therefore one can consider that the reduced geometry yields results comparable to the whole geometry ones.

For $Re = 12,000$, the flow is solved with the quarter mesh (table 9).

Re	Grid	Convergence level	Mean y^+ wall	Drag Coefficient	Viscous Drag (%)
12 000	finest	7.00E-09	1.33	0.469	8.9
12 000	quarter	3.40E-10	1.35	0.466	8.9

Table 10 : Single sphere & $Re = 12,000$; simulation's main results with quarter mesh

Thus one can verify if the asymmetry we had with the whole geometry is no longer an issue. Represented Figure 30 is the normal velocity magnitude into a (0, -1, 1) normal symmetry plane.

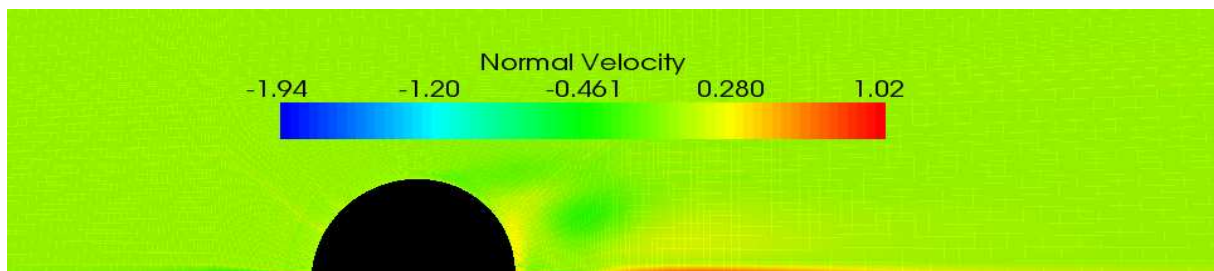


Figure 30 : $Re = 12,000$; Normal velocity in percent of the inlet velocity magnitude

The normal velocity is now below 1% of the inlet velocity. Moreover the surface where this normal velocity is significant is small.

In conclusion, even if the problem is not entirely solved the result is still quite better. From this point every simulation has been performed using one quarter of the whole geometry.

One last simulation with a single sphere has been performed at $Re = 3000$. The table 10 summarized the mains results obtained for single sphere cases:

Re	Grid	Convergence level	Mean y^+ wall	Drag Coefficient	Viscous Drag (%)
3 000	quarter	2.20E-10	0.45	0.579	16.0
5 000	quarter	4.00E-08	0.65	0.543	12.8
12 000	quarter	3.40E-10	1.35	0.466	8.9

Table 11 : Single sphere main results summary

Comment: These three simulations are the ones used for particles tracking.

2.2.4 Flow fields past linear arrays of spheres

Three geometries with a linear array of sphere have been treated:

- ✓ 8 spheres with $L/D=1.5$ and $D=6.5$ mm in a pipe of 0.1 m diameter
- ✓ 8 spheres with $L/D=2$ and $D=6.5$ mm in a pipe of 0.1 m diameter
- ✓ 8 spheres with $L/D=6$ and $D=6.5$ mm in a pipe of 0.1 m diameter

Comment: Each flow has been solved only in reduced geometry.

For each geometry the flow has been solved with more than two Reynolds number. Making a grid independence study for every case will be too much time consuming. Therefore such process have been applied only for the cases with the highest Reynolds Number ($Re=12\ 000$). Then it can be assumed that the mesh chosen is fine enough for lower Reynolds Numbers. Moreover the $L/D=2$ and $L/D=1.5$ geometries are very close so the grid independence study has been made only for $L/D=2$. For $L/D=1.5$ the mesh has been created using the parameters of the mesh with $L/D=2$.

→ $L/D = 2$ & $Re = 12\ 000$:

For this geometry three meshes were created (table 11)

L/D	Grid	Cells Count	Boundary Layer	
			First Row Size (mm)	Growth Factor
2	coarse	1 106 880	0.020	1.1
2	medium	1 636 800	0.020	1.1
2	fine	2 400 640	0.020	1.1

Table 12 : Meshes for 8 spheres & $L/D = 2$

Flows were solved using the 2nd order UPWIND spatial discretization scheme (table 12).

L/D	Re	Grid	Cells Count	Convergence level	Mean y^+ wall	Lead Sphere		
						Mean y^+ wall	Drag Coefficient	Viscous Drag (%)
2	12 000	coarse	1 106 880	2,00E-12	0,86	1,29	0,393	9,3
2	12 000	medium	1 636 800	4,00E-10	0,88	1,29	0,394	9,3
2	12 000	fine	2 400 640	1,00E-08	0,88	1,29	0,395	9,3

Table 13 : 8 spheres & $L/D = 2$ & $Re = 12,000$; simulations' main results

The streamwise drag differs in C_d by less than 1%.

The results extracted from the 4th sphere's surface and from its wake along the x-axis are plotted Figure 31 (for the results along the entire domain see in Annex 3):

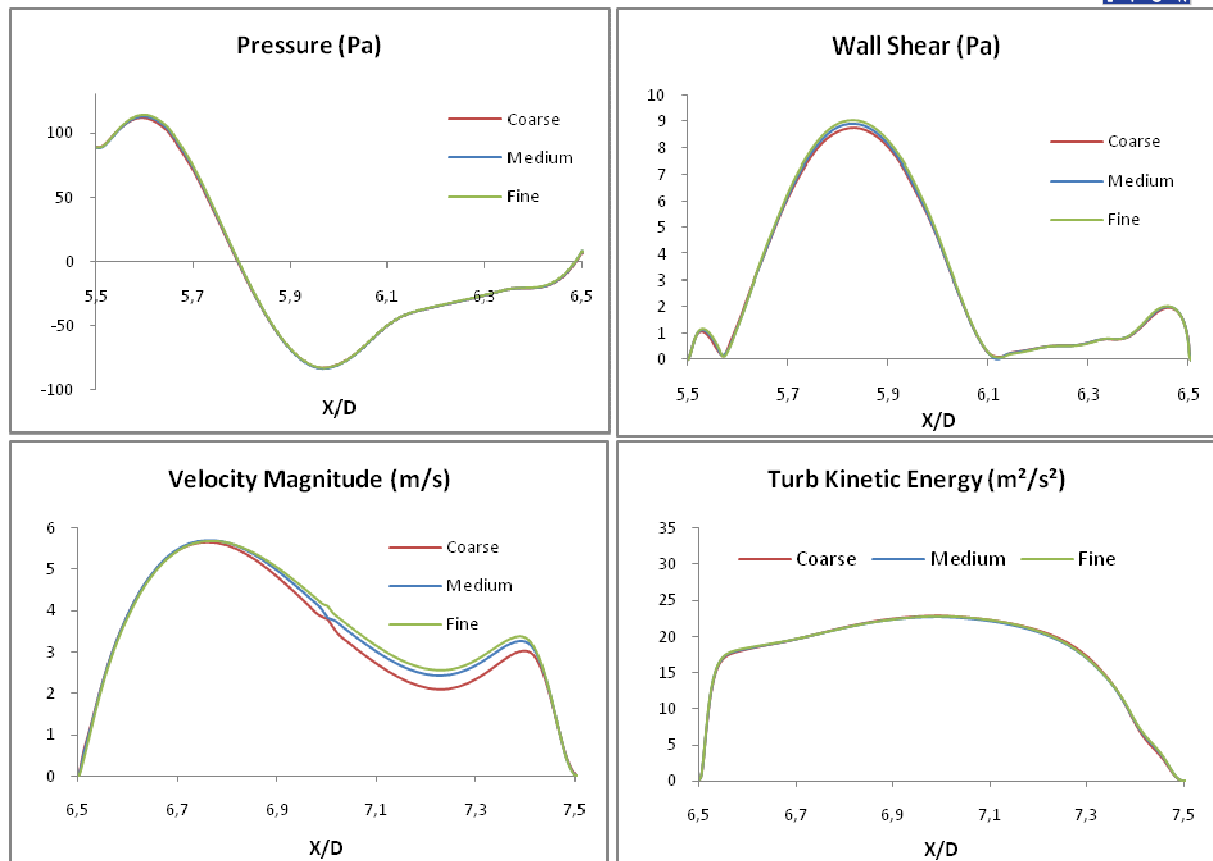


Figure 31 : 8 spheres & $L/D = 2$ & $Re = 12,000$; results values for grid independence

The difference between medium and fine is always inferior to 1% except for the velocity magnitude in the wake of the sphere. Here the difference stays between 2 % and 5 % on a distance of $0.5D$. Therefore one can consider that the fine grid yield grid independent enough results.

→ $L/D = 6$ & $Re = 12\,000$:

For this geometry two meshes were created (table 13)

L/D	Grid	Cells Count	Boundary Layer	
			First Row Size (mm)	Growth Factor
6	medium	1 690 401	0.020	1.1
6	fine	2 428 096	0.020	1.1

Table 14 : Meshes for 8 spheres & $L/D = 6$

Flows were solved using the 2nd order UPWIND spatial discretization scheme (table 14).

L/D	Re	Grid	Cells Count	Convergence level	Mean y+ wall	Lead Sphere		
						Mean y+ wall	Drag Coefficient	Viscous Drag (%)
6	12 000	medium	1 690 401	3,00E-09	1,06	1,35	0,463	8,9
6	12 000	fine	2 428 096	6,00E-08	1,09	1,35	0,465	8,8

Table 15 : 8 spheres & L/D = 6 & Re = 12,000; simulations' main results

The streamwise drag differs in Cd by less than 1%.

The results extracted from the 4th sphere's surface and from its wake along the x-axis are plotted Figure 32 (for the results along the entire domain see in Annex 3):

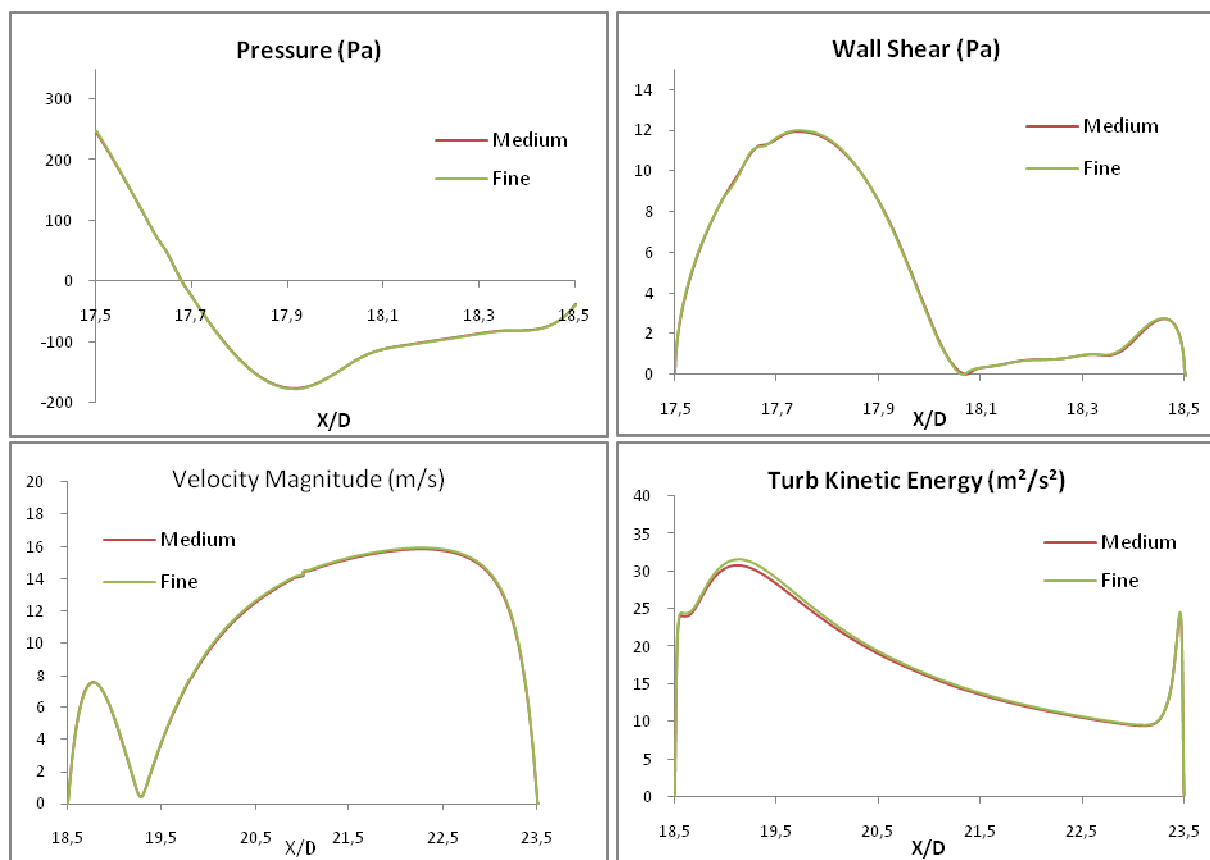


Figure 32 : 8 spheres & L/D = 6 & Re = 12,000; results values for grid independence

The difference between medium and fine is always inferior to 1% except for the turbulent kinetic energy in the near wake of the sphere. Here the difference goes up to 3 % only. Therefore one can consider that the fine grid yield grid independent enough results.

→ Last case and summary:

For the $L/D=1.5$ geometry only one mesh was created (table 15) using the parameters used for the $L/D=2$ fine mesh (with some adaptations):

L/D	Grid	Cells Count	Boundary Layer	
			First Row Size (mm)	Growth Factor
1.5	-	2 443 584	0.010	1.1

Table 16 : Mesh for 8 spheres & $L/D = 1.5$

The table 16 summarizes all the simulations made with 8 spheres:

L/D	Re	Grid	Cells Count	Convergence level	Mean y^+ wall	Lead Sphere		
						Mean y^+ wall	Drag Coefficient	Viscous Drag (%)
1.5	6 000	-	2 443 584	8,70E-08	0,63	0,80	0,449	12,0
1.5	8 300	-	2 443 584	5,00E-09	0,39	0,51	0,429	10,7
2	3 000	fine	2 400 640	1,40E-08	0,32	0,44	0,500	16,6
2	6 000	fine	2 400 640	8,70E-08	0,63	0,8	0,449	12,0
2	12 000	fine	2 400 640	1,00E-08	0,88	1,29	0,395	9,3
6	3 000	fine	2 428 096	1,50E-09	0,39	0,46	0,579	16,0
6	6 000	fine	2 428 096	2,80E-09	0,75	0,83	0,524	11,5
6	12 000	fine	2 428 096	6,00E-08	1,09	1,35	0,465	8,8

Table 17 : 8 spheres; simulations' main results summary

2.3 Results and discussions

All the simulations needed for particles tracking have been computed. Grid sensitivity was made in order to ensure that the results obtained are the best possible with this method.

In this chapter the results obtained with single spheres are first compared with experimental data. Then results with $Re = 3,000$ and $Re = 12,000$ are compared in order to see if the flow can really considered as Re independent (more particularly if the particles deposition results will be insensible to the Reynolds number).

2.3.1 Calculations verification

The prediction of the mean drag coefficient is above the range of the experimentally measured values. At $Re = 12\,000$ the predicted value is $C_d = 0.466$ compared to $C_d = 0.39 - 0.41$ in Achenbach's experiments [4]. This was expected as RANS usually results in over prediction of the drag.

This gap between Achenbach experiment results and the present simulation can also be illustrated by the Figure 33:

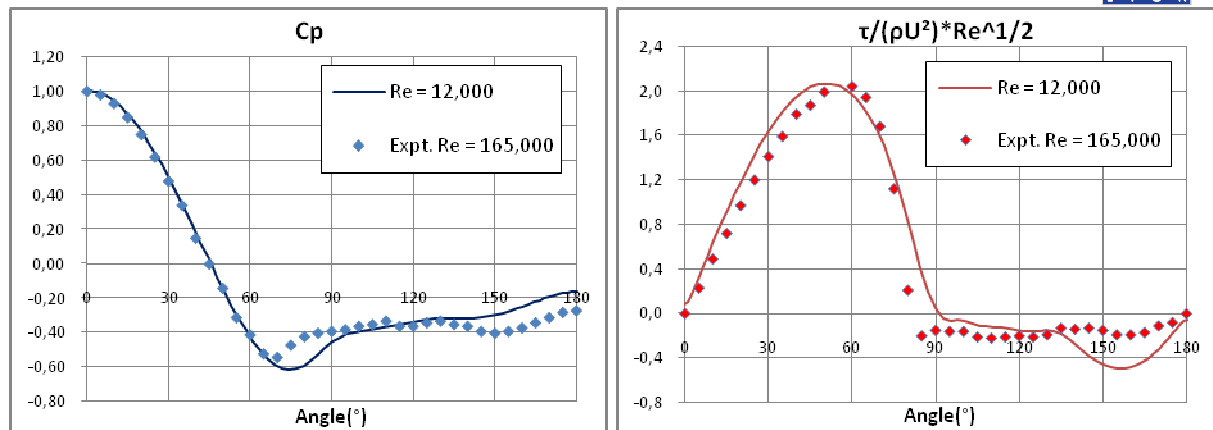


Figure 33 : Single sphere & Re = 12,000; comparison simulation/data

The two solutions are coherent. However the friction coefficient is slightly overestimated in the front part of the sphere. As particles deposition mainly occurs on this part it can have a bad effect on particles deposition results.

For the solution at $Re = 12\,000$, laminar boundary layer separation occurs at an angle of 94° that is higher than the value of 82.5° measured by Achenbach. This can influence the particles deposition on following spheres by modifying the extend of the wake.

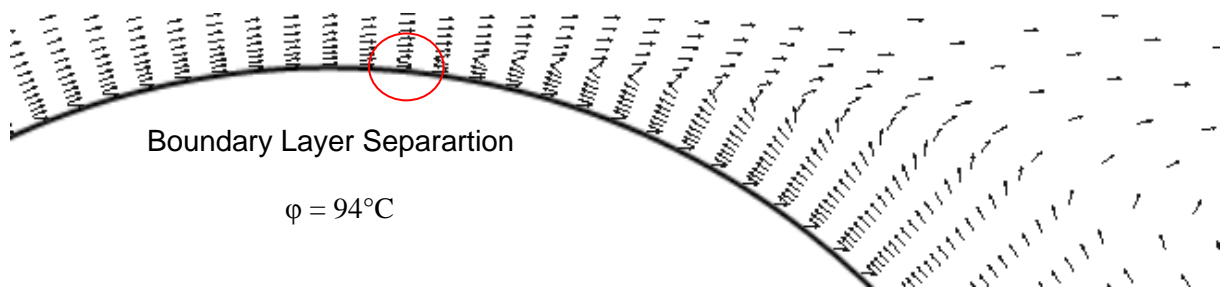


Figure 34 : Single sphere & Re = 12,000; boundary layer detachment point

One can also take a closer look to the recirculation area. Figure 35a shows the results obtained by Jang [5] at $Re = 11,000$ while Figure 36b shows the recirculation area we obtained at $Re = 12,000$.

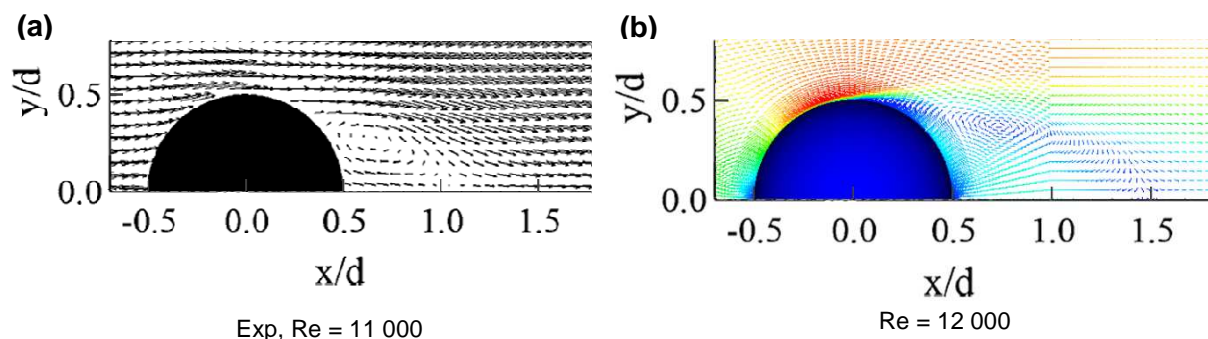


Figure 35 : Single sphere; recirculation area, comparison simulation/data

Experimental measurements show a recirculation area extended only on a distance of $0.5D$ while the numerical solution gives one twice as long. The steady RANS computation

overestimates clearly the near wake size. This can lead to important errors on particles deposition if the following sphere is less than $1.5D$ far from the lead sphere. Anyway this difference shows clearly that the wake is not accurately resolved and will probably lead to divergence on particles deposition on following spheres.

In conclusion, on the one hand the flow close to the sphere seems reasonably well resolved so one can expect that particles deposition on single sphere to be correctly estimated. On the other hand the resolution of the wake is not as good so one can expect that particles deposition on following spheres to be imprecise.

2.3.2 Reynolds number influence

In their experiments Hähner [9] and Waldenmair [10] choose Reynolds Number between 10^3 and 10^5 . In this range the flow field around a sphere concerning the form and the extension of the wake can be considered uniform to a great extent. For this reason one can be tempted to think that particles deposition can also be considered as independent of the Reynolds Number.

The following results show indeed that in our simulations the dimensionless wall friction (Figure 36) and the recirculation area extension (Figure 37) are quite uniform between $Re = 3,000$ and $Re = 12,000$. Then particles deposition on single sphere is probably virtually independent of Re .

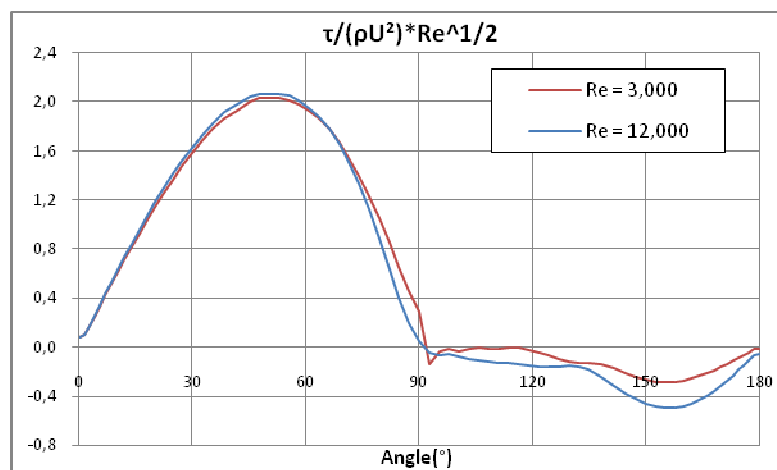


Figure 36 : Single sphere; wall friction coefficient, Re influence

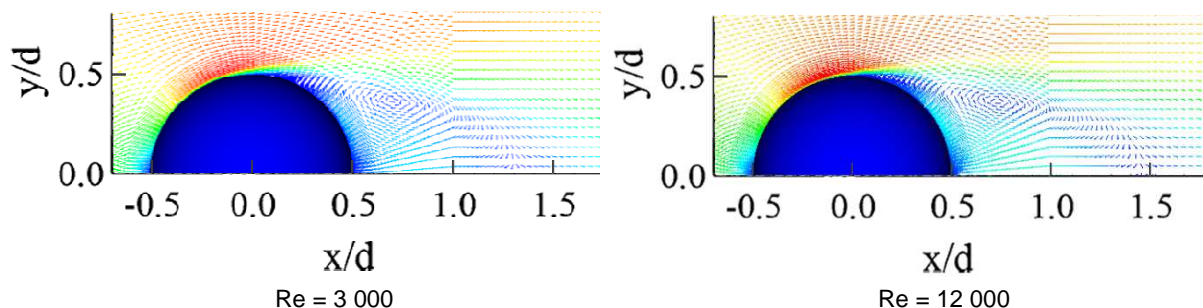


Figure 37 : Single sphere; recirculation area, Re influence

For $Re = 3,000$ recirculation extends until around $1.3D$; for $Re = 12,000$ recirculation extends until around $1.5D$.

However as regard particle deposition on following spheres of an array this assumption is not so evident. First of all the flow seen by the following spheres is disturbed by the lead one so one can't regard the Reynolds Number as being the same for every sphere and Re can possibly go down below 10^4 . Moreover the lead sphere creates a shielding effect that reduces the importance of particles inertial impaction mechanism on the following spheres and makes turbulence-enhanced deposition more decisive. Yet the turbulence intensity of the flow reaching a sphere will mostly depend on the previous sphere's wake. The Figure 38 shows that turbulence intensity in the wake can be distributed quite differently depending on the Reynolds number:

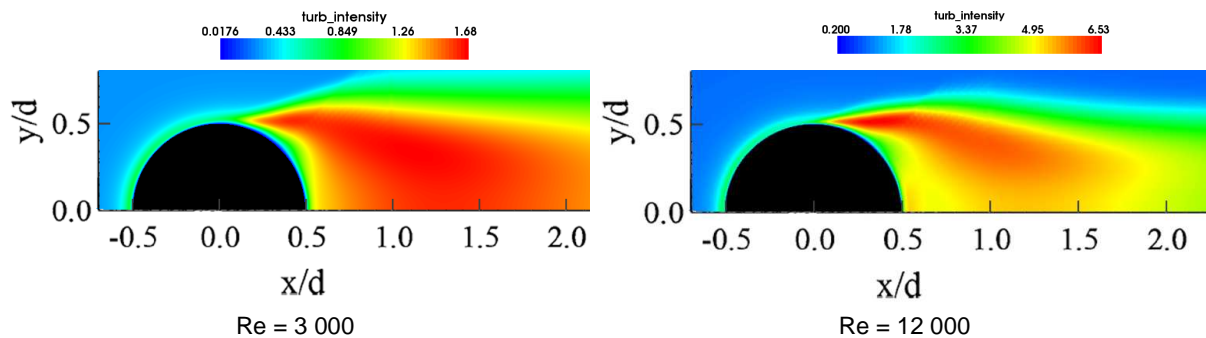


Figure 38 : Single sphere; turbulent intensity, Re influence

In conclusion, even if one can assume that particle deposition on single sphere is Re -independent into the chosen range, this affirmation is not so evident for particle deposition on linear array of spheres.



3 Particles Tracking

Twelve different flows have been solved using steady CFD-RANS calculation with RSM turbulent model. Even if the solutions found show some differences they are reasonably good. The next step of the Lagrangian particles tracking method is to inject particles at the entrance of the domain, follow their path and measure particles deposition on each collector. This part presents the methods used for injections and deposition calculations, then details the results obtained as regard particles deposition first on single spheres then on arrays of spheres

3.1 Particle injection and deposition calculation methods

Injection and deposition calculation methods are highly dependent to the particles tracking method used and the set up's geometry. This chapter describes and justifies the ones used in this investigation.

3.1.1 Collection efficiency

All the experiments made by Hähner [9] and Waldenmainer [10] were conducted using liquid particles of DES (Di-II-ethyl-hexyl-sebacate) in a velocity range such as no bounce off occur. Then in the present simulations the boundary conditions of the collectors have been set such as every particle touching the wall is trapped. Impaction and deposition are equivalent.

Each collector is characterized by its collection efficiency which is the ratio of deposit particles mass m_d to that m_o carried into the projection area of the collector:

$$\eta = \frac{m_d}{m_o}$$

Furthermore all the particles injected have the same density $\rho_p = 913 \text{ kg/m}^3$ so the collection efficiency is also the ratio of deposit particles number N_d to that N_o carried into the projection area of the collector:

$$\eta = \frac{N_d}{N_o}$$

In the strict sense, the definition of the collection efficiency is limited to singles spheres and not valid for arrays of spheres. Due to the fact that an experimental determination of the particles concentration in front of each sphere of an array is very difficult both Hähner [9] and Waldenmainer [10] measured the aerosol concentration only in front of the first sphere. The calculation of the collection efficiency for each sphere is then based on the particles concentration in the projection area of the first sphere of an array.

Then, in our simulations, the collection efficiency of the sphere i of an array is:

$$\eta_i = \frac{N_i}{N_o}$$

With:

N_i = number of particles deposited on the sphere i

A list of the main transport mechanisms has been made in the first part of this report. However, only liquid particles in gas flow ($\rho_p \gg \rho_f$) with $0.1 \text{ } \mu\text{m} < d_p < 20 \text{ } \mu\text{m}$ are considered here. Moreover the temperature is considered uniform all over the fluid domain. Then, the only significant force acting on the particles is taken to be drag and our investigation focused only on inertial deposition (inertial impaction and turbulence-enhanced deposition). Deposition on collectors depends then mainly on the particles Stokes number:

$$Stk = \frac{\rho_p d_p^2 u_0}{9\mu D}$$

In order to compare particles deposition measurements with different Stokes numbers one has to define a relative collection efficiency:

$$\eta_{ri} = \frac{\eta_i}{\eta_1}$$

Then the first sphere has always a normalized collection efficiency of 1.

One last variable has been defined. It characterizes the repartition of the particle deposition on a sphere. It is defined as followed:

$$p_i = \frac{\text{particles deposition repartition for the sphere } i \text{ of an array}}{\text{number of particles deposited in the back of the sphere } i} = \frac{N_i}{N_i}$$

Because the boundary layer separation happen around $\varphi = 90^\circ$ in the studied flow fields, p_i gives the proportion of particles which deposit because entrained inside the recirculation area of the sphere.

While comparing experimental data and computation results two numbers are used: the gap and the error. They are defined as follows:

$$Gap = data - numeric$$

$$Error = \frac{|data - numeric|}{data}$$

These two numbers are percentage but while the gap is an absolute percentage the error is a relative one.

3.1.2 Injection

One of the major issues while making Lagrangian particles tracking coupled with a Random Walk model is the injection method.

A. Generalities

In our geometries the injection has to be made in the inlet of the pipe and the inlet concentration of particles has to be uniform. However injecting particles all over the inlet will be a waste of computing time as the particles far from the center have a negligible chance to deposit on the spheres. The injection area must be set as only a fraction of the total inlet surface.

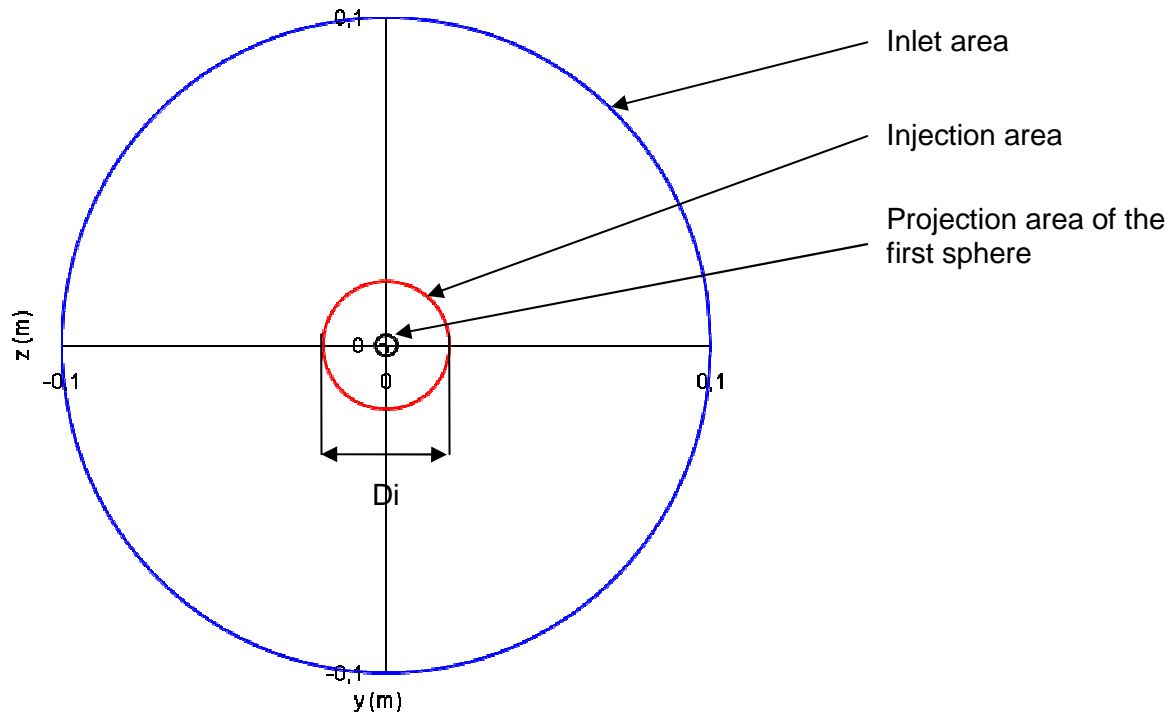


Figure 39 : Inlet area subdivision

An injector can be defined by its diameter (D_i), its number of particles, and the diameter of the particles (d_p). However the number of particles and the diameter are codependent so we define:

→ Injector ratio :

$$r = \frac{D_i}{D}$$

→ Central particles number :

$$N_p = \text{number of particles in the projection area of the first sphere}$$

Then an injector is defined by its ratio r , its central number of particles N_p , and the particles diameter d_p . While the choice of d_p is fixed by the experimental case to be reproduced, r and N_p are ours to choose.

B. Injector size

Making the injection area smaller than the inlet area reduces considerably the particles tracking computing time. However one has to make sure that he is not missing any particles deposition by making the injector too small.

In order to determine the minimum injector size, particle tracking computations have been performed using injectors with particles only on the circumference of the injection area. The injector ratio has been set with various values and if no particles deposited on the collectors the injector is big enough. However two different investigations have been conducted: one for single sphere cases and one for array of spheres cases.

→ Injector size for single spheres:

Particles tracking computations were made with the lowest and the highest Stokes number for $Re = 3,000$ and $Re = 12,000$. The table 17 gives the number of particles deposited for 10,000 particles injected:

Nb of Particles Traped for 10,000 injected			
Re	Stk	Injector Ratio r	
		1	2
3000	0,01	4	0
3000	10	1970	0
12000	0,01	4	0
12000	10	1211	0

Table 18 : Injector size determination for single sphere cases

An injector with a ratio of 2 is enough for all the single spheres cases. These results show that using a injector the size of the sphere will lead to huge underestimation of the collection efficiency. Thus, **all the particles tracking computations in single sphere geometries have been performed using injectors with $r=2$.**

→ Injector size for arrays of spheres:

To be sure the injector found is good for all the cases ($L/D = 1.5, 2$ and 6), these computations were made using the biggest spacing. This case needs the biggest injector because it has the longest collector extension so the highest chance that particles far from the first sphere diffuse enough to reach the last one.

Particles tracking computations were made with the lowest and the highest Stokes number for each Reynolds Number. The table 18 gives the number of particles deposited for 10,000 particles injected:

Nb of Particles Traped for 10,000 injected						
Re	Stk	Injector Ratio r				
		3	4	5	6	7
3000	0,03	24	3	0		
3000	2,3	335	44	2	0	
6000	0,03	2	1	0		
6000	2,3	117	6	1	0	
12000	0,03	2	1	0		
12000	2,3	121	18	3	<1	0

Table 19: Injector size determination for 8 spheres cases

A ratio of 6 is clearly enough. However if one chooses a ratio of 5, the collection efficiency of the 8th sphere (and only the 8th one) can be underestimated for high Stokes numbers but not for low Stokes numbers. In the worst case ($Re = 12,000$ and $Stk = 2.3$) the collection efficiency can be underestimated 0.4 % (and of less than 0.2 % for Re below 6,000). Moreover for these values of Stokes numbers the collection efficiency of the last spheres of an array is above 10%. Then an injector with a ration of 5 is enough for all the 8 spheres cases. Thus, **all the particles tracking computations in 8 spheres geometries have been performed using injectors with $r=5$.**

C. Particles distribution and number of particles :

In order to obtain a uniform particles distribution we choose to distribute them randomly all over the injection area (cf. FORTAN program in Annex 4). However the distribution can be considered as uniform only if the number of particle is big enough. In order to determine the minimum number of particle needed three injector have been created with 100, 1000 and 10000 particles (Figure 40).

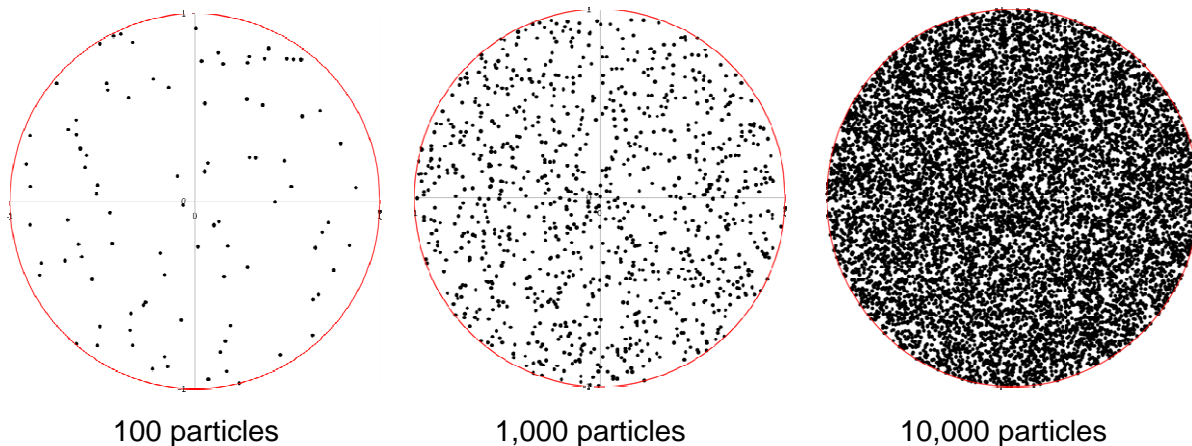


Figure 40 : Particle density repartition for various numbers of particles

If the distribution is uniform, by dividing the surface by X one should also divide the number of particles by X. For the three injectors one Xth on the surface has been extracted, X ranging from 2 to 10, and the number of particles in the extracted surface have been determined. The table 19 shows the relative error between the surface ratio (surface of the injector/surface of the extracted area) and the number of particles ratio (total number of particles/number of particles in the extracted area).

		Surface ratio								
		2	3	4	5	6	7	8	9	10
Part. Number	100	18,8%	43,9%	48,4%	35,7%	43,9%	35,7%	31,9%	31,9%	18,8%
	1000	0,4%	6,9%	7,6%	4,6%	3,7%	0,5%	6,9%	5,6%	3,8%
	10000	0,1%	0,4%	0,8%	0,9%	0,7%	0,7%	0,1%	0,0%	0,6%

Table 20 : Relative error in particles distribution for various injectors

From 10,000 particles the relative error is always below 1 % so the particles distribution can be considered as uniform. Then, in all the injectors the **central number of particles** N_p has to be superior to 10,000.

However, even if $N_p = 10,000$ is enough to have a uniform inlet particles distribution it may be insufficient as regard particles deposition. The tracking model being stochastic 10,000 injections may not be enough to obtain good averaged results. Unfortunately the number of particles really needed cannot be determined easily as it depends on the case. That is why **all the particles tracking have been performed using injectors with $N_p = 20,000$** and in some cases a second computation has been made using $N_p = 50,000$ or 100,000. Then the comparison of the results tells us if the first injector was sufficient or not.

3.1.3 Particles tracking and reduced geometry

Except for the first one (single sphere with $Re=5000$) all the simulations have been made using only one quarter of the geometry. On the one hand, when solving the flow it is easy to obtain an equivalent solution. One just has to impose symmetric boundary conditions over the symmetry planes. In the other hand, when making particle tracking one has to check first the particles behavior when crossing the symmetry planes.

In Fluent 6.3 a particle crossing a face set with symmetric boundary condition leaves the domain without reflecting. This way no particle tracking was possible with a reduced geometry. Fortunately in Fluent 12 it is no longer the case. When particles cross a face set with symmetric boundary condition there are reflected. This way, doing particles tracking in the reduced geometry or in the total geometry are equivalent.

As regard the injection, N_p is still the number of particles in the projected area of the first sphere except that now the projected area is a quarter of a disc and not a disc.

The only flow available both with the total and reduced geometry is: one single sphere with $Re=5,000$. Deposition efficiency calculations have been made for these two cases. The Figure 41 shows collection efficiency as a function of the particles Stokes number:

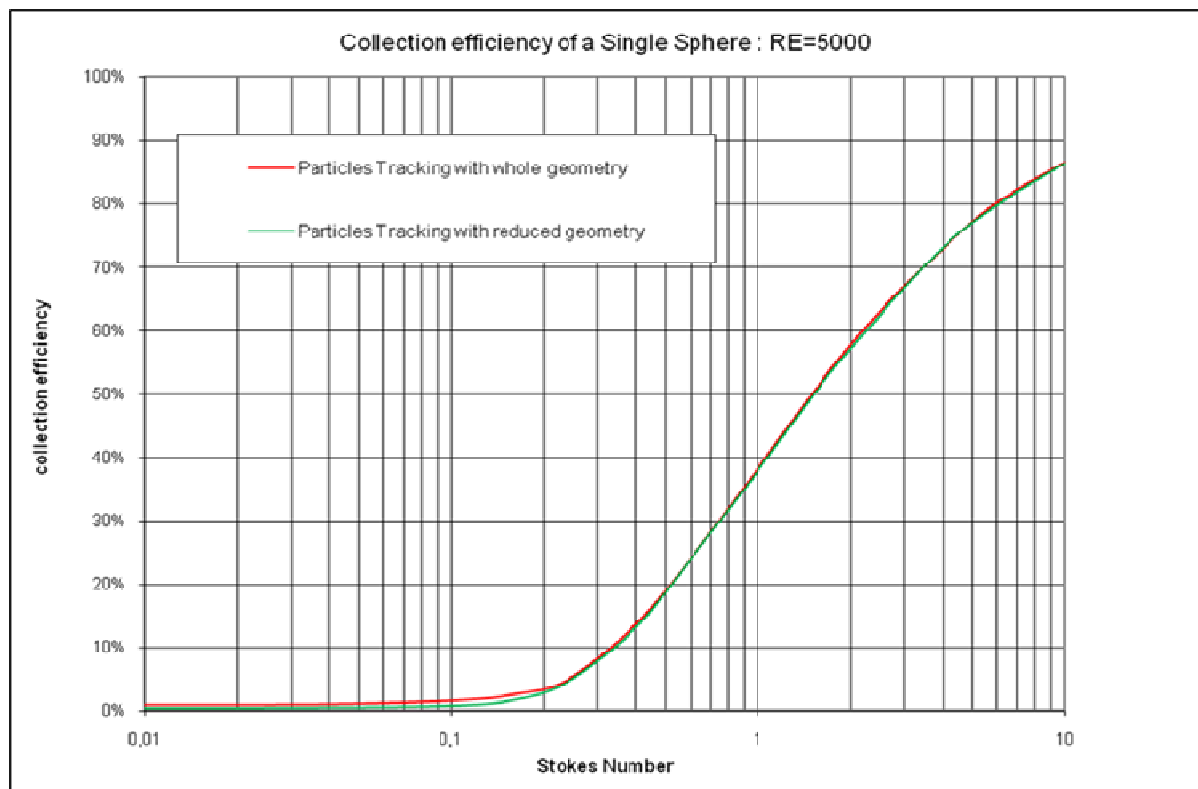


Figure 41 : Collection efficiency of single sphere; comparison whole vs. reduced geometry

The gap between the two curves is always inferior to 1 %. However for low Stokes numbers the collection efficiency is around 1% so even if the gap is small it corresponds to an error of 100 % or so. These results show that for Stokes number higher than 0.3 both geometries are equivalent for particles tracking. As regard particles tracking with very low Stokes number values the equivalence is not so evident and it depends on the scattering of the experimental results used to benchmark the model. If the scattering of the data is higher than the gap then the results can be considered as equivalent.

3.2 Particles deposition on single spheres

Both injection and deposition calculations methods have been selected. Then particles tracking can be computed. This chapter first summarizes the important experimental data concerning particles deposition on single spheres, then gives the results obtain with the CRW tracking model, finally it compared the two set of results.

3.2.1 Experimental data

Hähner [9] and Waldenmainer [10] have conducted collection efficiency experiments using single sphere as collectors with various diameter ($D = 3.2 \text{ mm}$, 6.5 mm and 9 mm). Various Reynolds numbers were used, ranging from 1,000 to 17,000. The particles Stokes numbers range from 0.03 to 4.5. The Figure 42 summarizes these results.

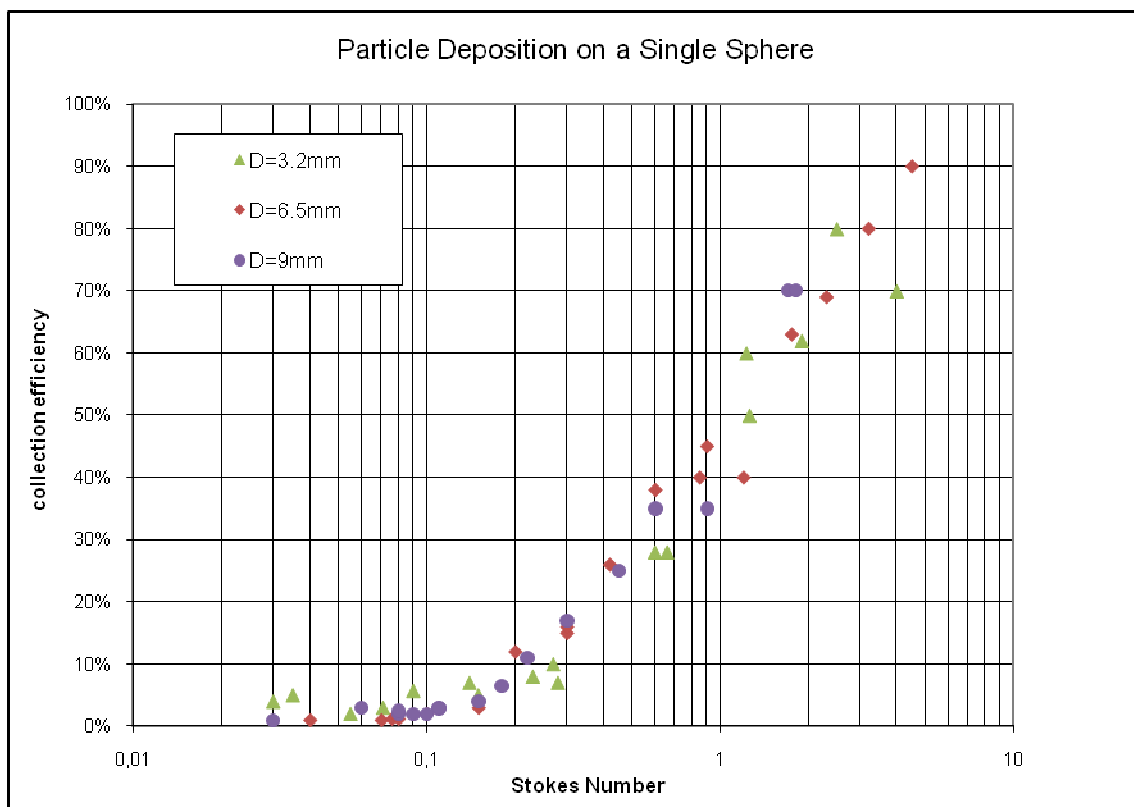


Figure 42 : Collection efficiency of single sphere; experimental data

One can note that the scattering of the data is quite important, particularly for low Stokes numbers (< 0.1) where the collection efficiencies are between 1 and 5 % (more than 500% of relative scattering). Then, as regard particles tracking computation, the reduced geometry can be considered equivalent to the whole one all over the Stokes number range.

3.2.2 Tracking results

As explained later in this report, three different flow fields past a single sphere have been computed at $Re = 3,000$, $Re = 5,000$ and $Re = 12,000$. The sphere diameter is always $D = 6.5 \text{ mm}$.

Then particles tracking have been conducted using the following injector's parameters: $r = 2$ and $N_p = 20,000$ (some computations have been also made with $N_p = 50,000$ but they yield the same results). The particles diameters d_p have been set so the particles Stokes number ranges from 0.01 to 10 (thirteen values).

Plotted on Figure 43 are the results for the collection efficiency calculations in the three regimes:

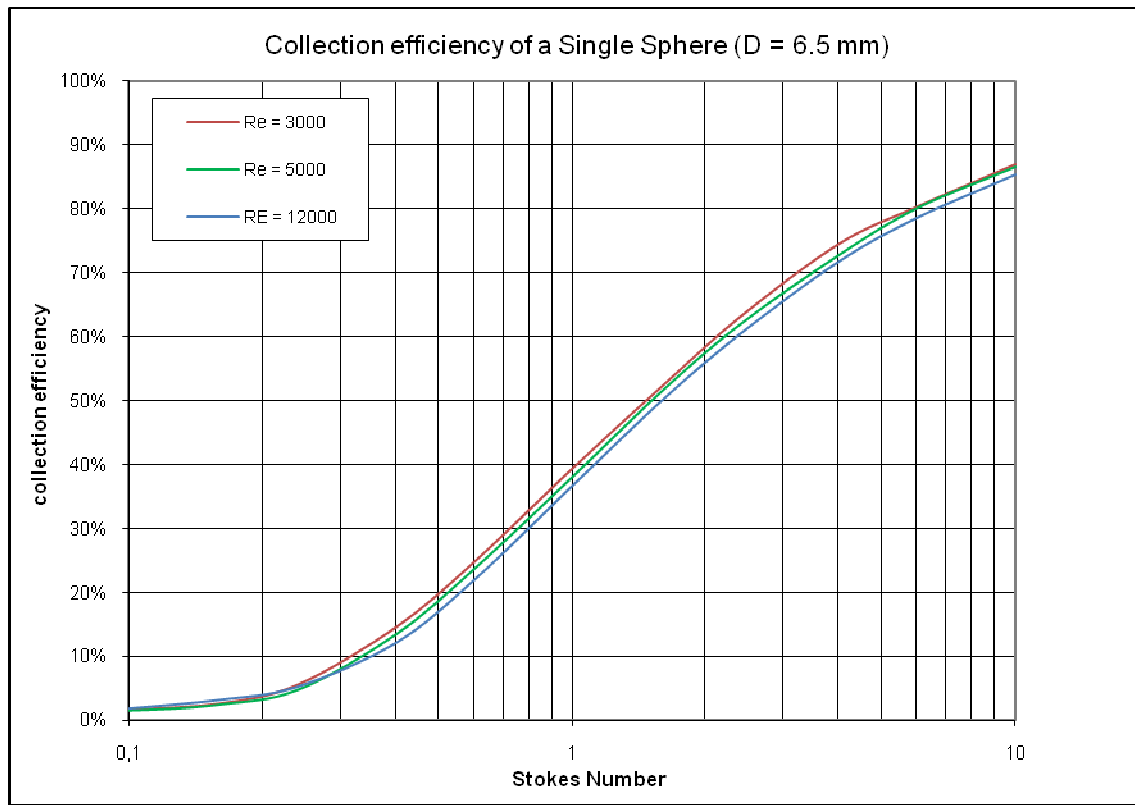


Figure 43 : Collection efficiency of single sphere; particles tracking results

Comment: Collection efficiency for particles below $Stk = 0.1$ is almost uniform around 1%.

As expected the Reynolds number has little impact on the particles deposition. However for $Stk > 0.3$ collection efficiency is around 2.5% higher with $Re = 3,000$ than with $Re = 12,000$. For $Stk < 0.2$ this gap is negligible (less than 0.5%). Then considering that the results are Re independent is maybe overrated. Moreover in the Reynolds number range used here the flow is uniform to a great extent, and then one can expect that with even smaller Reynolds number (outside the uniform flow range) its impact on collection efficiency will be more important.

3.2.3 Model benchmarking

The numerical geometry has a 6.5 mm diameter sphere only so only the data obtained with $D = 6.5$ mm have been used to benchmark the model. Then the experimental Reynolds number ranges from 3,000 to 12,000 only and the Stokes number from 0.03 to 4.5.

Superposed on the Figure 44 are the results from experiments, the results obtains with the CRW model at $Re = 5,000$ and numerical results obtained by Hahn [12] at $Re = 500$:

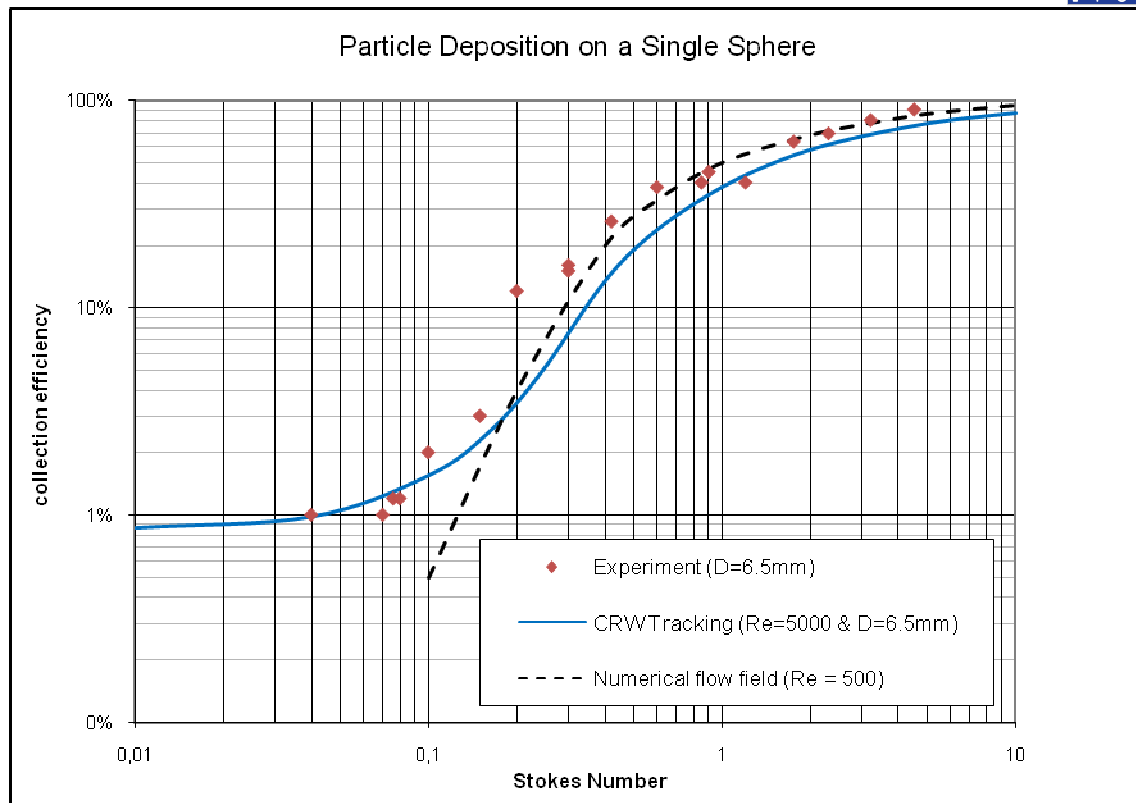


Figure 44 : Collection efficiency of single sphere; comparison data vs. simulation results

One can say about these results:

- Experimental data and CRW computation results show the same tendency all over the Stokes number range (even at very low Stokes numbers (< 0.2) where the numerical results by Hahn [12] fail to predict any particles deposition).
- For $Stk < 0.2$ the agreement between CRW result and data is good. Moreover for very low Stokes numbers the turbulence-enhanced particles deposition is preponderant so the CRW tracking model seems to accurately take this mechanism into account.
- For $Stk > 0.2$ the CRW model underestimates the particles deposition. The computed collection efficiency is between 15 and 6 % lower than the experimental data (except for $Stk = 1.2$ where it is above experimental data). The mean value of the gap is 8.8%.
- The numerical results by Hahn [12] seem coherent with the experimental data. However they have been obtained with $Re = 500$ which is below the experimental range and outside the range where the flow is uniform. In fact these numerical results are more coherent with our results because they are above them than with the experimental data from which they should be superior. Then maybe the coherence between the Hahn results and the data is just a coincidence.

In conclusion, despite a tendency to underestimate particles deposition at high Stokes number the model yields good results for particles deposition on single spheres. However, for single spheres particles deposition is mainly due to inertial impaction (except maybe for low Stk) and turbulence-enhanced deposition is secondary. Then the improvement brought by the CRW model cannot really be seen here (except for low Stk).

3.3 Particles deposition on arrays of spheres

This chapter first summarizes the important experimental data concerning particles deposition on arrays of spheres, then gives the results obtain with the CRW tracking model, finally it compared the two set of results.

3.3.1 Experimental data

In order to benchmark particle tracking computations one needs to have access to experimental data. The best benchmarking is when experimental and numerical set ups are exactly the same (same geometries and same boundary conditions). When this exact equivalence is not possible, at least the dimensionless numbers which characterize the phenomenon studied must be equal (here the particles Stokes number and the sphere Reynolds number).

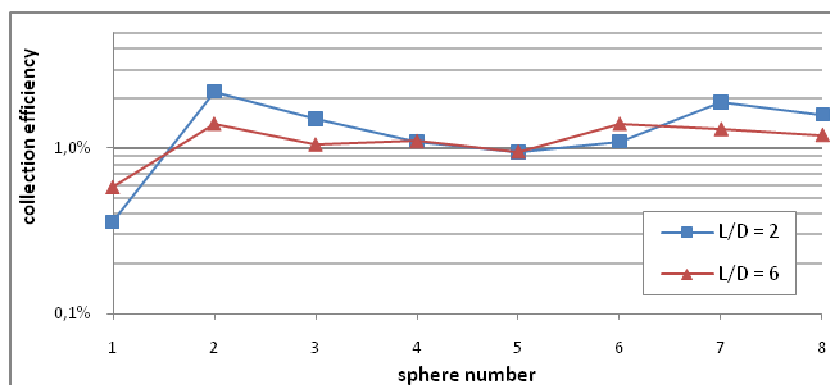
The experimental data used here have been obtained by Hähner [9] and Waldenmainer [10] and even if they both treated a lot of configurations only few results are available. Moreover they conducted experiments in various geometries while the numerical results have been obtained with constant geometry so, in some case, only the dimensionless numbers Stk and Re match. The table 20 summarizes all the configurations with data available and specifies the ones where experimental and numerical geometries are different (signaled out by a circle in the table below).

Stk	L/D		
	1.5	2	6
0.03		X	X
0.04	O		
0.3		X	X
0.44	O		
1.2	X	X	X
2.3	X		

Table 21 : Experimental data available

For each spacing data are available at low (0.03 or 0.04), medium (0.3 or 0.44) and high (1.2) particles Stokes number.

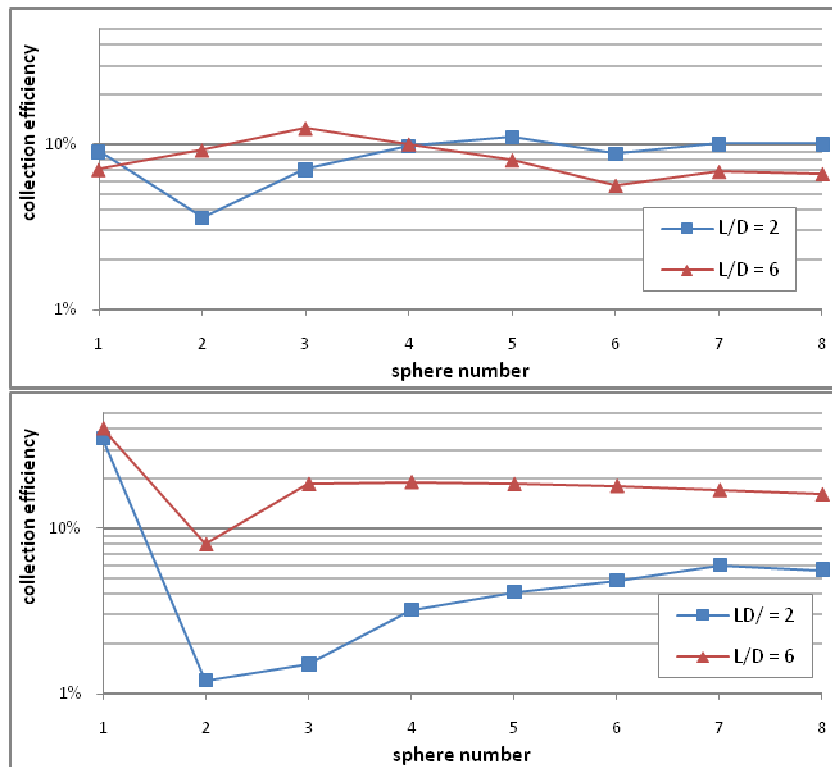
The results by Hähner [9] ($L/D = 2$ and $L/D = 6$) show the impact of sphere spacing on particles deposition for three different particles Stokes number (0.03, 0.3 and 1.2).



(a) Parameters:

$D = 6.5 \text{ mm}$
 $d_p = 1.4 \text{ }\mu\text{m}$
 $u_0 = 14 \text{ m/s}$

$Re = 6,000$
 $Stk = 0.03$



(b) Parameters:

$D = 3.2$ mm
 $d_p = 3.5$ μ m
 $u_0 = 14$ m/s

$Re = 3,000$
 $Stk = 0.3$

(c) Parameters:

$D = 6.5$ mm
 $d_p = 10$ μ m
 $u_0 = 14$ m/s

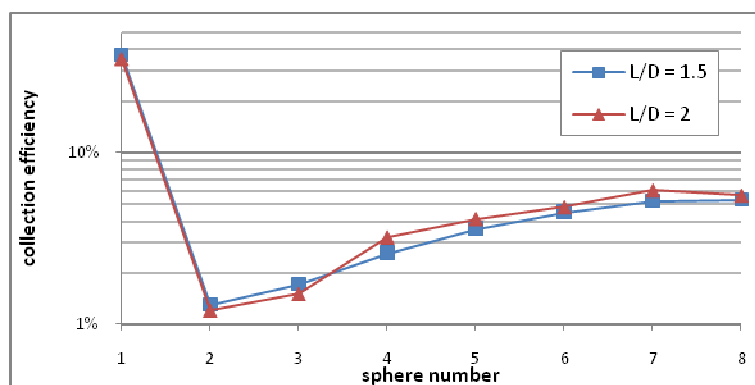
$Re = 6,000$
 $Stk = 1.2$

Figure 45 : Collection efficiency on linear arrays; data from Hähner

As expected collection efficiency of the first sphere goes down as the Stokes number decrease. As regard particles deposition on the following spheres two configurations can be observed:

- The leading sphere creates a shielding effect and particle deposition on second spheres is lower. This configuration can be observed for high Stk values (Figure 45 c.) and medium Stk values with close spheres (Figure 45 b.).
- The leading sphere creates a reverse shielding effect and particle deposition on the second is higher. This configuration can be observed for low Stk values (Figure 45 a.) and medium Stk values with spheres far apart (Figure 45 b.).

The results by Waldenmainer [10] give us the collection efficiencies at $L/D = 1.5$ for two Stk values (0.03 and 1.2). Moreover, for $Stk = 1.2$ the geometry is identical to the one used by Hähner [9], then the two results can be compared (Figure 46). Waldenmainer [10] results also give us the relative collection efficiencies for four different Stokes numbers (Figure 47).

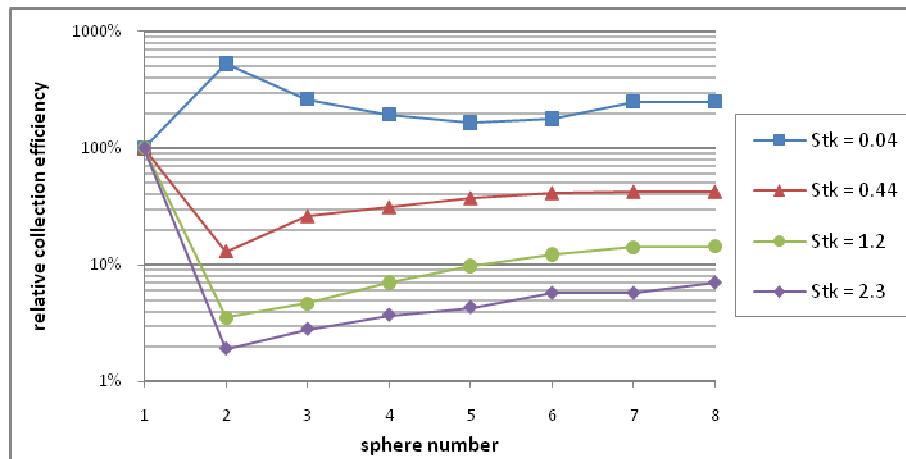


Parameters:

$D = 6.5$ mm
 $d_p = 10$ μ m
 $u_0 = 14$ m/s

$Re = 6,000$
 $Stk = 1.2$

Figure 46 : collection efficiency on linear arrays; data from Waldenmainer 1



Parameters:

 $Re = 6,000^*$
 $L/D = 1.5$

(*except for
 $Stk = 0.44$
where
 $Re = 8,300$)

Figure 47 : collection efficiency on linear arrays; data from Waldenmainer 2

First, one can note that the results at $Stk = 1.2$ for $L/D = 1.5$ are quite close to those obtain by Hähner [9] for $L/D=2$ (Figure 46). Otherwise, the shielding effect of the first sphere decreases while the particles Stokes number decreases (Figure 47) and gets inverted between $Stk = 0.4$ and $Stk = 0.04$.

In conclusion one can note that all these results present the same construction. For each case collection efficiency goes through three phases as the sphere number increase:

- Deposition on Lead sphere, characterized by the collection efficiency of the 1st sphere: η_1 .
- Shielded zone: starts at the 2nd sphere and ends around the middle of an array. It is the zone where the shielding or reverse shielding effect is the most visible. This zone can be characterized by the relative collection efficiency of the second sphere: η_{r2}
- Stabilization zone: starts around the middle of an array and ends with it. In this zone the collection efficiency shows a tendency to get constant. This zone can be characterized by the mean value of the 5th to 7th spheres' collection efficiencies: $\frac{\eta_{r5} + \eta_{r6} + \eta_{r7}}{3}$ (from now these three spheres are called **the tail** of an array).

The experimental data of particles deposition on leading spheres can be compared to those obtain with single spheres (Figure 48).

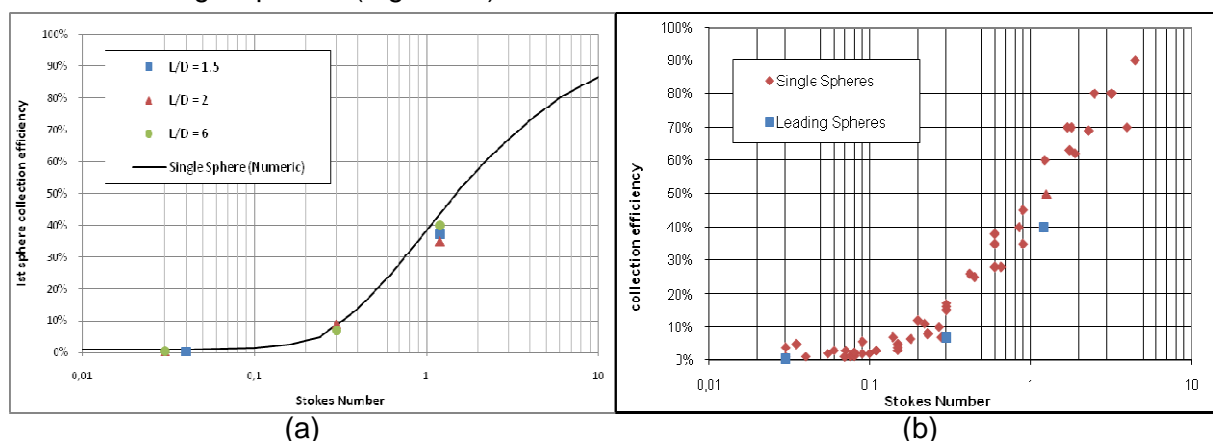


Figure 48 : Comparison collection efficiency leading spheres vs. single spheres

First of all one can note that while experimental data of collection efficiency of single spheres are above the numerical curve (Figure 44) those for leading spheres are below the curve (Figure 48 a.). Then the gap between single sphere data and leading sphere data is huge for high Stk (Figure 48 b.). One can wonder what's the cause of such difference even with $L/D = 6$ where the second sphere can hardly interact with the first one. Moreover this comparison gives us a idea of the scatter of experimental data.

3.3.2 Tracking results

Every experimental case from which data are available has been numerically reproduced. Moreover particles tracking have also been computed with more Stokes numbers and more flow fields. The table 21 summarizes all the particles tracking that have been computed.

Re	Stk	L/D		
		1.5	2	6
3000	0.04			
	0.3		X	X
	0.44			
	0.9			
	1.2			
	2.3			
6000	0.03		X	X
	0.04	X		
	0.3			
	0.44			
	0.9			
	1.2	X	X	X
	2.3	X		
8300	0.44	X		
	0.9	X		
12000	0.04			
	0.3			
	0.44			
	0.9			
	1.2			
	2.3			

Table 22 : Particles tracking computations summary (X = data available)

White squares correspond to computations made. Moreover, all the particles tracking at $Re=6,000$ have been conducted using both the CRW and the DRW tracking model.

A first check of the results' coherence can be done by comparing the particles deposition on leadings spheres with particles deposition on single spheres (Figure 49).

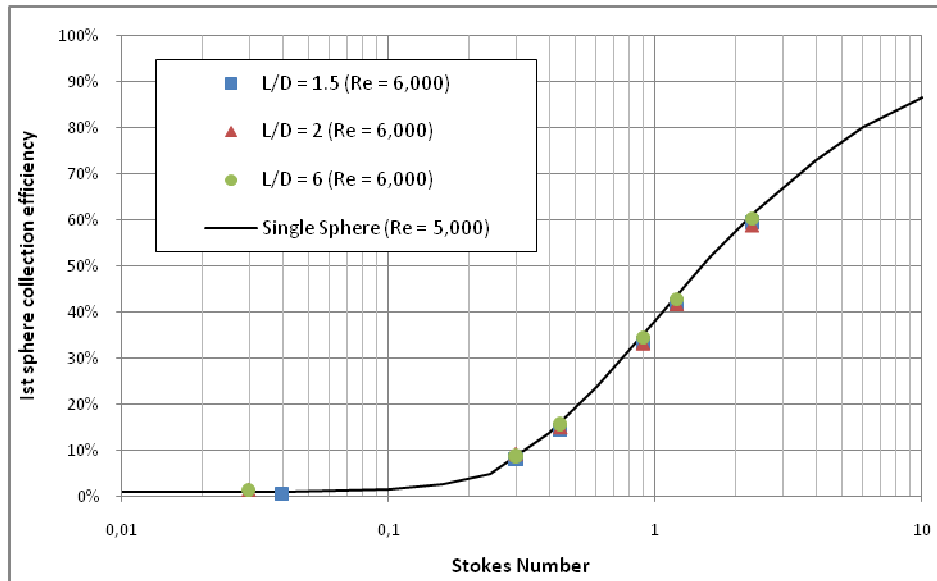
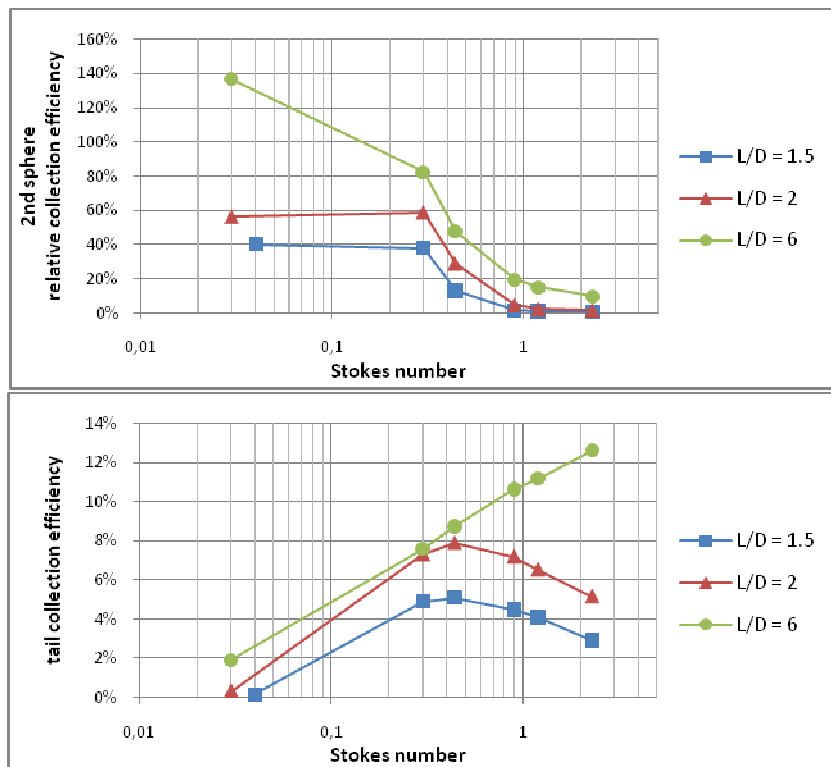


Figure 49 : Comparison collection efficiency leading spheres vs. single spheres

The results are indeed coherent: particles deposition on the first sphere is independent to sphere spacing and of the same order of magnitude than particles deposition on single spheres (they are indeed slightly lower because computed at different Reynolds number).

In order to visualize the behavior of the model two parameters have been used: **the relative collection efficiency of the second sphere** to characterize the **shielding effect**, and **the collection efficiency of the tail** to characterize the **stabilization zone**.

First the influence of the spacing (Figure 50) on collection efficiencies has been investigated.



(a) Parameters:

$D = 6.5 \text{ mm}$
 $u_0 = 14 \text{ m/s}$

$Re = 6,000$

(b) Parameters:

$D = 6.5 \text{ mm}$
 $u_0 = 14 \text{ m/s}$

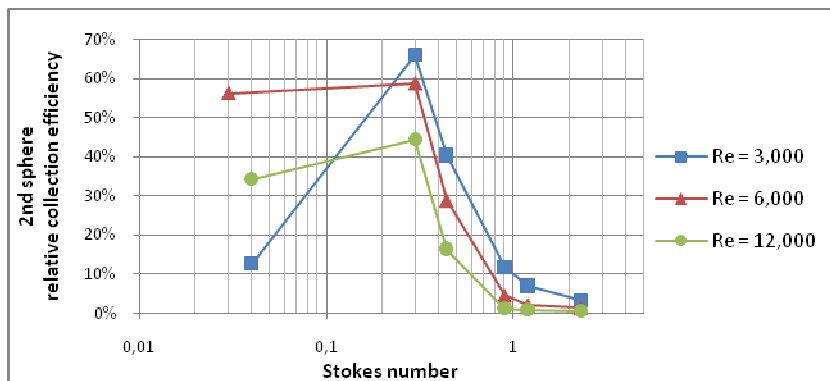
$Re = 6,000$

Figure 50 : Collection efficiency of arrays; simulation results, spacing influence

As regard the shielding effect (Figure 50 a.) for all spacing it increases as Stk increase: for $L/D = 2$ at $Stk = 0.3$ the 2nd sphere collection efficiency is about 60% of the first one while it goes down to below 1% at $Stk = 1.2$. Moreover for $L/D = 1.5$ or 2 the shielding effect is uniform between $Stk = 0.03$ and 0.3 and between $Stk = 1.2$ and 2.3. Otherwise the shielding effect decreases as the spacing increases. This was expected as the influence of the first sphere on the second decreases as the spacing increases. Finally, the only configuration with a reverse shielding effect is for $L/D = 6$ at very low Stk (0.03).

As regard the collection efficiency of the tail (Figure 50 b.) it shows quite different behaviors depending on the spacing. For $L/D = 1.5$ or 2 it increases as Stk increases until around $Stk = 0.5$ then starts decreasing. For $L/D = 6$ it always increases as Stk increases. Otherwise collection efficiency of the tail globally increases as the spheres spacing increases.

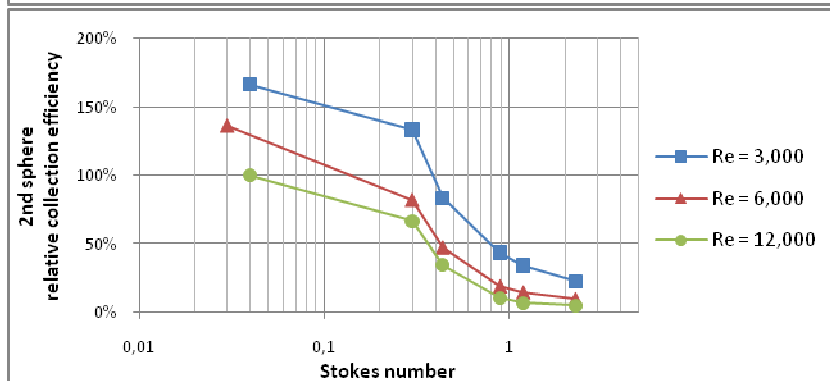
Then the influence of the Reynolds number on collection efficiencies (Figure 51) has been investigated. Indeed, collection efficiency on single spheres has previously been proven as nearly Re independent but collection efficiencies on arrays of spheres is maybe not so.



(a) Parameters:

$D = 6.5 \text{ mm}$

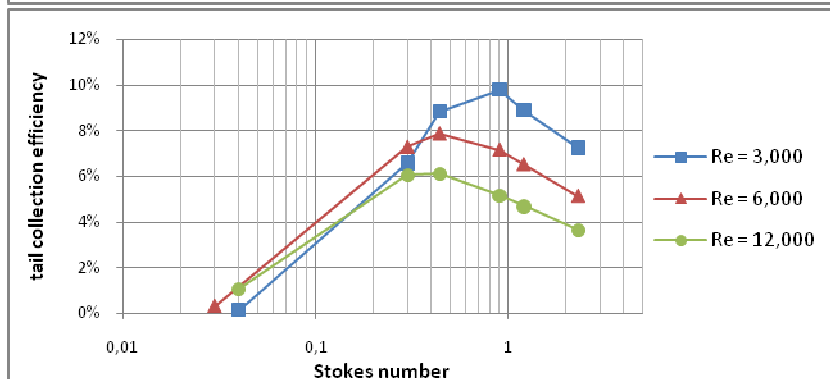
$L/D = 2$



(b) Parameters:

$D = 6.5 \text{ mm}$

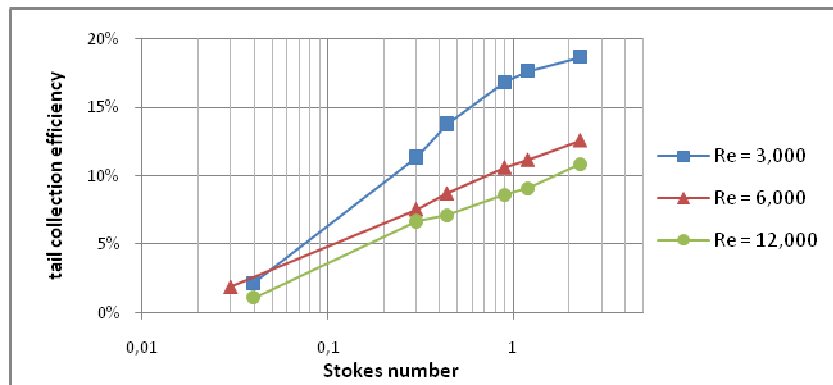
$L/D = 6$



(c) Parameters:

$D = 6.5 \text{ mm}$

$L/D = 2$



(d) Parameters:

$$D = 6.5 \text{ mm}$$

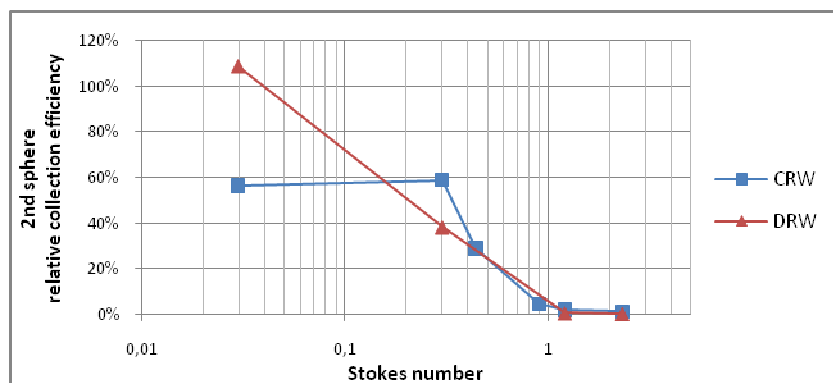
$$L/D = 6$$

Figure 51: Collection efficiency of arrays; simulation results, Re influence

As expected the shielding effect (Figure 51 a. and b.) increase as Re increase (the higher the Reynolds number the more the influence of the first sphere on the second). However one can note that for $Re = 3,000$ the results at $Stk = 0.03$ seem too low, maybe due to model's limitations. Moreover the gap between $Re = 3,000$ and $Re = 6,000$ is larger than between $Re = 6,000$ and $Re = 12,000$ probably because at $Re = 3,000$ more spheres fall below the range where the flow is uniform.

The same thing for the collection efficiency of the tail (Figure 51 c. and d.): it decreases as the Re increases in the same way that for the single sphere; except that this time results can hardly be considered as nearly Re-independent. For example between $Re = 6,000$ and $Re = 12,000$ the collection efficiency gap is globally of 2% which correspond to a decrease of more than 30 %. Moreover at $Re = 3,000$ the results are also qualitatively different particularly at low Stk , probably for the same cause than previously.

At last, difference between the CRW tracking model and the DRW tracking model (Figure 52) has been investigated.



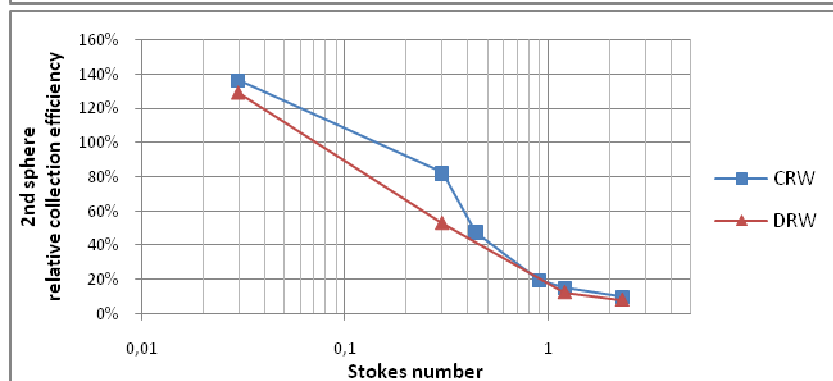
(a) Parameters:

$$D = 6.5 \text{ mm}$$

$$u_0 = 14 \text{ m/s}$$

$$Re = 6,000$$

$$L/D = 2$$



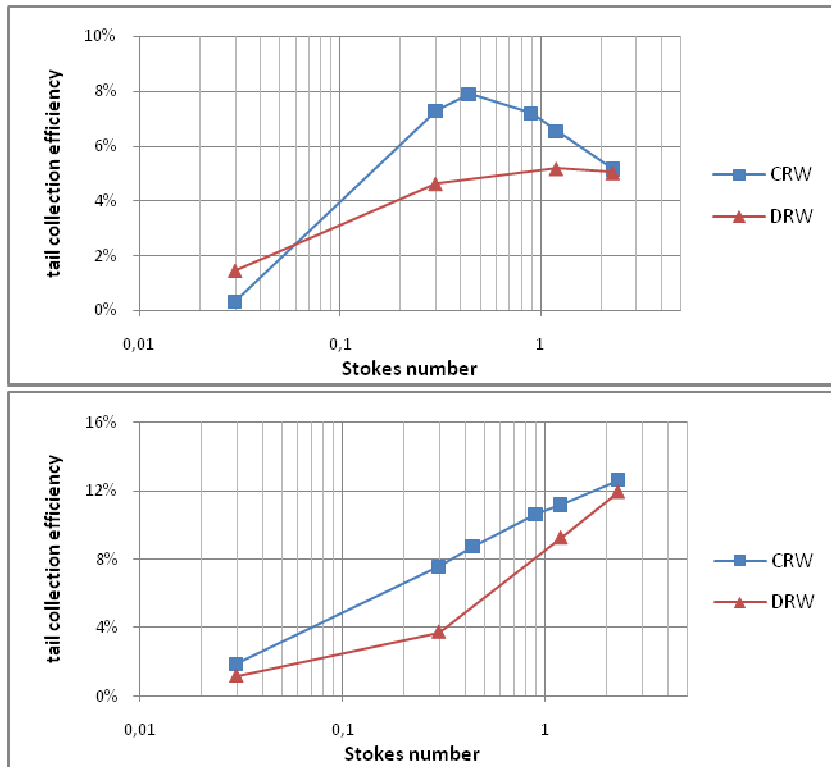
(b) Parameters:

$$D = 6.5 \text{ mm}$$

$$u_0 = 14 \text{ m/s}$$

$$Re = 6,000$$

$$L/D = 6$$



(c) Parameters:

$$D = 6.5 \text{ mm}$$

$$u_0 = 14 \text{ m/s}$$

$$Re = 6,000$$

$$L/D = 2$$

(d) Parameters:

$$D = 6.5 \text{ mm}$$

$$u_0 = 14 \text{ m/s}$$

$$Re = 6,000$$

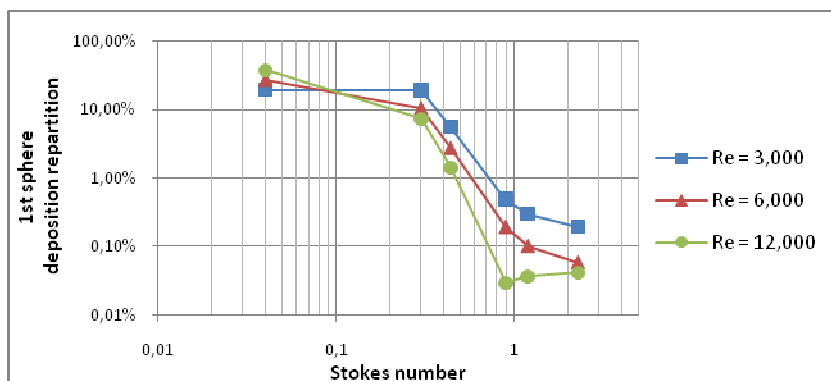
$$L/D = 6$$

Figure 52: Collection efficiency of arrays; simulation results, tracking model influence

As regard the shielding effect (Figure 52 a. and b.) the results are close at $Stk > 0.5$. For $Stk < 0.5$ results are both quantitatively and qualitatively different: while the CRW model fails to capture any reverse shielding effect at $Stk = 0.03$ the DRW model seems to succeed.

As regard the collection efficiency of the tail (Figure 52 c. and d.) the DRW results are globally lower than the CRW ones and this gap tend to decrease as the Stk increase. This was expected as the DRW model tends to underestimated turbulence-enhanced particles deposition and the turbulence impact on deposition decrease as the Stk increase.

One last result has been investigated: the particles deposition repartition p_i between the front and the back of the spheres (Figure 53).



(a) Parameters:

$$D = 6.5 \text{ mm}$$

$$L/D = 2$$

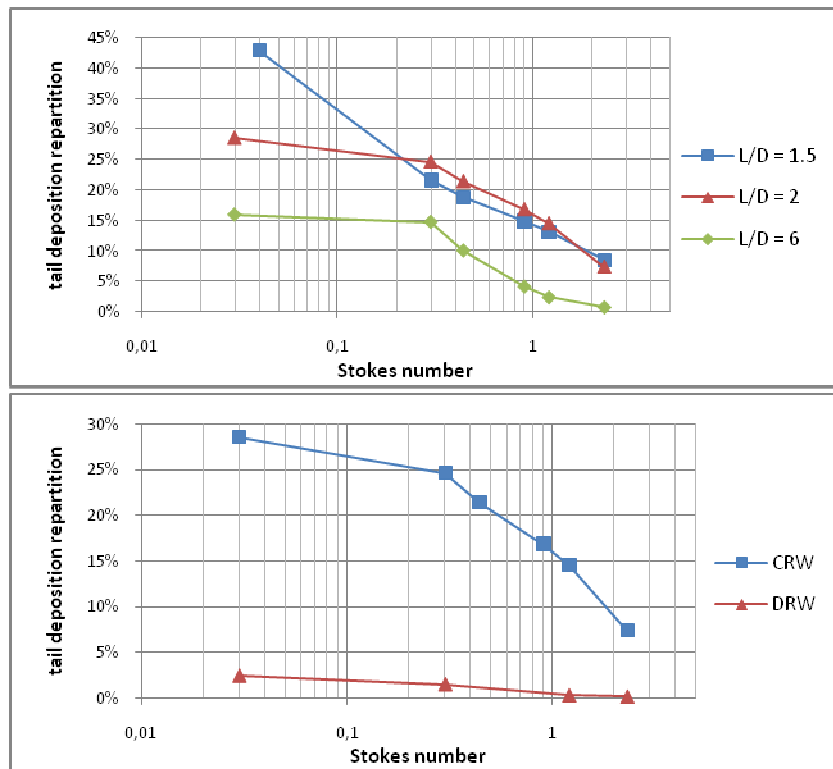


Figure 53 : Particles deposition repartition; simulation results

As regard the first sphere (Figure 53 c.) at $Stk > 0.5$ the number of particles deposited on the back of the sphere is negligible (less than 1% of the deposition). However at $Stk < 0.3$ this number is quite important (between 10 and 50 % of the deposition). As expected the higher the Reynolds number the smaller the particles deposit on the back of the sphere.

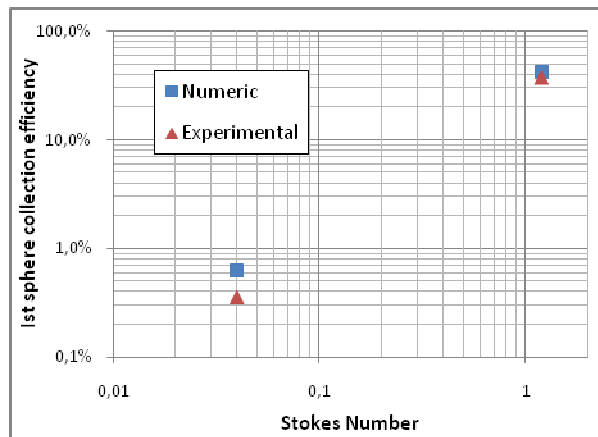
As regard the tail (Figure 53 b.) for $L/D=1.5$ or 2 the number of particles deposited on the back is never really negligible (always $>5\%$). For $L/D=6$ it falls below 5% for $Stk > 0.8$. As expected the higher the spacing between spheres the lesser the particles deposit on the back of the tail's spheres.

Finally as regard the particles tracking model (Figure 53 c.) the DRW model totally fails to predict any particles deposition on the back of the spheres. This can explain that the two models yield quite different results for medium Stk values (Figure 52 c. and d.) where the deposition on the back of the spheres is the more important.

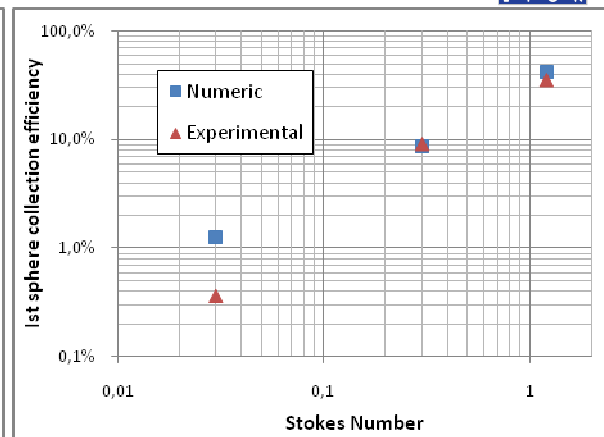
3.3.3 Model benchmarking

The final step (and most important) of our investigation is the comparison between experimental data and numeric results. This comparison shows the efficiency and the limitations of the method: where it can be considered as yielding globally good results, where the results are only quantitatively good and where they are neither qualitatively nor quantitatively acceptable.

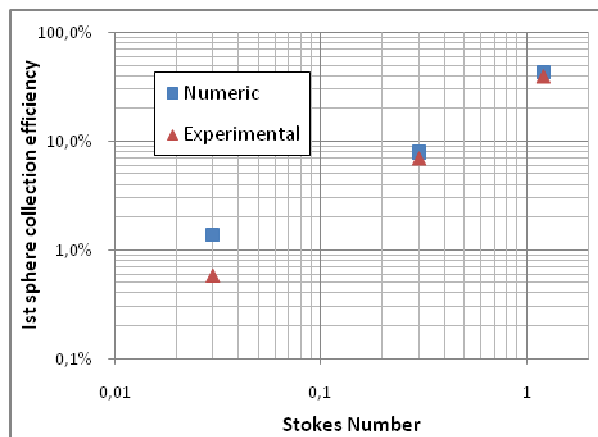
The first comparison concerns collections efficiency of the first spheres (Figure 54).



(a)



(b)



(c)

(a) : $L/D = 1.5$

(b) : $L/D = 2$

(c) : $L/D = 6$

Figure 54 : Collection efficiency of leading spheres, comparison simulation results vs. data

The table 22 summarizes the difference between numeric results and experimental data for leading spheres.

			Sphere spacing L/D		
			1.5	2	6
Stk value	Low (0.03/0.04)	Gap	-0.27%	-0.90%	-0.80%
		Error	76%	250%	138%
	Medium (0.3)	Gap		-0.33%	-1%
		Error		3.6%	13%
	High (1.2)	Gap	-4.7%	-6.7%	-2.6%
		Error	13%	19%	6.6%

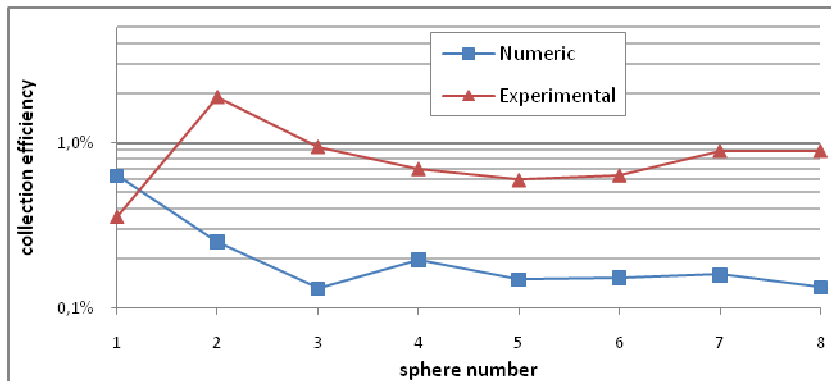
Table 23 : Collection efficiency of leading spheres, gaps and errors

For low Stokes numbers even if the gap is small the error is huge. For medium and high Stokes numbers the error is relatively small. One can also note that this time the numerical results are higher than the data while for the single spheres it was the opposite.

The results obtain on the rest of the arrays are presented below. The results are organized by sphere spacing. Each experimental data available is directly compared with its corresponding numerical results. When the two results have been obtained using the same geometry both dimensional and dimensionless parameters are specified in the right hand

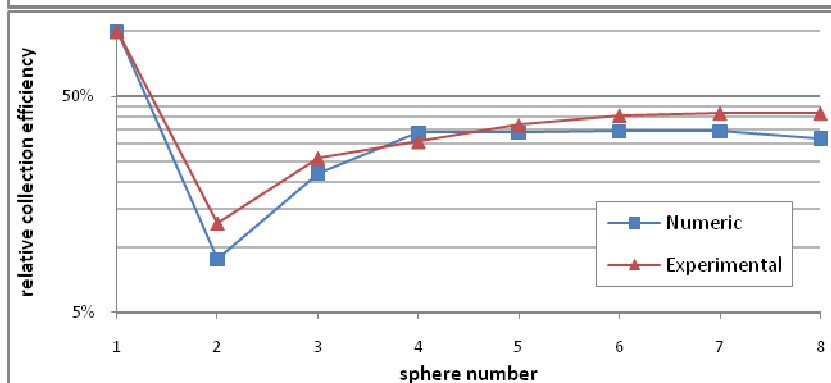
side of the figure. In the others cases only the dimensionless parameters are specified.

For $L/D = 1.5$ (Figure 55) the results are globally quite good except for those at very low Stokes number ($Stk = 0.04$):



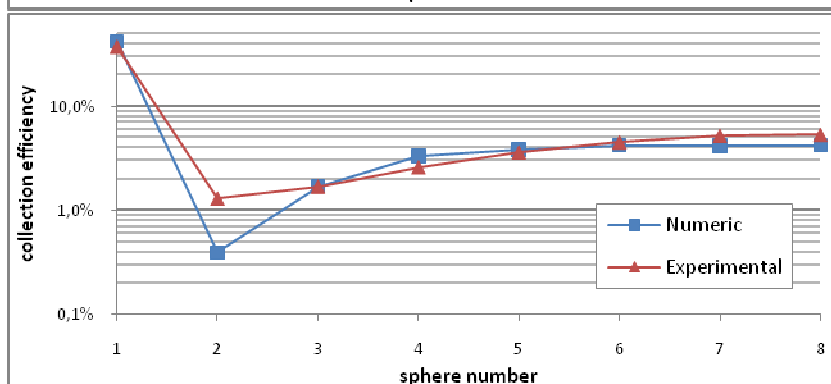
(a) Parameters:

$Re = 6,000$
 $Stk = 0.04$
 $L/D = 1.5$



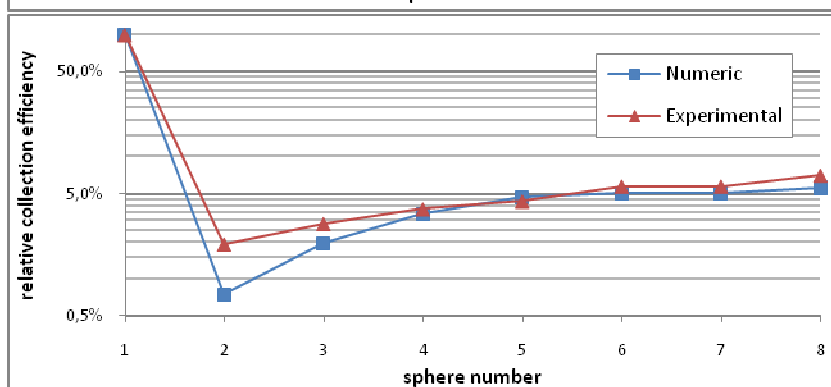
(b) Parameters:

$Re = 8,300$
 $Stk = 0.44$
 $L/D = 1.5$



(c) Parameters:

$D = 6.5 \text{ mm}$
 $d_p = 10 \text{ μm}$
 $u_0 = 14 \text{ m/s}$
 $Re = 6,000$
 $Stk = 1.2$
 $L/D = 1.5$



(d) Parameters:

$D = 6.5 \text{ mm}$
 $d_p = 14 \text{ μm}$
 $u_0 = 14 \text{ m/s}$
 $Re = 6,000$
 $Stk = 2.3$
 $L/D = 1.5$

Figure 55 : Collection efficiencies with $L/D = 1.5$, comparison simulation results vs. data

- At $Stk = 0.04$ (Figure 55 a.) the **gap** in collection efficiency of the tail is about **0.6%** which correspond to an **error of 78%**. As regard the **2nd sphere** the numerical simulation fails to capture the reverse shielding effect and the numerical results are **1.7% lower** which correspond to an **error of 87%**.
- At $Stk = 0.44$ (Figure 55 b.) the **gap** in relative collection efficiency of the tail is about **6%** which correspond to an **error of 14%**. As regard the **2nd sphere** the numerical results are **4% lower** which correspond to an **error of 32%**.
- At $Stk = 1.2$ (Figure 55 c.) the **gap** in collection efficiency of the tail is about **0.4%** which correspond to an **error of 8%**. As regard the **2nd sphere** the numerical results are **0.9% lower** which correspond to an **error of 70%**.
- At $Stk = 2.3$ (Figure 55 d.) the **gap** in relative collection efficiency of the tail is about **0.3%** which correspond to an **error of 6.5%**. As regard the **2nd sphere** the numerical results are **1.2 % lower** which correspond to an **error of 60%**.

The Figure 56 summarizes these results.

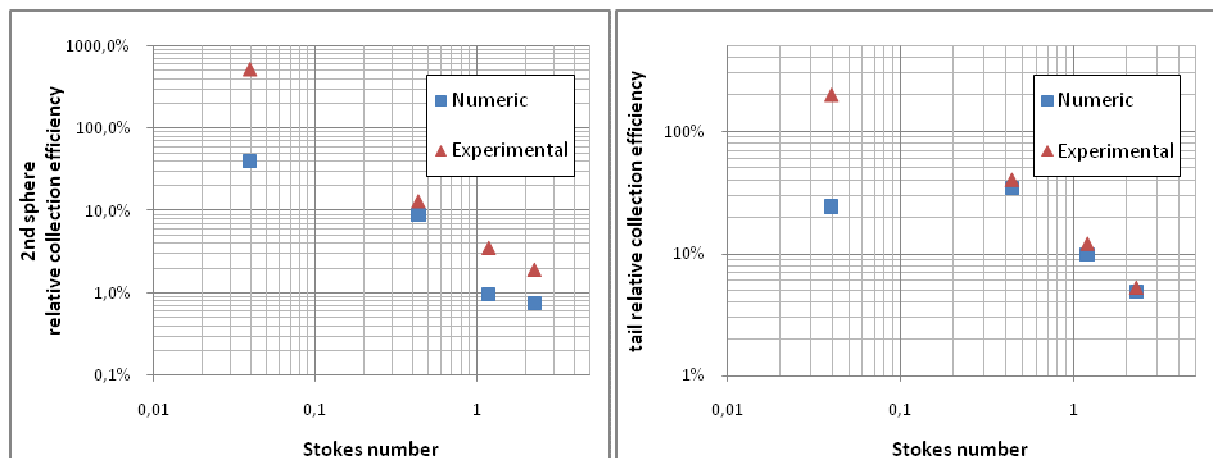


Figure 56 : Results with $L/D = 1.5$, model benchmarking

First one has to note that at $Stk = 0.44$ and $Stk = 2.3$ only the relative deposition efficiencies are available, and gaps and errors with the real deposition efficiencies are probably smaller. Moreover for $Stk = 0.44$ the two geometries are not identical.

As regard particles deposition on the second sphere the numerical model always underestimates it. This seems logical as RANS simulations tend to underestimate turbulence intensity and in the shielded zone turbulence-enhanced deposition dominates over inertial impaction. Moreover it has been shows previously in this report that the extend of the near wake was overestimated. Maybe this is the cause for the errors made on the second spheres.

For $L/D = 2$ (Figure 57) the results are still globally satisfactory except again for those at very low Stokes number ($Stk = 0.03$):

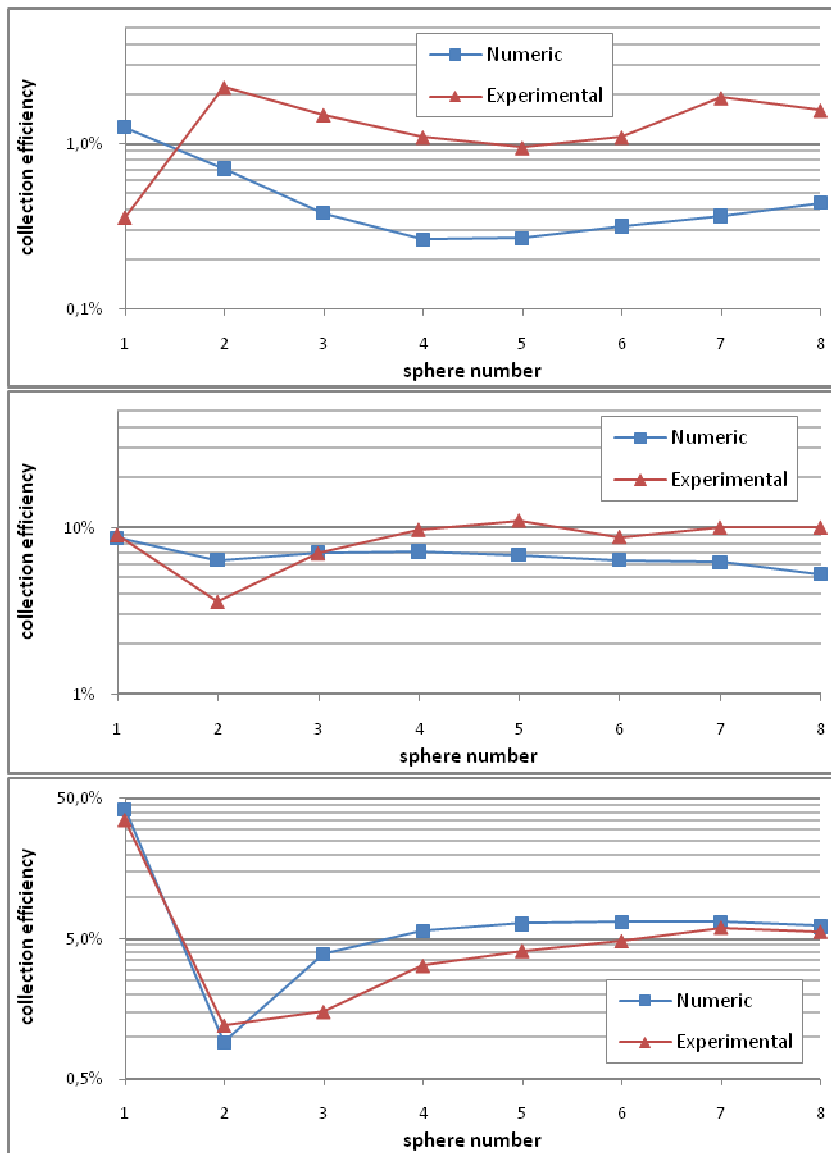


Figure 57: Collection efficiencies with $L/D = 2$, comparison simulation results vs. data

- At $Stk = 0.03$ (Figure 57 a.) the **gap** in collection efficiency of the tail is about **1%** which correspond to an **error of 76%**. As regard the **2nd sphere** the numerical simulation fails to capture the reverse shielding effect and the numerical results are **1.5% lower** which correspond to an **error of 68%**.
- At $Stk = 0.3$ (Figure 57 b.) the **gap** in collection efficiency of the tail is about **3.5%** which correspond to an **error of 35%**. As regard the **2nd sphere** the numerical results are **2.8% higher** which correspond to an **error of 77%**.
- At $Stk = 1.2$ (Figure 57 c.) the **gap** in collection efficiency of the tail is about **-1.6%** which correspond to an **error of 32%**. As regard the **2nd sphere** the numerical results are **0.3% lower** which correspond to an **error of 23%**.

The Figure 58 summarizes these results.

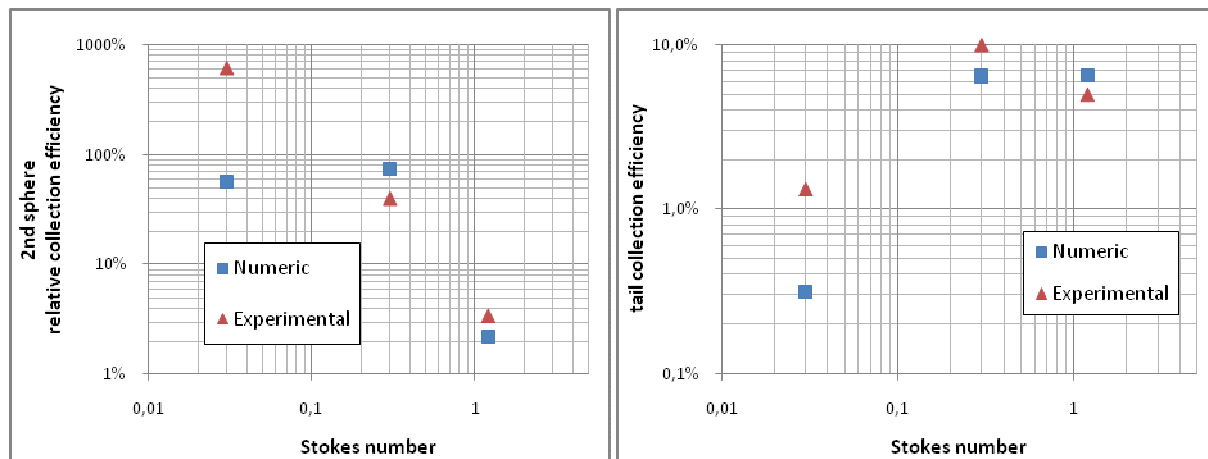


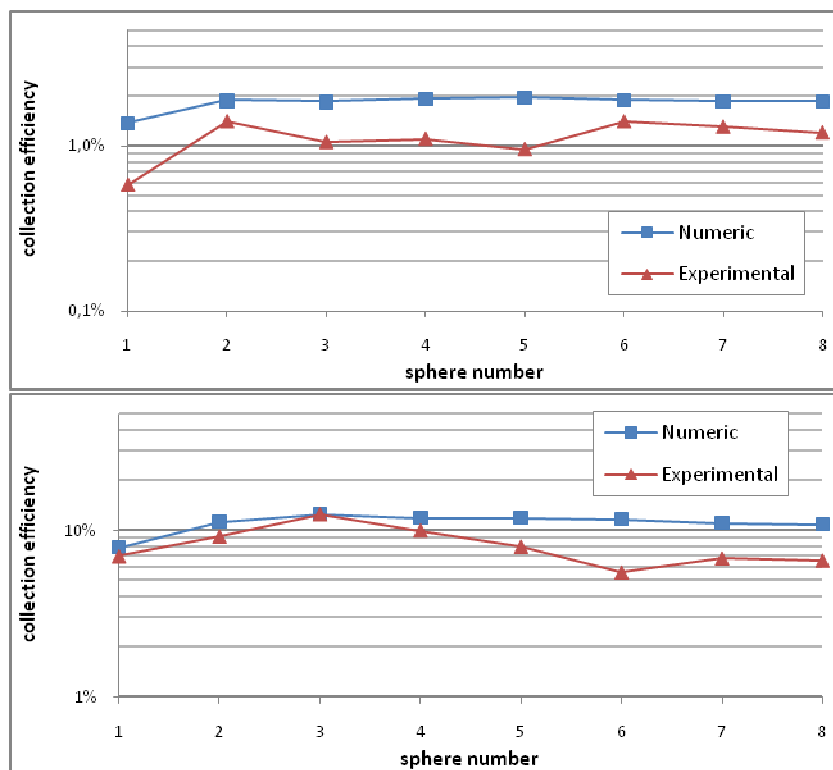
Figure 58 : Results with $L/D = 2$, model benchmarking

Globally the results have deteriorated compare to $L/D = 1.5$ and results at very low Stokes number present again the same problem. Moreover two abnormal behaviors can be observed:

- At $Stk = 0.3$ numeric collection efficiency the second sphere is overestimated
- At $Stk = 1.2$ numeric collection efficiency of the tail is overestimated

These results go against the hypothesis from which deposition should be underestimated because of lack of turbulent intensity due to RANS resolution.

For $L/D = 6$ (Figure 59) the results have again deteriorated except for those at very low Stokes number (which have slightly improved):



(a) Parameters:

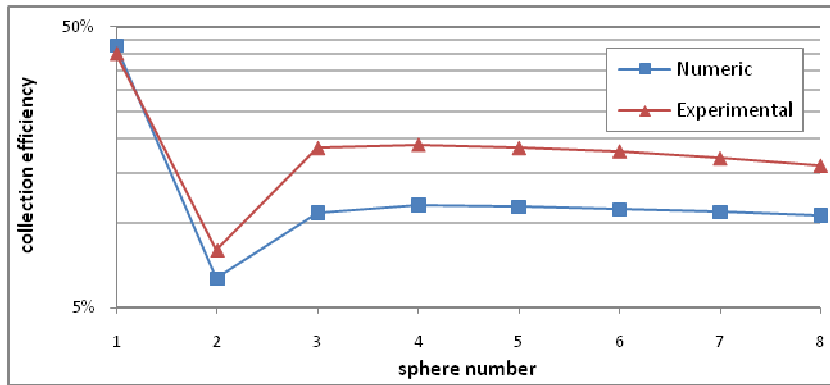
$D = 6.5 \text{ mm}$
 $d_p = 1.4 \text{ }\mu\text{m}$
 $u_0 = 14 \text{ m/s}$

$Re = 6,000$
 $Stk = 0.03$
 $L/D = 6$

(b) Parameters:

$D = 3.2 \text{ mm}$
 $d_p = 3.5 \text{ }\mu\text{m}$
 $u_0 = 14 \text{ m/s}$

$Re = 3,000$
 $Stk = 0.3$
 $L/D = 6$



(c) Parameters:

$D = 6.5 \text{ mm}$
 $d_p = 10 \text{ }\mu\text{m}$
 $u_0 = 14 \text{ m/s}$

$Re = 6,000$
 $Stk = 1.2$
 $L/D = 6$

Figure 59: Collection efficiencies with $L/D = 6$, comparison simulation results vs. data

- At $Stk = 0.03$ (Figure 59 a.) the **gap** in collection efficiency of the tail is about **-0.7%** which correspond to an **error of 56%**. As regard the **2nd sphere** for the first time the numerical simulation manage to capture the reverse shielding effect and the numerical results are **0.5% higher** which corresponds to an **error of 34%**.
- At $Stk = 0.3$ (Figure 59 b.) the **gap** in collection efficiency of the tail is about **-4.7%** which correspond to an **error of 68%**. As regard the **2nd sphere** both results present a reverse shielding effect and the numerical ones are **2% higher** which correspond to an **error of 22%**. The results obtained here must be considered with care because experimental and numerical geometry are different.
- At $Stk = 1.2$ (Figure 59 c.) the **gap** in collection efficiency of the tail is about **6.6%** which correspond to an **error of 37%**. As regard the **2nd sphere** the numerical results are **1.6% higher** which corresponds to an **error of 20%**.

The Figure 60 summarizes these results.

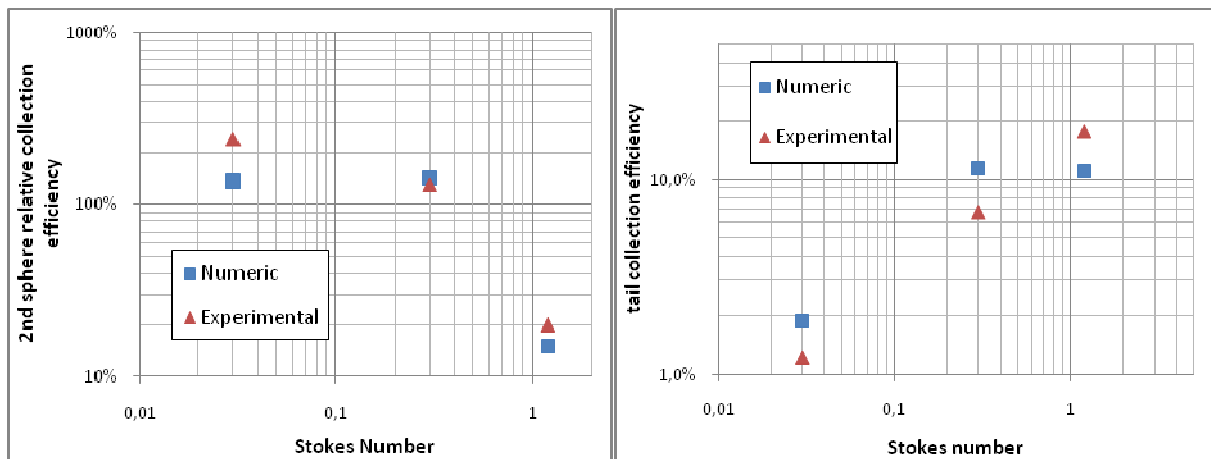
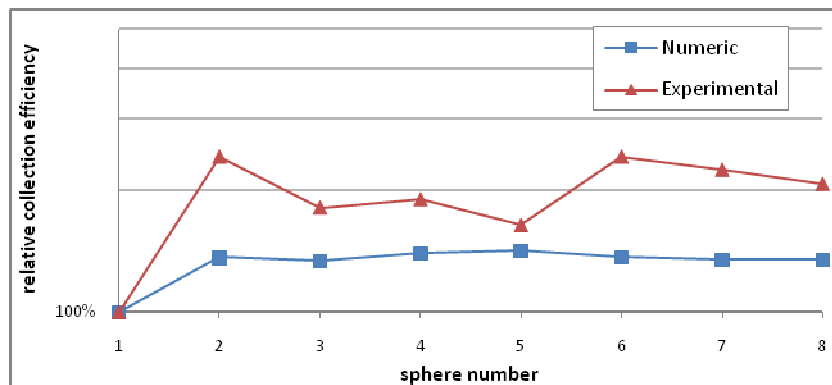


Figure 60 : Results with $L/D = 6$, model benchmarking

At high Stokes number data and computed results are qualitatively equivalent. However the values are quite different. This can also be explained by the tendency of the RANS method to underestimate the turbulence intensity: in this configuration each sphere interacts with the far wake of the previous one and turbulence intensity in the far wake can be largely underestimated by RANS calculations.

At low and medium Stokes number the numerical model overestimate particle deposition. However for low Stk it is probably the errors made on the first sphere that lead to such results. This can be verified by plotting the relative collection efficiency (Figure 61).



Parameters:

$D = 6.5 \text{ mm}$
 $d_p = 1.4 \text{ }\mu\text{m}$
 $u_0 = 14 \text{ m/s}$

$Re = 6,000$
 $Stk = 0.03$
 $L/D = 6$

Figure 61: Relative collection efficiencies ($L/D = 6$), comparison simulation results vs. data

The table 24 summarizes gaps and errors between data and numerical results.

			Sphere spacing L/D					
			1.5		2		6	
			Gap	Error	Gap	Error	Gap	Error
Stk value	Low (0.03/0.04)	Lead sphere	-0,27%	76%	-0,90%	250%	-0,80%	138%
		Shielding	1,7%	87%	1,5%	68%	-0,5%	34%
		Tail deposition	0,60%	78%	1,0%	76%	-0,7%	56%
	Medium (0.3/0.44)	Lead sphere			-0,33%	3,6%	-1,0%	13%
		Shielding	4,0%	32%	-2,8%	77%	-2,0%	22%
		Tail deposition	6,0%	14%	3,5%	35%	-4,7%	68%
	High (1.2)	Lead sphere	-4,7%	13%	-6,7%	19%	-2,6%	6,6%
		Shielding	0,90%	70%	0,30%	23%	-1,6%	20%
		Tail deposition	0,40%	8%	-1,6%	32%	6,6%	37%

Table 24 : Particles deposition on arrays, Gaps and Errors summary

In conclusion of this chapter the mains tendencies of the numerical model are:

- Whatever the spacing, numerical results at very low Stokes numbers are not in coherence with the data, particularly for close spheres where the model fails to catch the reverse shielding effect (for spheres far apart the reverse shielding effect is captured). However one has to be careful while considering the experimental data for such low values of Stk because their scattering seems to be quite important (Figure 42).
- At medium and high Stokes for $L/D = 1.5$ coherence between numerical results and data is very good. Then, even if the results are still qualitatively coherent the quantitative coherence gets worst while increasing the spacing between spheres.

If one doesn't take into account the results at very low Stk where the data can maybe not trusted, then the numerical method gives quite good results particularly for close spheres.



Conclusion

A hybrid Euler-Lagrange numerical method designed to compute particles diffusion and deposition on collectors has been investigated. Benchmarking of the method was carried out by comparing simulation results with experimental measurements of particles deposition on single and linear arrays of spheres.

First some observations can be made about the behavior of the numerical model.

As regard the Reynolds number influence on particles deposition, while it is quite negligible for single and leading spheres, it is clearly not the case for the following spheres of an array. Then, while benchmarking the model, it is really important that experiments and simulations have the same Re . As regard the level of particles deposition on the following spheres of an array, while it is always increasing when Stk increases for spheres far apart ($L/D=6$) like it does for single and leading spheres, for close spheres ($L/D=1.5$ and 2) it reaches a maximum around $Stk = 0.4$ then start decreasing. This property is interesting if one want to maximize particles deposition rate.

Then comparisons between data and computation results allow us to draw some conclusions about the model performances.

On the one hand computations underestimate particles deposition on single spheres. On the other hand particles deposition on leading spheres of an array is always over estimated. However particles deposition on singles spheres and on leading spheres of an array should be comparable particularly for high spacing between spheres where the second sphere has no chance to modify the particles deposition on the leading one. While it is the case for numerical results, data of particles deposition on leading sphere of an array are quite below the ones of singles spheres. Then one can conclude that for single and leading spheres results the experimental data scattering is quite important and numerical results are inside the boundaries of this scattering.

As regard particles deposition on the following spheres of an array, numerical results for particles with very low inertia (Stk around 0.03) are neither quantitatively (errors of deposition on the tail around 70%) nor qualitatively (reverse shielding effect not captured) coherent with data. While the qualitative incoherence is clearly due to the limitations of the model, the quantitative difference is probably also caused by the inaccuracy of experimental measurement technique which can hardly be trusted for such small particles. Then, these results cannot really be used for benchmarking the model.

Results obtained with particles with higher inertia ($Stk > 0.3$) are much more interesting for benchmarking. Qualitatively numerical results and data are always in coherence: shielding or reverse shielding effect well captured, deposition on tails follows globally the same kind of evolution. Quantitatively the difference is the lowest for close spheres (errors on tail collection efficiencies around 10% for $L/D = 1.5$) then get bigger when the spacing increase (errors around 30% for $L/D = 2$ and above 40% for $L/D = 6$). One can also note that the higher the particles inertia the lower the error.

In conclusion the numerical method investigated here gives the best results for closes spheres and shows limitations for particles with very low inertia. This is quite fortunate as pebbles beds are made of touching spheres.

The limitations of the method are probably due to a RANS calculation of the flow as it underestimates the turbulent intensity in the wake. Then the higher the spacing between spheres the higher the error made on particles turbulent diffusion and deposition. That is why computing the flow with DES instead of RANS will probably lead to quite better results. Dr Dehbi has started to work in this direction and the first results seem promising.

References

- [1] : *Particles Bubbles & Drops – Their Motion, Heat and Mass transfer*, E.E. Michaelides, World Scientific (2006)
- [2] : *A CFD model for particle dispersion in turbulent boundary layer flows*, Abdel Dehbi, Nuclear Engineering and Design 238 (2008) 707-715
- [3] : *Turbulent particle dispersion in arbitrary wall-bounded geometries: A coupled CFD-Langevin-equation based approach*, Abdel Dehbi, International Journal of Multiphase Flow 34 (2008) 819-828
- [4] : *Experiments on the flow past spheres at very high Reynolds numbers*, Elmar Achenbach, J. of Fluid Mech. 54 (1972) 565-575
- [5] : *PIV analysis of near wake behind a sphere at a subcritical Reynolds number*, Young Il Jang and Sang Joon Lee, Exp. Fluids 44 (2008) 905-914
- [6] : *Turbulent Modeling Applied to Flows over a Sphere*, George Constantinescu and Kyle Squire, AIAA Journal vol. 41 no. 9 (2003)
- [7] : *Numerical investigations of flows over a sphere in the subcritical and supercritical regime*, George Constantinescu and Kyle Squire, Physics of Fluids vol. 16 no. 5 (2004)
- [8] : *Experimental observation of aerosol deposition in turbulent flow*, Benjamin Y.H. Lui and Jugal K. Agarwal, Aerosol Science 5 (1974) 145-155
- [9] : *Inertial impaction of aerosol particles on single and multiple spherical targets*, Frank Hähner, Günter Dau and Fritz Ebert, Chem. Eng. Technol. 17 (1994) 88-94
- [10] : *Grundlegende Untersuchungen zue trägheitsbedingten Deposition luftgetragener Partikeln in Anordnungen eng benachbarter Kugelkollektoren*, Matthias Waldenmaier (PHD thesis), Universität Kaiserslautern
- [11] : *Measurements of inertial Deposition of aerosol particles in regular arrays of spheres*, Matthias Waldenmaier, J. Aerosol Science vol. 30 no. 10 (1999) 1281-1290
- [12] : *Computational Fluid Dynamics analysis of aerosol deposition in pebble beds*, Margaret Msongi Mkhosi M.S. (PHD thesis), The Ohio State University (2007)
- [13] : *Simulation of particles movement around a sphere-determination of impact efficiency and visualization of particles trajectories*, A. Hahn, Proc. 13th Annual Meeting of the AAAR (1993)

ANNEXES

Annex 1: Gambit journal file

The following Gambit journal file creates and meshes a linear array of 8 spheres in a pipe. Only one quarter of the whole geometry is generated (reduced geometry) and symmetric boundary conditions are set on the symmetry planes. The geometric and mesh parameters have to be set by the operator in the first paragraph of the journal.

```

////////////////////////////////Initialisation////////////////////////////////
identifier name "Draft" new nosaveprevious

////////////////////////////////
////////////////////////////////User defines variables (all lenght in mm)////////////////////////////////
////////////////////////////////

///Geometry
/Radius sphere
$Rs=3.25
/(=Rs*cos(45))
$C=2.298
/Core Radius and Half lenght
$Hc=6.5
/(=Hc/2)
$Ho=3.25
/Pipe radius minus Hc
$Rp=9.75
/Pipe inlet size
$Lp=39

///Sphere Bondary layers
/First row size
$Fr=0.04
/Number of rows
$Nr=14
/Growth factor
$R=1.05

///Pipe Bondary layers
/First row size
$Frw=0.05
/Number of rows
$Nrww=10
/Growth factor
$Rw=1.2

///Grid
/Core axial resolution in front of the sphere (>Nr)
$Ndc=70
/Core axial growth factor in front of the sphere
$GD=0.99
/Tube radial resolution (>Nrww)
$Ndp=30
/Tube radial inner first row size
$Fl=0.04
/Tube radial outer first row size
$Fn=2
/Circular grid resolution (per)
$Nn=64
/Core radial resolution in front of the sphere (Nns=Nn/2+1)

```

```

$Nns=33
/Core radial growth factor in front of the sphere
$GF=1.02
/(=1/GF)
$GFF=0.980392157
/Axial resolution above the sphere
$Nps=32
/Inlet axial resolution
$Npi=42
/Inlet axial last row size
$Ll=0.04

///Copy parameters
/P1=3*Hc
$P1=19.5
/P2=7*Hc
$P2=45.5

////////////////////////////////////
////////////////////////////////////Geometry////////////////////////////////////
////////////////////////////////////

//Sphere definition
/(Rs)
volume create radius $Rs sphere
face create width 100 height 100 yzplane rectangle
volume split "volume.1" faces "face.2" connected
volume delete "volume.2" lowertopology
face create width 100 height 100 xyplane rectangle
volume split "volume.1" faces "face.4" connected
volume merge "volume.1" "volume.2" real
face create width 100 height 100 zxplane rectangle
volume split "volume.1" faces "face.7" connected
volume merge "volume.1" "volume.2" real
face create width 100 height 100 yzplane rectangle
/(C)
face move "face.12" offset -$C 0 0
volume split "volume.1" faces "face.12" connected
volume merge "volume.1" "volume.2" real

//Cylinder definition
/(Hc) & (Ho)
volume create height $Hc radius1 $Hc offset -$Ho 0 0 xaxis frustum

//Vertex and edge creation
vertex create onedge "edge.38" uparameter 0.25
vertex create onedge "edge.38" uparameter 0.5
vertex create onedge "edge.38" uparameter 0.75
vertex create project "vertex.29" "vertex.30" \
    "vertex.31" edge "edge.37"
edge split "edge.38" vertex "vertex.29" connected
edge split "edge.39" vertex "vertex.30" connected
edge split "edge.40" vertex "vertex.31" connected
edge split "edge.37" vertex "vertex.32" connected
edge split "edge.37" vertex "vertex.33" connected
edge split "edge.37" vertex "vertex.34" connected
edge create straight "vertex.27" "vertex.28"
edge create straight "vertex.29" "vertex.32"
edge create straight "vertex.30" "vertex.33"
edge create straight "vertex.31" "vertex.34"
edge create straight "vertex.27" "vertex.33"

```



```

edge create straight "vertex.32" "vertex.34"
vertex create edgeints "edge.49" "edge.50" real
edge create straight "vertex.16" "vertex.35"
edge create straight "vertex.25" "vertex.27"
edge create straight "vertex.26" "vertex.32"
edge create straight "vertex.24" "vertex.33"
edge create straight "vertex.23" "vertex.34"
edge create straight "vertex.5" "vertex.31"
edge create straight "vertex.11" "vertex.28"
edge create straight "vertex.18" "vertex.29"
edge create straight "vertex.10" "vertex.30"
edge split "edge.49" vertex "vertex.35" connected
edge split "edge.50" vertex "vertex.35" connected

//Faces definition
face create "enter1" wireframe "edge.42" "edge.49" "edge.50" real
face create "enter2" wireframe "edge.43" "edge.50" "edge.60" real
face create "enter3" wireframe "edge.44" "edge.60" "edge.61" real
face create "enter4" wireframe "edge.37" "edge.61" "edge.49" real
face create "front1" wireframe "edge.35" "edge.42" \
  "edge.52" "edge.53" real
face create "front2" wireframe "edge.34" "edge.43" \
  "edge.53" "edge.54" real
face create "front3" wireframe "edge.29" "edge.44" \
  "edge.54" "edge.55" real
face create "front4" wireframe "edge.30" "edge.37" \
  "edge.55" "edge.52" real
face create "base1" wireframe "edge.13" "edge.38" "edge.57" "edge.58" real
face create "base2" wireframe "edge.23" "edge.39" "edge.58" "edge.59" real
face create "base3" wireframe "edge.10" "edge.40" "edge.56" "edge.59" real
face create "base4" wireframe "edge.5" "edge.41" "edge.56" "edge.57" real
face create "tub1" wireframe "edge.42" "edge.38" "edge.45" "edge.46" real
face create "tub2" wireframe "edge.43" "edge.39" "edge.46" "edge.47" real
face create "tub3" wireframe "edge.44" "edge.40" "edge.47" "edge.48" real
face create "tub4" wireframe "edge.37" "edge.41" "edge.48" "edge.45" real
face create "cutmid1" wireframe "edge.11" "edge.45" "edge.52" \
  "edge.57" real
face create "cutmid2" wireframe "edge.36" "edge.46" "edge.53" \
  "edge.58" real
face create "cutmid3" wireframe "edge.32" "edge.47" "edge.54" \
  "edge.59" real
face create "cutmid4" wireframe "edge.18" "edge.48" "edge.55" \
  "edge.56" real
face create "cutin1" wireframe "edge.33" "edge.49" "edge.51" "edge.52" real
face create "cutin2" wireframe "edge.24" "edge.50" "edge.51" "edge.53" real
face create "cutin3" wireframe "edge.20" "edge.51" "edge.54" "edge.60" real
face create "cutin4" wireframe "edge.31" "edge.51" "edge.55" "edge.61" real
face modify "face.15" label "sfront1"
face modify "face.11" label "sfront2"
face modify "face.3" label "sfront3"
face modify "face.14" label "sfront4"
face modify "face.6" label "smid1"
face modify "face.16" label "smid2"
face modify "face.13" label "smid3"
face modify "face.8" label "smid4"

//Cleaning
volume delete "volume.1" "volume.2"
face delete "face.2" "face.5" "face.9" "face.10" "face.17" \
  "face.18" "face.19" lowertopology

```

```
//Volume definition
volume create "vin1" stitch "sfront1" "enter1" "front1" "cutin1" \
  "cutin2" real
volume create "vin2" stitch "sfront2" "enter2" "front2" "cutin2" \
  "cutin3" real
volume create "vin3" stitch "sfront3" "enter3" "front3" "cutin3" \
  "cutin4" real
volume create "vin4" stitch "sfront4" "enter4" "front4" "cutin4" \
  "cutin1" real
volume create "vmid1" stitch "smid1" "front1" "base1" "cutmid1" \
  "cutmid2" "tub1" real
volume create "vmid2" stitch "smid2" "front2" "base2" "tub2" \
  "cutmid2" "cutmid3" real
volume create "vmid3" stitch "smid3" "front3" "base3" "tub3" \
  "cutmid3" "cutmid4" real
volume create "vmid4" stitch "smid4" "front4" "base4" "tub4" \
  "cutmid1" "cutmid4" real

edge split "edge.51" percentarclength 0.5 connected
edge merge "edge.62" "edge.51" forced

//Pipe middle creation
/(Rp)
edge create translate "vertex.27" vector 0 $Rp 0
face create rotate "edge.63" onedge "edge.42" reverse
face create rotate "edge.65" onedge "edge.43" reverse
face create rotate "edge.67" onedge "edge.44" reverse
face create rotate "edge.71" onedge "edge.37" reverse
volume create translate "face.44" "face.45" "face.46" \
  "face.47" onedge "edge.45"
face modify "face.52" label "tubmid1"
face modify "face.57" label "tubmid2"
face modify "face.58" label "tubmid3"
face modify "face.61" label "tubmid4"
face modify "face.48" label "symid1"
face modify "face.51" label "symid2"

//Pipe inlet creation
/(Lp)
edge create translate "vertex.35" vector -$Lp 0 0
volume create translate "face.44" "face.45" "face.46" "face.47" "enter1" \
  "enter2" "enter3" "enter4" onedge "edge.93"
edge delete "edge.93" lowertopology
volume delete "vin2" "vin3" "vin4" "vmid2" "vmid3" "vmid4" "volume.10" \
  "volume.11" "volume.12" "volume.14" "volume.15" "volume.16" "volume.18" \
  "volume.19" "volume.20" lowertopology
volume merge "volume.13" "volume.17" real
face merge "face.83" "face.66" mergelower
face modify "face.83" label "Inlet"
face merge "face.67" "face.84"
face merge "face.64" "face.82"
face modify "face.68" label "tubin"
edge modify "edge.96" label "guide"
edge modify "edge.101" label "guide2"
face modify "face.64" label "symin1"
face modify "face.67" label "symin2"

//Physics
physics create "tub" btype "WALL" face "tubmid1" "tubin"
physics create "SymmetryXY" btype "SYMMETRY" face "symid1" \
  "symin1" "cutmid1" "cutin1"
```

```
physics create "SymmetryZX" btype "SYMMETRY" face "symid2" \
  "symin2" "cutmid2" "cutin2"
```

```
//Reflect
/1 sphere
volume creflect "vin1" "vmid1" "volume.9" "volume.13" \
  linkmesh copyzone vector 1 0 0 origin 0 0 0
face modify "face.103" label "Outlet"
/2 spheres
volume delete "volume.15" lowertopology
volume creflect "vin1" "vmid1" \
  "volume.9" "volume.11" "volume.12" "volume.13" "volume.14" \
  linkmesh copyzone vector 1 0 0 origin $Hc 0 0
face modify "face.131" label "Outlet"
/4 spheres
volume delete "volume.20" lowertopology
volume creflect "vin1" "vmid1" "volume.9" \
  "volume.11" "volume.12" "volume.13" "volume.14" "volume.15" \
  "volume.16" "volume.17" "volume.18" "volume.19" "volume.21" \
  linkmesh copyzone vector 1 0 0 origin $P1 0 0
face modify "face.171" label "Outlet"
/8 spheres
volume delete "volume.27" lowertopology
volume creflect "vin1" "vmid1" "volume.9" \
  "volume.11" "volume.12" "volume.13" "volume.14" "volume.15" \
  "volume.16" "volume.17" "volume.18" "volume.19" \
  "volume.21" "volume.22" "volume.23" "volume.24" "volume.25" "volume.26" \
  "volume.28" "volume.29" "volume.30" "volume.31" "volume.32" \
  "volume.33" "volume.34" \
  linkmesh copyzone vector 1 0 0 origin $P2 0 0
face modify "face.245" label "Outlet"
```

```
////////////////////////////////////
////////////////////////////////////Grid resolution////////////////////////////////////
////////////////////////////////////
```

```
//Sphere BLayer
/(Fr) & (Nr) & (R)
blayer create first $Fr growth $R rows $Nr uniform
blayer attach "b_layer.1" face "basel" edge "edge.13" add
blayer attach "b_layer.1" face "cutmid1" "cutmid2" \
  edge "edge.11" "edge.36" add
blayer attach "b_layer.1" face "front1" edge "edge.35" add
blayer attach "b_layer.1" face "cutin1" "cutin2" \
  edge "edge.33" "edge.24" add
blayer attach "b_layer.1" volume "vin1" face "sfront1" add
blayer attach "b_layer.1" volume "vmid1" face "smid1" add
window modify blayer invisible
```

```
//Core
/(Nn)
edge mesh "edge.35" intervals $Nn
/(Nns)
edge mesh "edge.24" successive ratio1 $GF intervals $Nns
edge mesh "edge.33" successive ratio1 $GFF intervals $Nns
edge mesh "edge.50" successive ratio1 $GFF intervals $Nns
edge mesh "edge.49" successive ratio1 $GFF intervals $Nns
/(Nps)
edge mesh "edge.11" intervals $Nps
/(Ndc) & (GD)
```

```

undo begingroup
edge picklink "edge.62" "edge.58" "edge.57" "edge.53" "edge.52"
edge mesh "edge.52" "edge.53" "edge.57" "edge.58" "edge.62" \
    successive ratio1 $GD intervals $Ndc
undo endgroup
window modify mesh invisible

//Pipe BLayer
undo begingroup
/(Frw) & (Rw) & (Nrw)
blayer create first $Frw growth $Rw rows $Nrw uniform
blayer attach "b_layer.2" face "face.44" "face.50" "Inlet" \
    edge "edge.66" "edge.79" "edge.100" add
undo endgroup
window modify blayer invisible

//Pipe Middle
undo begingroup
edge picklink "edge.63" "edge.74" "edge.99"
/(Ndp) & (Fl)
edge mesh "edge.63" "edge.74" "edge.99" firstlength ratio1 $Fl \
    ratio2 $Fn intervals $Ndp
undo endgroup
undo begingroup
edge picklink "edge.65" "edge.78" "edge.95"
/(Ndp) & (Fl) & (Fn)
edge mesh "edge.65" "edge.78" "edge.95" firstlength ratio1 $Fn \
    ratio2 $Fl intervals $Ndp
undo endgroup
window modify mesh invisible

//Inlet and Outlet
undo begingroup
edge picklink "guide" "guide2" "edge.119"
/(Npi) & (Ll)
edge mesh "guide" "guide2" "edge.119" firstlength ratio1 $Ll intervals $Npi
undo endgroup
window modify mesh invisible

////////////////////////////////////
////////////////////////////////////Meshing////////////////////////////////////
////////////////////////////////////

//Meshing of the core
face mesh "sfront1" triprimitive
window modify mesh invisible
volume mesh "vin1" cooper
window modify mesh invisible
volume mesh "vmid1" map
window modify invisible mesh

//Meshing of the pipe middle
volume mesh "volume.9" map
window modify invisible mesh

//Meshing of Inlet and Outlet
volume mesh "volume.13" cooper source "Inlet" "enter1" "face.44"
window modify invisible mesh

//cleaning
blayer delete "b_layer.1" "b_layer.2"

```

```

////////////////////////////////////
////////////////////////////////////Physics////////////////////////////////////
////////////////////////////////////

```

```

physics create "inlet" btype "VELOCITY_INLET" face "Inlet"

physics create "outlet" btype "OUTLET_VENT" face "Outlet"

physics create "sphere1Front" btype "WALL" face "smid1" "sfront1"

physics create "sphere1Back" btype "WALL" face "face.94" "face.88"

physics create "sphere2Back" btype "WALL" face "face.105" "face.111"

physics create "sphere2Front" btype "WALL" face "face.122" "face.128"

physics create "sphere3Front" btype "WALL" face "face.185" "face.191"

physics create "sphere3Back" btype "WALL" face "face.202" "face.208"

physics create "sphere4Front" btype "WALL" face "face.162" "face.168"

physics create "sphere4Back" btype "WALL" face "face.145" "face.151"

physics create "sphere5Front" btype "WALL" face "face.299" "face.293"

physics create "sphere5Back" btype "WALL" face "face.316" "face.310"

physics create "sphere6Back" btype "WALL" face "face.333" "face.327"

physics create "sphere6Front" btype "WALL" face "face.344" "face.350"

physics create "sphere7Front" btype "WALL" face "face.259" "face.265"

physics create "sphere7Back" btype "WALL" face "face.276" "face.282"

physics create "sphere8Back" btype "WALL" face "face.219" "face.225"

physics create "sphere8Front" btype "WALL" face "face.236" "face.242"


physics create "fluidel1" ctype "FLUID" volume "vin1" \
    "vmid1" "volume.9" "volume.13" "volume.11" "volume.12" "volume.14"
physics create "fluide2" ctype "FLUID" volume "volume.15" \
    "volume.16" "volume.17" "volume.18" "volume.19" "volume.21"
physics create "fluide3" ctype "FLUID" volume "volume.34" \
    "volume.29" "volume.30" "volume.31" "volume.32" "volume.33"
physics create "fluide4" ctype "FLUID" volume "volume.22" \
    "volume.23" "volume.24" "volume.25" "volume.26" "volume.28"
physics create "fluide5" ctype "FLUID" volume "volume.48" \
    "volume.49" "volume.50" "volume.51" "volume.52" "volume.53"
physics create "fluide6" ctype "FLUID" volume "volume.54" \
    "volume.55" "volume.56" "volume.57" "volume.58" "volume.59"
physics create "fluide7" ctype "FLUID" volume "volume.42" \
    "volume.43" "volume.44" "volume.45" "volume.46" "volume.47"
physics create "fluide8" ctype "FLUID" volume "volume.35" \
    "volume.36" "volume.37" "volume.38" "volume.39" "volume.40" "volume.41"

```



Annex 2: Mesh parameters

For all the meshes presented here the common geometric parameters are:

- Sphere(s) diameter : $D = 6.5 \text{ mm}$
- Pipe diameter : $D_p = 0.1 \text{ m}$
- Inlet length : $7D$

The values of the mesh parameters for every grid used in the investigations are detailed in table 25.

Nb of Spheres	1	1	1	1	1	8	8	8	8	8	8
L/D (-)	2	2	2	2	2	1.5	2	2	2	6	6
Mesh	Coarse	Medium	Fine	Finest	Quarter	-	Coarse	Medium	Fine	Medium	Fine
Fr (mm)	0.02	0.02	0.02	0.02	0.02	0.01	0.02	0.02	0.02	0.02	0.02
R (-)	1.1	1.1	1.1	1.1	1.1	1.1	1.1	1.1	1.1	1.1	1.1
Nr (-)	20	20	20	20	17	20	20	17	15	20	15
Nn (-)	24	26	40	40	40	44	32	40	44	40	44
Nns (-)	13	14	21	21	21	23	17	21	23	21	23
GF (-)	1	1	1.05	1.05	1.05	1.05	1.03	1.05	1.05	1.05	1.05
Ndc (-)	35	40	40	40	40	41	36	40	50	70	80
GD (-)	1	1	1	1	1	1	1	1	1	1.032	1.032
Nps (-)	17	18	20	20	17	18	16	17	19	17	19
Ndp (-)	60	70	70	70	65	92	60	65	75	35	45
Fl (mm)	0.3	0.2	0.2	0.14	0.12	0.06	0.14	0.12	0.09	0.7	0.6
Fn (mm)	0.3	0.2	0.2	0.14	0.12	0.06	0.14	0.12	0.09	0.7	0.6
Npi (-)	25	35	30	60	80	45	35	35	40	15	16
LI (mm)	0.3	0.2	0.2	0.14	0.12	0.06	0.14	0.12	0.09	0.7	0.6
Grid Size (millions)	0.68	1.04	1.62	2.4	0.66	2.44	1.11	1.64	2.40	1.70	2.42

Table 25 : Mesh parameters detail



Annex 3: Flow fields results for 8 spheres

The values plotted in the figures 63 to 66 have been extracted along the pipe axis and from the spheres' surface as shown in Figure 62.

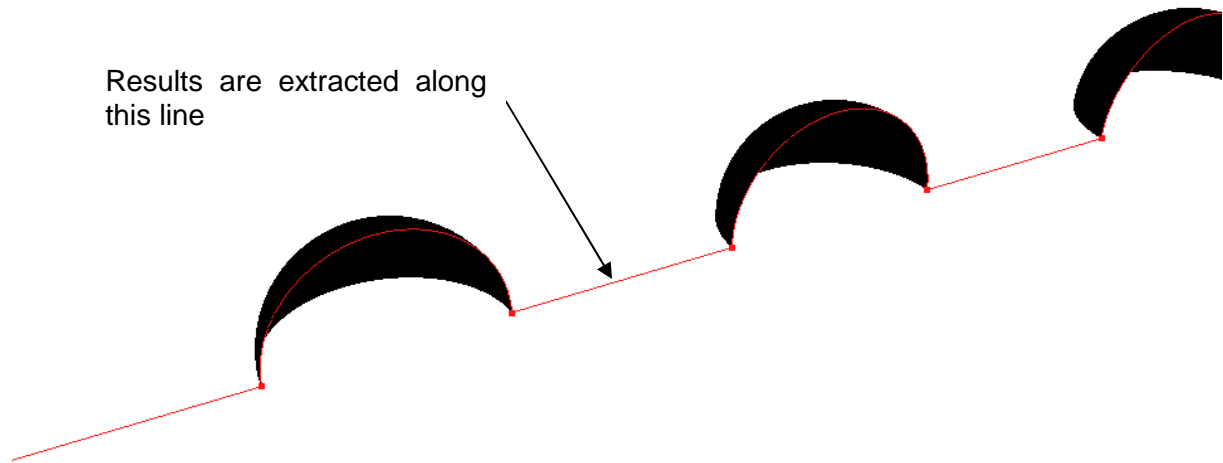


Figure 62 : Results extraction line

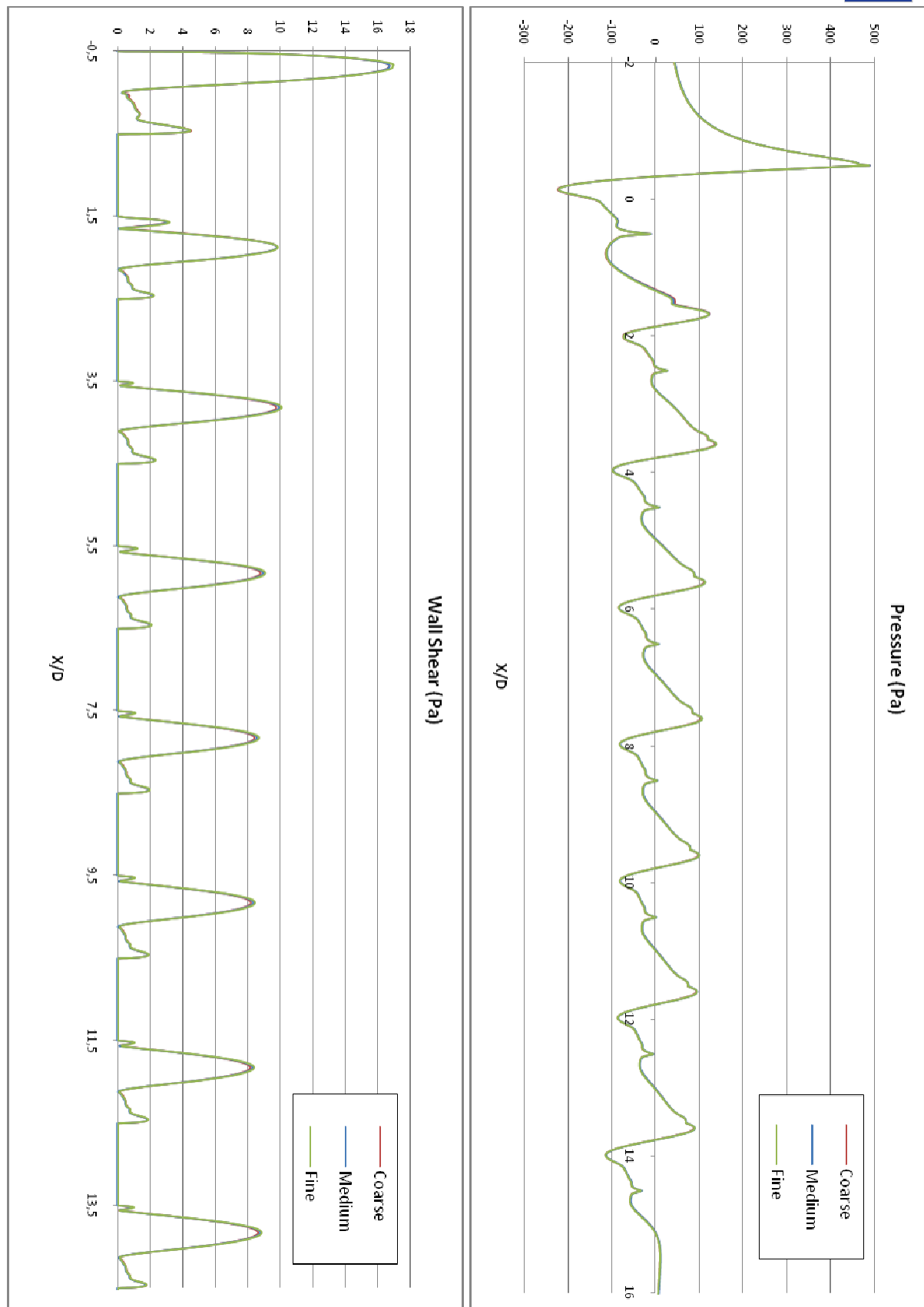


Figure 63 : 8 spheres & $L/D = 6$ & $Re = 12,000$; global wall results

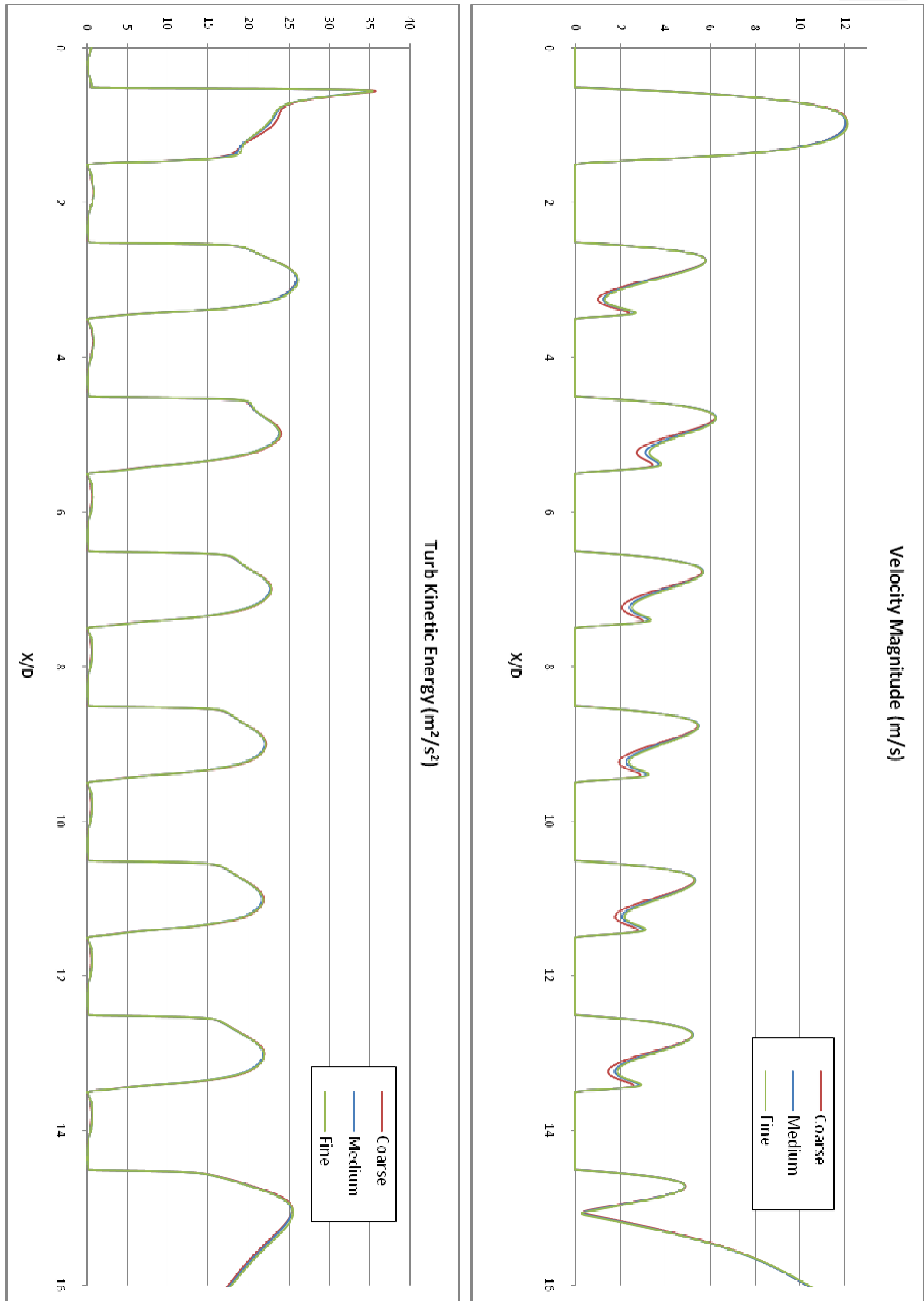


Figure 64 : 8 spheres & L/D = 2 & Re = 12,000; global wake results

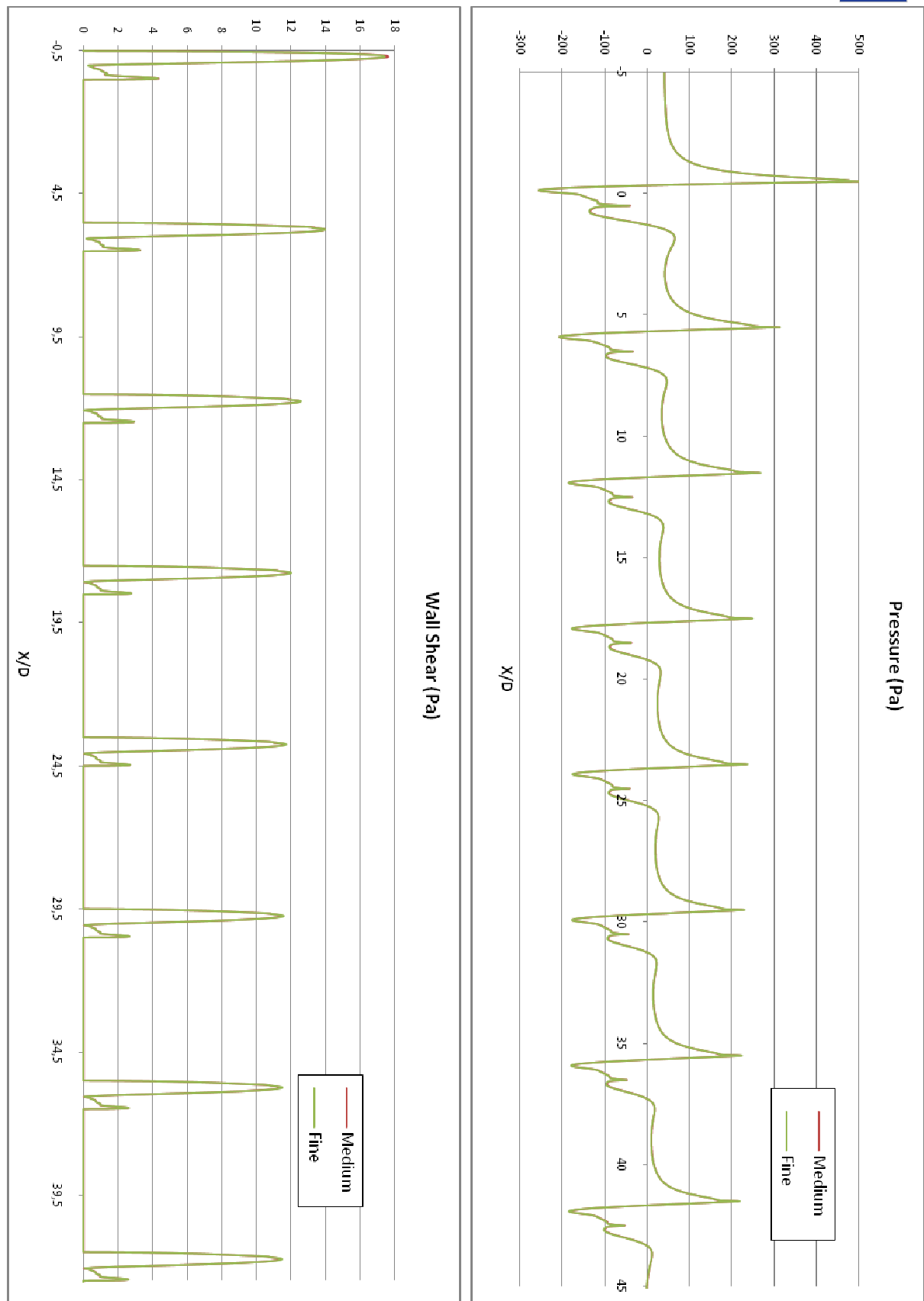


Figure 65 : 8 spheres & L/D = 6 & Re = 12,000; global wall results

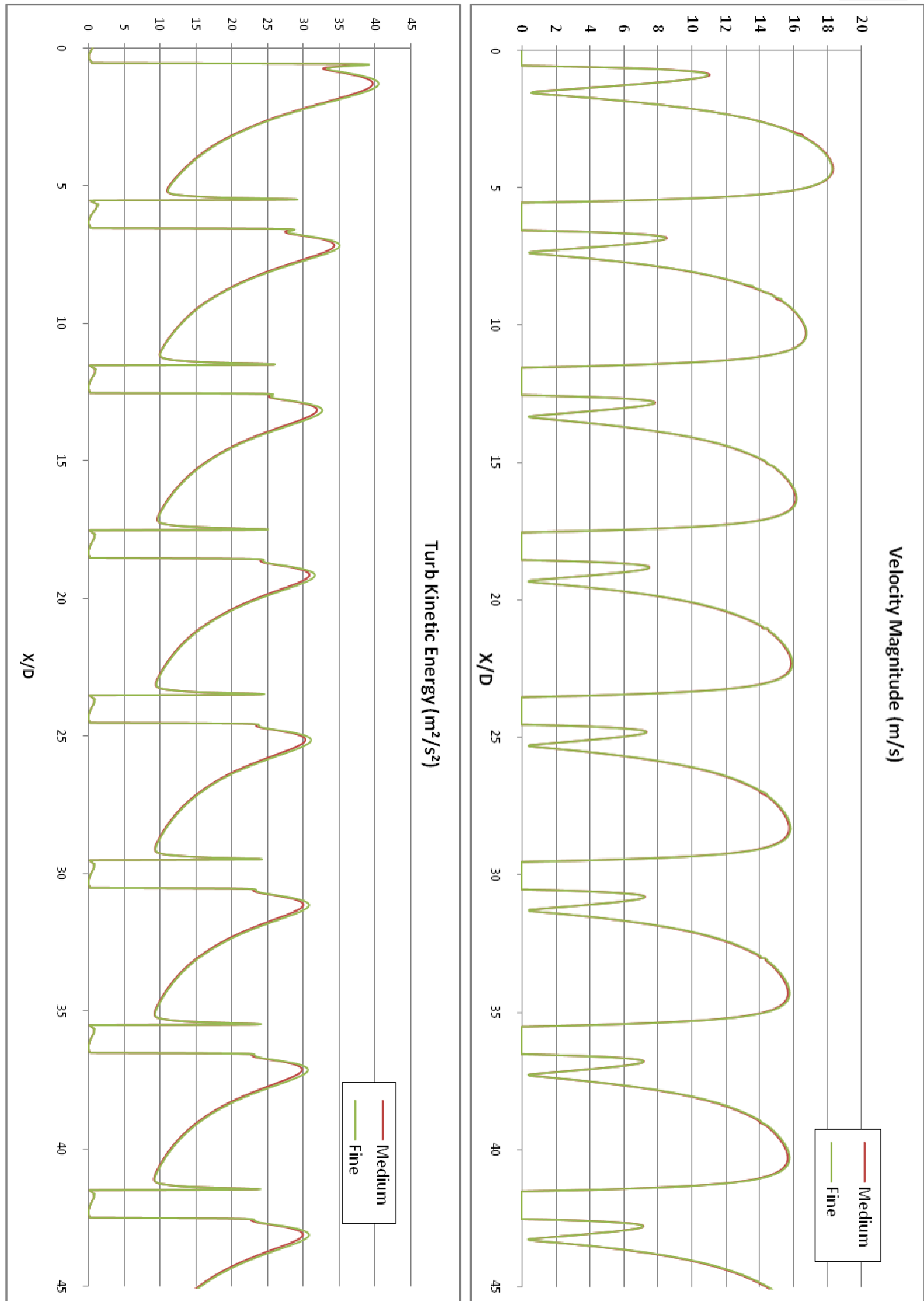


Figure 66 : 8 spheres & $L/D = 6$ & $Re = 12,000$; global wake results

Annex 4: FORTRAN Programs for injectors

- This program generates a random distribution of particles over a 6.5 mm diameter x-normal disk. The central number of particle (N_p), particles number D_p , injector ratio r , particles x velocity u_0 , and injector x position have to be set by the operator.

```

dimension d(0:100000)
PI=ACOS(-1.0)

write(6,*)'Np, Dp, r, u0, Pos inj.'
read(5,*)Np,Dp,r,u,x

dia=r*0.0065
N=Np*r**2
N=(4.1/PI)*N
N=N**0.5

jj=0
do j=1,N
  do k=1,N
    y=0.5*dia*rand()
    z=0.5*dia*rand()
    dist=sqrt(y*y+z*z)
    if(dist.le.(0.5*dia))then
      jj=jj+1
      ii1=int(3204233.423234532*y)
      ii2=int(1243333.122534532*z)
      jj1=(-1)**(ii1)
      jj2=(-1)**(ii2)
      write(1,*)'(',x,jj1*y,jj2*z,u,0,0,Dp*1e-6,293,0,')',')'
    endif
  enddo
enddo
write(6,*)Dp,jj,dia,x,u,summ,sump
end

```

- This program generates a random distribution of particles over a 6.5 mm diameter x-normal quarter disk. The central number of particle (N_p), particles number D_p , injector ratio r , particles x velocity u_0 , and injector x position have to be set by the operator.

```

dimension d(0:100000)
PI=ACOS(-1.0)

write(6,*)'Np, Dp, r, u0, Pos inj.'
read(5,*)Np,Dp,r,u,x

dia=r*0.0065
N=Np*r**2
N=(4.1/PI)*N
N=N**0.5

jj=0
do j=1,N
  do k=1,N
    y=0.5*dia*rand()
    z=0.5*dia*rand()
    dist=sqrt(y*y+z*z)
    if(dist.le.(0.5*dia))then
      jj=jj+1
      write(1,*)'(',x,y,z,u,0,0,Dp*1e-6,293,0,')',')'
    endif
  enddo
enddo
write(6,*)Dp,jj,dia,x,u
end

```

Annex 5: Particles Deposition results

The table 26 summarizes collection efficiency results for the cases with single sphere geometries.

Particle Stockes number	Sphere Reynolds Number			
	3,000	5,000		12,000
		Reduced Geometry	Whole Geometry	
0.01		0.35%	0.35%	
0.04		0.45%	0.45%	
0.1	1.6%	1.6%	0.72%	1.8%
0.16	2.6%	2.5%	1.65%	3.2%
0.24	5.5%	5.2%	4.50%	5.2%
0.4	14.5%	13.6%	12.99%	12.0%
0.6	24.7%	23.8%	23.69%	21.8%
1	39.3%	38.1%	37.75%	36.6%
1.6	52.3%	51.7%	51.22%	50.1%
2.4	63.1%	62.0%	61.37%	60.4%
4	74.5%	72.8%	72.94%	71.7%
6	80.3%	80.1%	79.67%	78.5%
10	86.9%	86.5%	86.34%	85.3%

Table 26 : Collection efficiency results for singles spheres

The table 27 summarizes deposition repartition (p), collection efficiency (η) and relative collection efficiency (η_p) results for the cases with linear array of sphere geometries. It also gives the experimental data and the numerical results obtain with the DRW model.

L/D	Re	Stk	D (mm)	Origine	Type	1	2	3	4	5	6	7	8
1,5	6000	0,04	6,5	CRW	P	16,31%	30,00%	52,94%	53,47%	40,26%	46,84%	41,46%	40,58%
1,5	6000	0,04	6,5	CRW	η	0,63%	0,25%	0,13%	0,20%	0,15%	0,15%	0,16%	0,13%
1,5	6000	0,04	6,5	CRW	ηr	100,00%	40,00%	20,92%	31,08%	23,69%	24,31%	25,23%	21,23%
1,5	6000	0,04	9	Data	η	0,36%	1,90%	0,95%	0,70%	0,60%	0,64%	0,90%	0,90%
1,5	6000	0,04	9	Data	ηr	100,00%	527,78%	263,89%	194,44%	166,67%	177,78%	250,00%	250,00%
1,5	6000	0,04	6,5	DRW	P	16,67%	4,31%	5,91%	8,25%	11,39%	3,66%	9,68%	2,14%
1,5	6000	0,04	6,5	DRW	η	0,79%	1,24%	0,91%	1,00%	0,77%	0,80%	0,60%	0,68%
1,5	6000	0,04	6,5	DRW	ηr	100,00%	157,41%	114,81%	127,16%	97,53%	101,23%	76,54%	86,42%
1,5	6000	0,3	6,5	CRW	P	5,21%	32,38%	25,78%	22,56%	20,59%	22,14%	22,14%	21,40%
1,5	6000	0,3	6,5	CRW	η	8,14%	3,07%	4,52%	5,25%	5,28%	4,78%	4,65%	4,40%
1,5	6000	0,3	6,5	CRW	ηr	100,00%	37,75%	55,54%	64,53%	64,89%	58,72%	57,10%	54,04%
1,5	6000	0,3	6,5	DRW	P	1,44%	9,05%	7,70%	5,00%	7,00%	5,11%	5,07%	0,74%
1,5	6000	0,3	6,5	DRW	η	8,83%	2,37%	3,93%	5,18%	5,02%	4,68%	4,42%	3,94%
1,5	6000	0,3	6,5	DRW	ηr	100,00%	26,85%	44,48%	58,62%	56,85%	52,98%	50,11%	44,64%
1,5	6000	0,44	6,5	CRW	P	0,84%	40,00%	23,93%	19,96%	20,53%	16,43%	19,39%	17,24%
1,5	6000	0,44	6,5	CRW	η	14,52%	1,88%	4,44%	5,40%	5,32%	5,17%	4,78%	4,78%
1,5	6000	0,44	6,5	CRW	ηr	100,00%	12,94%	30,61%	37,20%	36,66%	35,58%	32,93%	32,93%
1,5	6000	0,9	6,5	CRW	P	0,03%	50,00%	22,51%	19,18%	13,64%	14,00%	17,03%	14,13%
1,5	6000	0,9	6,5	CRW	η	33,33%	0,50%	2,25%	3,79%	4,33%	4,46%	4,67%	4,42%
1,5	6000	0,9	6,5	CRW	ηr	100,00%	1,49%	6,76%	11,37%	12,98%	13,38%	14,01%	13,26%
1,5	6000	1,2	6,5	CRW	P	0,07%	34,48%	21,60%	15,55%	14,50%	13,14%	11,82%	11,23%
1,5	6000	1,2	6,5	CRW	η	41,69%	0,40%	1,71%	3,34%	3,85%	4,23%	4,18%	4,24%
1,5	6000	1,2	6,5	CRW	ηr	100,00%	0,95%	4,10%	8,01%	9,23%	10,15%	10,02%	10,17%
1,5	6000	1,2	6,5	Data	η	37,00%	1,30%	1,70%	2,60%	3,60%	4,50%	5,20%	5,30%
1,5	6000	1,2	6,5	Data	ηr	100,00%	3,51%	4,59%	7,03%	9,73%	12,16%	14,05%	14,32%
1,5	6000	1,2	6,5	DRW	P	0,00%	14,29%	4,66%	1,96%	1,66%	1,71%	0,86%	0,57%
1,5	6000	1,2	6,5	DRW	η	41,59%	0,07%	1,15%	3,48%	5,00%	4,86%	4,53%	4,27%
1,5	6000	1,2	6,5	DRW	ηr	100,00%	0,16%	2,77%	8,37%	12,02%	11,68%	10,89%	10,27%
1,5	6000	2,3	6,5	CRW	P	0,04%	21,98%	8,79%	9,11%	9,72%	6,43%	9,58%	3,98%
1,5	6000	2,3	6,5	CRW	η	59,36%	0,44%	1,17%	2,03%	2,76%	2,96%	3,00%	3,31%
1,5	6000	2,3	6,5	CRW	ηr	100,00%	0,75%	1,96%	3,43%	4,65%	4,99%	5,06%	5,58%
1,5	6000	2,3	6,5	Data	ηr	100,00%	1,90%	2,80%	3,70%	4,30%	5,70%	5,70%	7,00%
1,5	6000	2,3	6,5	DRW	P	0,00%	18,18%	0,68%	1,79%	0,91%	0,56%	0,32%	0,67%
1,5	6000	2,3	6,5	DRW	η	59,09%	0,05%	0,71%	2,18%	3,75%	4,35%	4,62%	4,36%
1,5	6000	2,3	6,5	DRW	ηr	100,00%	0,09%	1,21%	3,69%	6,34%	7,36%	7,83%	7,37%
1,5	8300	0,44	6,5	CRW	P	0,88%	48,47%	26,94%	20,40%	18,65%	20,29%	19,57%	16,77%
1,5	8300	0,44	6,5	CRW	η	14,45%	1,28%	3,20%	4,90%	4,92%	5,00%	4,99%	4,62%
1,5	8300	0,44	6,5	CRW	ηr	100,00%	8,84%	22,17%	33,92%	34,02%	34,59%	34,49%	31,99%
1,5	8300	0,44	9	Data	ηr	100,00%	13,00%	26,00%	31,00%	37,00%	41,00%	42,00%	42,00%
2	3000	0,04	6,5	CRW	P	19,09%	21,43%	21,05%	33,33%	20,59%	34,29%	10,00%	27,27%
2	3000	0,04	6,5	CRW	η	1,07%	0,14%	0,09%	0,16%	0,17%	0,17%	0,10%	0,21%
2	3000	0,04	6,5	CRW	ηr	100,00%	12,73%	8,64%	15,00%	15,45%	15,91%	9,09%	20,00%
2	3000	0,3	6,5	CRW	P	18,71%	28,97%	27,84%	27,96%	28,17%	28,19%	26,89%	12,95%
2	3000	0,3	6,5	CRW	η	9,38%	6,18%	7,08%	7,41%	6,65%	6,61%	6,44%	5,27%
2	3000	0,3	6,5	CRW	ηr	100,00%	65,85%	75,42%	79,00%	70,84%	70,43%	68,61%	56,19%

L/D	Re	Stk	D (mm)	Origine	Type	1	2	3	4	5	6	7	8
2	3000	0,3	3,2	CRW	η	8,67%	6,38%	7,09%	7,19%	6,84%	6,37%	6,21%	5,26%
2	3000	0,3	3,2	CRW	η _r	100,00%	73,56%	81,72%	82,91%	78,87%	73,47%	71,66%	60,70%
2	3000	0,3	3,2	Data	η	9,00%	3,60%	7,00%	9,70%	11,00%	8,80%	10,00%	10,00%
2	3000	0,3	3,2	Data	η _r	100,00%	40,00%	77,78%	107,78%	122,22%	97,78%	111,11%	111,11%
2	3000	0,44	6,5	CRW	ρ	5,54%	31,52%	23,64%	22,90%	24,67%	22,03%	22,80%	16,99%
2	3000	0,44	6,5	CRW	η	16,65%	6,72%	9,33%	9,37%	9,18%	8,79%	8,49%	7,75%
2	3000	0,44	6,5	CRW	η _r	100,00%	40,33%	56,00%	56,27%	55,10%	52,78%	51,00%	46,54%
2	3000	0,9	6,5	CRW	ρ	0,48%	39,47%	18,60%	19,35%	18,63%	17,35%	17,28%	15,22%
2	3000	0,9	6,5	CRW	η	34,26%	4,03%	8,65%	9,76%	10,00%	9,84%	9,49%	8,98%
2	3000	0,9	6,5	CRW	η _r	100,00%	11,76%	25,26%	28,48%	29,20%	28,72%	27,69%	26,20%
2	3000	1,2	6,5	CRW	ρ	0,29%	36,32%	18,21%	17,19%	15,41%	14,70%	14,21%	13,03%
2	3000	1,2	6,5	CRW	η	43,16%	3,05%	7,31%	8,54%	8,77%	8,99%	8,89%	8,83%
2	3000	1,2	6,5	CRW	η _r	100,00%	7,06%	16,94%	19,79%	20,32%	20,84%	20,60%	20,47%
2	3000	2,3	6,5	CRW	ρ	0,19%	25,06%	10,39%	9,14%	11,22%	9,07%	9,15%	8,58%
2	3000	2,3	6,5	CRW	η	60,36%	2,06%	5,21%	6,51%	7,09%	7,26%	7,36%	7,33%
2	3000	2,3	6,5	CRW	η _r	100,00%	3,42%	8,63%	10,79%	11,74%	12,02%	12,19%	12,15%
2	6000	0,03	6,5	CRW	ρ	27,13%	12,41%	25,64%	33,33%	23,64%	24,62%	37,33%	36,67%
2	6000	0,03	6,5	CRW	η	1,26%	0,71%	0,38%	0,26%	0,27%	0,32%	0,37%	0,44%
2	6000	0,03	6,5	CRW	η _r	100,00%	56,20%	30,23%	20,93%	21,32%	25,19%	29,07%	34,88%
2	6000	0,03	6,5	Data	η	0,36%	2,20%	1,50%	1,10%	0,95%	1,10%	1,90%	1,60%
2	6000	0,03	6,5	Data	η _r	100,00%	611,11%	416,67%	305,56%	263,89%	305,56%	527,78%	444,44%
2	6000	0,03	6,5	DRW	ρ	13,33%	0,84%	1,69%	0,58%	2,45%	2,44%	2,53%	1,36%
2	6000	0,03	6,5	DRW	η	1,61%	1,75%	2,01%	1,67%	1,59%	1,40%	1,35%	1,44%
2	6000	0,03	6,5	DRW	η _r	100,00%	108,79%	125,15%	103,94%	98,79%	86,97%	83,94%	89,39%
2	6000	0,3	6,5	CRW	ρ	10,51%	30,51%	24,63%	25,93%	24,76%	24,66%	24,45%	15,97%
2	6000	0,3	6,5	CRW	η	9,05%	5,31%	8,20%	7,75%	7,53%	7,46%	6,90%	6,51%
2	6000	0,3	6,5	CRW	η _r	100,00%	58,65%	90,62%	85,66%	83,18%	82,43%	76,28%	71,91%
2	6000	0,3	6,5	DRW	ρ	2,36%	4,11%	2,33%	2,50%	2,30%	1,28%	1,03%	0,76%
2	6000	0,3	6,5	DRW	η	8,69%	3,33%	5,02%	5,45%	4,67%	4,96%	4,26%	4,49%
2	6000	0,3	6,5	DRW	η _r	100,00%	38,27%	57,74%	62,74%	53,70%	57,01%	48,99%	51,68%
2	6000	0,44	6,5	CRW	ρ	2,73%	37,06%	24,07%	22,37%	22,17%	23,09%	18,97%	13,75%
2	6000	0,44	6,5	CRW	η	14,84%	4,28%	7,72%	8,44%	8,27%	7,73%	7,64%	6,60%
2	6000	0,44	6,5	CRW	η _r	100,00%	28,83%	52,04%	56,87%	55,75%	52,10%	51,48%	44,48%
2	6000	0,9	6,5	CRW	ρ	0,19%	44,23%	21,40%	19,31%	17,88%	15,81%	16,79%	11,65%
2	6000	0,9	6,5	CRW	η	33,12%	1,52%	4,95%	6,92%	7,23%	7,10%	7,20%	6,32%
2	6000	0,9	6,5	CRW	η _r	100,00%	4,59%	14,93%	20,90%	21,83%	21,43%	21,75%	19,09%
2	6000	1,2	6,5	CRW	ρ	0,10%	39,43%	19,22%	15,74%	14,50%	14,94%	14,05%	8,28%
2	6000	1,2	6,5	CRW	η	41,69%	0,92%	3,90%	5,70%	6,40%	6,57%	6,62%	6,15%
2	6000	1,2	6,5	CRW	η _r	100,00%	2,21%	9,35%	13,67%	15,34%	15,76%	15,88%	14,75%
2	6000	1,2	6,5	Data	η	35,00%	1,20%	1,50%	3,20%	4,10%	4,80%	6,00%	5,60%
2	6000	1,2	6,5	Data	η _r	100,00%	3,43%	4,29%	9,14%	11,71%	13,71%	17,14%	16,00%
2	6000	1,2	6,5	DRW	ρ	0,00%	1,89%	0,19%	0,57%	0,10%	0,37%	0,54%	0,49%
2	6000	1,2	6,5	DRW	η	41,33%	0,26%	2,53%	4,26%	4,77%	5,34%	5,43%	5,96%
2	6000	1,2	6,5	DRW	η _r	100,00%	0,63%	6,11%	10,30%	11,54%	12,92%	13,14%	14,42%
2	6000	2,3	6,5	CRW	ρ	0,06%	16,95%	9,44%	10,90%	8,33%	6,27%	7,56%	3,70%

L/D	Re	Stk	D (mm)	Origine	Type	1	2	3	4	5	6	7	8
2	6000	2,3	6,5	CRW	η	58,77%	0,86%	2,53%	3,94%	4,92%	5,29%	5,23%	5,27%
2	6000	2,3	6,5	CRW	ηr	100,00%	1,47%	4,31%	6,70%	8,37%	9,01%	8,90%	8,96%
2	6000	2,3	6,5	DRW	P	0,00%	0,00%	0,48%	0,46%	0,11%	0,29%	0,18%	0,36%
2	6000	2,3	6,5	DRW	η	58,97%	0,20%	2,01%	3,20%	4,50%	5,10%	5,48%	5,40%
2	6000	2,3	6,5	DRW	ηr	100,00%	0,34%	3,42%	5,43%	7,63%	8,65%	9,30%	9,16%
2	12000	0,04	6,5	CRW	P	37,40%	66,67%	20,86%	35,96%	27,19%	30,61%	27,08%	21,67%
2	12000	0,04	6,5	CRW	η	1,24%	0,42%	0,91%	0,87%	1,11%	0,96%	1,17%	0,88%
2	12000	0,04	6,5	CRW	ηr	100,00%	34,25%	73,62%	70,08%	89,76%	77,17%	94,49%	70,87%
2	12000	0,3	6,5	CRW	P	7,26%	38,81%	30,14%	32,53%	29,89%	31,52%	32,41%	16,25%
2	12000	0,3	6,5	CRW	η	8,33%	3,68%	5,76%	5,65%	6,14%	5,91%	6,17%	4,71%
2	12000	0,3	6,5	CRW	ηr	100,00%	44,23%	69,19%	67,90%	73,70%	71,00%	74,11%	56,59%
2	12000	0,44	6,5	CRW	P	1,42%	48,69%	28,87%	31,79%	27,07%	27,46%	29,66%	14,49%
2	12000	0,44	6,5	CRW	η	13,70%	2,23%	5,17%	5,37%	6,05%	6,00%	6,25%	5,42%
2	12000	0,44	6,5	CRW	ηr	100,00%	16,31%	37,75%	39,21%	44,20%	43,84%	45,62%	39,57%
2	12000	0,9	6,5	CRW	P	0,03%	52,78%	27,98%	23,66%	20,26%	18,80%	18,72%	7,80%
2	12000	0,9	6,5	CRW	η	32,93%	0,35%	2,46%	3,73%	4,94%	5,27%	5,26%	5,00%
2	12000	0,9	6,5	CRW	ηr	100,00%	1,07%	7,46%	11,33%	14,99%	16,00%	15,98%	15,18%
2	12000	1,2	6,5	CRW	P	0,04%	47,46%	26,45%	18,81%	15,86%	15,47%	16,40%	6,58%
2	12000	1,2	6,5	CRW	η	40,65%	0,29%	1,94%	3,19%	4,34%	4,60%	5,15%	4,97%
2	12000	1,2	6,5	CRW	ηr	100,00%	0,71%	4,76%	7,85%	10,67%	11,33%	12,66%	12,23%
2	12000	2,3	6,5	CRW	P	0,04%	13,85%	10,94%	13,42%	10,32%	11,44%	8,23%	3,30%
2	12000	2,3	6,5	CRW	η	58,44%	0,32%	1,25%	1,93%	3,07%	3,67%	4,15%	4,28%
2	12000	2,3	6,5	CRW	ηr	100,00%	0,54%	2,14%	3,30%	5,26%	6,28%	7,10%	7,33%
6	3000	0,04	6,5	CRW	P	26,13%	17,34%	18,29%	17,18%	15,51%	14,29%	12,94%	6,73%
6	3000	0,04	6,5	CRW	η	1,08%	1,80%	2,11%	2,21%	2,04%	2,01%	2,38%	1,96%
6	3000	0,04	6,5	CRW	ηr	100,00%	166,22%	194,59%	204,50%	188,74%	186,04%	219,37%	180,63%
6	3000	0,3	6,5	CRW	P	6,63%	13,63%	11,77%	11,81%	11,33%	11,14%	11,63%	10,61%
6	3000	0,3	6,5	CRW	η	8,63%	11,52%	11,83%	11,84%	11,55%	11,33%	11,10%	10,83%
6	3000	0,3	6,5	CRW	ηr	100,00%	133,52%	137,14%	137,24%	133,89%	131,29%	128,64%	125,52%
6	3000	0,3	3,2	CRW	η	7,91%	11,24%	12,39%	11,81%	11,80%	11,61%	10,96%	10,84%
6	3000	0,3	3,2	CRW	ηr	100,00%	142,14%	156,68%	149,24%	149,14%	146,81%	138,57%	137,09%
6	3000	0,3	3,2	Data	η	7,00%	9,20%	12,50%	10,00%	8,00%	5,60%	6,80%	6,60%
6	3000	0,3	3,2	Data	ηr	100,00%	131,43%	178,57%	142,86%	114,29%	80,00%	97,14%	94,29%
6	3000	0,44	6,5	CRW	P	1,59%	9,75%	8,28%	7,80%	9,56%	7,85%	8,42%	7,88%
6	3000	0,44	6,5	CRW	η	16,52%	13,81%	14,50%	14,37%	14,29%	13,74%	13,33%	13,31%
6	3000	0,44	6,5	CRW	ηr	100,00%	83,64%	87,77%	87,03%	86,50%	83,20%	80,71%	80,60%
6	3000	0,9	6,5	CRW	P	0,24%	3,65%	4,03%	3,47%	4,26%	3,19%	4,11%	4,28%
6	3000	0,9	6,5	CRW	η	35,26%	15,50%	18,50%	17,57%	17,28%	16,99%	16,24%	15,83%
6	3000	0,9	6,5	CRW	ηr	100,00%	43,95%	52,47%	49,84%	49,01%	48,18%	46,06%	44,89%
6	3000	1,2	6,5	CRW	P	0,07%	3,49%	2,77%	2,58%	2,87%	2,47%	3,00%	2,33%
6	3000	1,2	6,5	CRW	η	43,99%	15,37%	19,00%	18,92%	18,04%	18,34%	16,59%	16,53%
6	3000	1,2	6,5	CRW	ηr	100,00%	34,95%	43,19%	43,00%	41,00%	41,68%	37,71%	37,58%
6	3000	2,3	6,5	CRW	P	0,04%	1,43%	0,81%	1,23%	1,17%	1,56%	1,39%	1,12%
6	3000	2,3	6,5	CRW	η	61,42%	14,37%	19,82%	19,46%	19,24%	18,80%	17,96%	19,14%
6	3000	2,3	6,5	CRW	ηr	100,00%	23,40%	32,27%	31,69%	31,32%	30,61%	29,24%	31,15%

L/D	Re	Stk	D (mm)	Origine	Type	1	2	3	4	5	6	7	8
6	6000	0,03	6,5	CRW	η	1,38%	1,88%	1,85%	1,93%	1,95%	1,88%	1,86%	1,86%
6	6000	0,03	6,5	CRW	ηr	100,00%	136,26%	134,14%	140,08%	141,78%	136,69%	135,13%	134,99%
6	6000	0,03	6,5	Data	η	0,58%	1,40%	1,05%	1,10%	0,95%	1,40%	1,30%	1,20%
6	6000	0,03	6,5	Data	ηr	100,00%	241,38%	181,03%	189,66%	163,79%	241,38%	224,14%	206,90%
6	6000	0,03	6,5	DRW	p	3,00%	8,55%	4,85%	4,15%	4,03%	1,14%	3,42%	3,59%
6	6000	0,03	6,5	DRW	η	1,48%	1,91%	1,53%	1,33%	1,28%	1,14%	1,09%	1,12%
6	6000	0,03	6,5	DRW	ηr	100,00%	128,95%	102,96%	89,80%	86,51%	76,97%	73,36%	75,33%
6	6000	0,3	6,5	CRW	p	3,73%	15,21%	15,77%	14,51%	14,46%	15,15%	14,71%	14,13%
6	6000	0,3	6,5	CRW	η	8,62%	7,09%	7,89%	8,24%	7,73%	7,70%	7,26%	7,18%
6	6000	0,3	6,5	CRW	ηr	100,00%	82,18%	91,46%	95,53%	89,59%	89,25%	84,22%	83,26%
6	6000	0,3	6,5	DRW	p	0,49%	2,48%	1,42%	1,94%	1,96%	2,28%	1,01%	1,12%
6	6000	0,3	6,5	DRW	η	8,89%	4,71%	4,47%	4,27%	3,99%	3,85%	3,38%	3,49%
6	6000	0,3	6,5	DRW	ηr	100,00%	52,99%	50,30%	48,00%	44,87%	43,34%	37,96%	39,28%
6	6000	0,44	6,5	CRW	p	0,81%	10,76%	10,40%	10,29%	9,58%	11,09%	9,59%	8,97%
6	6000	0,44	6,5	CRW	η	15,61%	7,43%	9,05%	8,81%	8,86%	8,84%	8,44%	8,10%
6	6000	0,44	6,5	CRW	ηr	100,00%	47,63%	58,00%	56,47%	56,78%	56,66%	54,09%	51,91%
6	6000	0,9	6,5	CRW	p	0,10%	3,44%	4,24%	3,64%	4,42%	4,11%	4,05%	3,53%
6	6000	0,9	6,5	CRW	η	34,41%	6,67%	10,24%	11,12%	10,92%	10,44%	10,49%	10,08%
6	6000	0,9	6,5	CRW	ηr	100,00%	19,38%	29,75%	32,30%	31,74%	30,33%	30,47%	29,30%
6	6000	1,2	6,5	CRW	p	0,04%	3,47%	2,23%	2,17%	2,26%	2,48%	2,52%	1,91%
6	6000	1,2	6,5	CRW	η	42,63%	6,35%	10,86%	11,57%	11,40%	11,18%	10,92%	10,63%
6	6000	1,2	6,5	CRW	ηr	100,00%	14,90%	25,47%	27,14%	26,75%	26,23%	25,62%	24,93%
6	6000	1,2	6,5	Data	η	40,00%	8,00%	18,50%	19,00%	18,50%	18,00%	17,00%	16,00%
6	6000	1,2	6,5	Data	ηr	100,00%	20,00%	46,25%	47,50%	46,25%	45,00%	42,50%	40,00%
6	6000	1,2	6,5	DRW	p	0,00%	0,00%	0,00%	0,00%	0,05%	0,10%	0,00%	0,17%
6	6000	1,2	6,5	DRW	η	42,16%	5,34%	9,46%	9,70%	9,62%	9,39%	8,75%	8,87%
6	6000	1,2	6,5	DRW	ηr	100,00%	12,66%	22,43%	23,01%	22,83%	22,28%	20,76%	21,03%
6	6000	2,3	6,5	CRW	p	0,02%	1,38%	0,63%	0,95%	0,76%	0,77%	0,84%	0,74%
6	6000	2,3	6,5	CRW	η	60,14%	5,99%	11,68%	12,88%	12,90%	12,69%	12,18%	11,88%
6	6000	2,3	6,5	CRW	ηr	100,00%	9,97%	19,42%	21,42%	21,45%	21,09%	20,26%	19,76%
6	6000	2,3	6,5	DRW	p	0,00%	0,00%	0,00%	0,00%	0,00%	0,00%	0,00%	0,00%
6	6000	2,3	6,5	DRW	η	59,86%	4,94%	11,91%	12,98%	12,16%	12,24%	11,41%	11,26%
6	6000	2,3	6,5	DRW	ηr	100,00%	8,25%	19,90%	21,69%	20,31%	20,45%	19,07%	18,81%
6	12000	0,04	6,5	CRW	p	30,04%	24,33%	20,66%	16,24%	16,23%	17,24%	14,48%	14,48%
6	12000	0,04	6,5	CRW	η	1,28%	1,28%	1,04%	1,14%	1,11%	1,13%	1,08%	1,08%
6	12000	0,04	6,5	CRW	ηr	100,00%	100,00%	80,99%	88,97%	86,69%	88,21%	84,03%	84,03%
6	12000	0,3	6,5	CRW	p	1,20%	15,00%	16,54%	15,08%	14,48%	13,58%	14,12%	13,78%
6	12000	0,3	6,5	CRW	η	8,14%	5,43%	5,96%	6,24%	6,77%	6,46%	6,80%	6,90%
6	12000	0,3	6,5	CRW	ηr	100,00%	66,73%	73,20%	76,74%	83,21%	79,44%	83,63%	84,83%
6	12000	0,44	6,5	CRW	p	0,21%	11,79%	8,99%	9,87%	8,31%	9,59%	9,55%	9,91%
6	12000	0,44	6,5	CRW	η	14,24%	4,92%	6,51%	6,67%	6,81%	7,07%	7,45%	7,53%
6	12000	0,44	6,5	CRW	ηr	100,00%	34,57%	45,73%	46,87%	47,82%	49,67%	52,35%	52,89%
6	12000	0,9	6,5	CRW	p	0,00%	2,53%	2,97%	2,27%	2,72%	2,19%	3,49%	2,52%
6	12000	0,9	6,5	CRW	η	33,42%	3,47%	6,40%	7,54%	8,25%	8,48%	9,09%	8,70%
6	12000	0,9	6,5	CRW	ηr	100,00%	10,39%	19,16%	22,55%	24,69%	25,36%	27,19%	26,02%

L/D	Re	Stk	D (mm)	Origine	Type	1	2	3	4	5	6	7	8
6	12000	1,2	6,5	CRW	η	41,41%	2,86%	6,74%	7,75%	8,59%	9,02%	9,63%	9,75%
6	12000	1,2	6,5	CRW	η^r	100,00%	6,91%	16,27%	18,72%	20,74%	21,79%	23,26%	23,55%
6	12000	2,3	6,5	CRW	p	0,00%	0,49%	0,45%	0,43%	0,29%	0,31%	0,39%	0,51%
6	12000	2,3	6,5	CRW	η	58,77%	3,01%	7,53%	9,08%	10,24%	10,87%	11,38%	11,43%
6	12000	2,3	6,5	CRW	η^r	100,00%	5,13%	12,81%	15,45%	17,42%	18,49%	19,36%	19,45%

Table 27 : Particles tracking results for linear arrays of 8 spheres